APPLICATIONS OF 3D PRINTING IN BIOFILM ENGINEERING AND HIGH-THROUGHPUT DIAGNOSTICS DEVELOPMENT

by

Isaak John Thornton

A dissertation submitted in partial fulfillment
of the requirements for the degree

of

Doctor of Philosophy

in

Mechanical Engineering

MONTANA STATE UNIVERSITY
Bozeman, Montana

December 2024

ACKNOWLEDGEMENTS

This dissertation would not have been possible without the support, guidance, and encouragement of many incredible individuals and organizations.

First, I would like to thank my advisor, Dr. James Wilking, for his unwavering trust and encouragement to pursue interdisciplinary research. I am also grateful to Dr. Peter Lu for his mentorship and contributions to software development and project conceptualization, and his patience in helping me hone my reasoning and writing.

I am thankful to my lab mates and collaborators, including Dr. Reha Abbassi, Dr. Thomas LeFever, and Dr. Dimitri Bikos, for their camaraderie and contributions that made the challenges of research more manageable. Special thanks to Kathryn Zimlich for her support in cultivating and managing cell cultures, and for helping me develop a deeper understanding of microorganisms. My appreciation extends to the staff, faculty, and fellow students at the Center for Biofilm Engineering for fostering a supportive research environment, including Dr. Matthew Fields, Dr. Kristen Connolly, and Dr. Heidi Smith for their guidance and training.

To my parents and sister, thank you for fostering my curiosity and always supporting me. To my friends, thank you for keeping me grounded and providing respite from research.

I acknowledge the funding sources that made this research possible, including support from the Army Research Office, the National Science Foundation, ULT Safety, and the Molecular Biosciences Fellowship Program.

Finally, I acknowledge the use of artificial intelligence technologies Grammarly and ChatGPT, for text editing. All data, analysis, and arguments presented are my own.

TABLE OF CONTENTS

TABLE OF CONTENTS CONTINUED

TABLE OF CONTENTS CONTINUED

TABLE OF CONTENTS CONTINUED

LIST OF TABLES

Table Page

LIST OF FIGURES

Figure Page

LIST OF FIGURES CONTINUED

LIST OF FIGURES CONTINUED

LIST OF FIGURES CONTINUED

LIST OF FIGURES CONTINUED

LIST OF FIGURES CONTINUED

LIST OF FIGURES CONTINUED

LIST OF FIGURES CONTINUED

LIST OF FIGURES CONTINUED

LIST OF FIGURES CONTINUED

GLOSSARY

CHAPTERS 2-4:

Vat Polymerization: A 3D printing process where a vat of liquid resin is cured by light to build a structure layer by layer.

Print Platform: The surface where the first layers of the 3D printed object are attached. Also referred to as the “build plate” or “print bed”.

Early Layers: Initial layers in vat polymerization that attach the printed structure to the print platform. Adhesion of early layers is critical for maintaining the print’s stability. Also referred to as the “burn-in layers” or the “bottom layers”

Suction Force: The force required to overcome the adhesion and vacuum created between the cured layer and the bottom of the resin vat. Also referred to as the separation force.

Peel: The act of separating a printed structure from the bottom of the resin vat. Some vat polymerization 3D printers incorporate “peel moves” to aid in cured layer separation.

Direct Laser Writing: A 3D printing technique that uses focused laser beams to polymerize resin directly on the substrate without the use of photomasks.

Extracellular Polymeric Substances (EPS): A complex mix of polysaccharides, proteins, and other compounds produced by microbes, forming the protective matrix found in biofilms.

Biofilm: A surface-associated microbial community surrounded by EPS.

Well Plate or Microtiter Plate: A standardized lab tool with multiple small wells used for high-throughput biological and chemical experimentation.

Photopolymerization: A process where light induces the polymerization of liquid resin to form solid structures.

Critical Exposure Energy (Ec): The minimum energy needed to polymerize resin during 3D printing.

Cure Depth (Cd): The distance light can penetrate resin to polymerize it effectively before the light intensity drops below Ec.

GLOSSARY CONTINUED

CHAPTERS 5-8:

POC (Point-of-Care): A POC test refers to diagnostics tests performed near or at the site of patient care. This includes fully self-administered tests like lateral flow antigen tests and tests administered by technicians outside of a lab.

Device: A diagnostic device is an integrated tool used to collect a patient sample, store reagents, and perform an assay reaction, enabling point-of-care testing.

Reagents: Chemicals and substances used in diagnostic assays to facilitate sample processing, amplification, and detection.

Assay: A procedure or test used to detect, quantify, or study the presence or activity of a substance, such as a pathogen or biomarker, in a sample.

NAAT (Nucleic Acid Amplification Test): A test that detects the presence of specific nucleic acid sequences of a pathogen by amplifying nucleic acids in a patient sample.

Amplification: In the context of NAATs, amplification refers to the process of increasing the number of copies of a specific nucleic acid sequence(s).

Incubation: In NAATs, incubation is the process of maintaining a sample at a specific temperature to promote the reaction(s) or amplification needed for the assay. This typically supports the function of polymerases or other functional molecules in the assay.

Primers: Short sequences of nucleotides that bind to specific regions of DNA or RNA to initiate the amplification process in NAATs.

PCR (Polymerase Chain Reaction): A type of NAAT that uses thermal cycling to amplify DNA sequences, making it easier to detect pathogens in a sample.

RT-PCR (Reverse Transcription - Polymerase Chain Reaction): A variation of PCR used for amplifying RNA sequences. In RT-PCR, the RNA is first converted into complementary DNA (cDNA) using reverse transcription, after which the cDNA is amplified similarly to PCR. This method is commonly used to detect RNA viruses, such as SARS-CoV-2, by targeting sequences within their RNA genome.

Thermocycling: The process of changing the temperature of a PCR assay to facilitate the stepwise process of nucleic acid amplification. The process typically includes:
1. Denaturation - 94°C for ~2 min to break apart DNA strands into single stranded DNA.

GLOSSARY CONTINUED

2. Annealing - 50°C for ~1 min to allow for primers to bind to the target sequences of single stranded DNA.
3. Extension - 72°C for 5-15 min where DNA polymerase extends primer sequences to form a new DNA strand. These steps are repeated 20-40 times for typical PCR processes.

Thermocycling Machines: Instruments used in molecular biology, particularly in PCR (Polymerase Chain Reaction) assays, to precisely control the rapid heating and cooling cycles required to amplify DNA or RNA. These machines automate the cycling process and provide a precisely controlled thermal environment. Some machines are also capable of fluorescence measurement.

LAMP (Loop-Mediated Isothermal Amplification): A NAAT that amplifies DNA at a constant temperature, providing rapid and specific detection of nucleic acids without the need for thermal cycling.

QUASR (Quenching of Unincorporated Amplification Signal Reporters) is a closed-tube detection technique for RT-LAMP assays that enhances specificity by using a dye-labeled primer incorporated into a target-specific amplicon.

ABSTRACT

Three-dimensional (3D) printing is a versatile and transformative manufacturing technology, enabling the creation of complex structures across a wide range of materials and methods. In this dissertation I describe two applications of 3D printing: the bioprinting of microbial biofilm models and the rapid prototyping of pathogen diagnostic systems. Biofilms play important roles in ecosystems, while also posing significant challenges to human health and infrastructure. Their complexity and heterogeneity influence key functions such as antibiotic resistance and bioprocessing. However, existing *in vitro* methods of studying biofilms lack control over structure and composition, limiting comprehensive studies. To address this, I develop a light-based 3D printing method to fabricate synthetic biofilm models with bacteria embedded in hydrogels. This method allows for controlled modulation of biofilm heterogeneity, enabling systematic exploration of structure-function relationships and ultimately providing a framework for engineering synthetic biofilms with controlled characteristics. I also apply the rapid prototyping abilities of 3D printing to develop novel diagnostic tools. Rapid and accessible diagnostic testing is crucial for pandemic preparedness, yet existing methods are often slow, costly, or reliant on centralized laboratories. To address these limitations, I leverage 3D printing to develop a high-throughput diagnostic workflow with automated fluorescence detection, achieving processing speeds of over 2,100 samples per hour. This diagnostic platform demonstrates the potential of 3D printing to facilitate the rapid development and deployment of diagnostic tools, which is essential for timely and efficient disease response. Together, these projects illustrate how advanced manufacturing technologies like 3D printing can drive innovation in biotechnology and healthcare, ultimately contributing to improved disease management and scientific advancement.

CHAPTER ONE

INTRODUCTION

This dissertation explores the use of three-dimensional (3D) printing as an enabling technology for research and development across diverse scientific domains. By offering precise, rapid, and accessible fabrication, 3D printing facilitates innovative solutions that are unattainable or impractical with traditional methods. This work focuses on two key applications where 3D printing serves as an enabling technology: (1) light-based 3D bioprinting to fabricate synthetic biofilms, providing a platform to study microbial structure-function relationships and engineer living materials; and (2) the use of rapid prototyping to develop a diagnostic method that improves upon accessibility and throughput in pathogen detection. This introductory chapter outlines the challenges addressed, identifies limitations in existing methods, and presents the guiding hypotheses and objectives of the research that I detail in the subsequent chapters.

1.1 Bioprinting of Synthetic Biofilms

3D bioprinting has emerged as a powerful tool for replicating the architectural and functional organization of biological systems. Traditional two-dimensional or liquid cell culture methods are limited in their ability to mimic the complex spatial and physiological characteristics of mammalian tissues and microbial communities. While bioprinting has been extensively used for fabricating eukaryotic systems (e.g. tissue engineering), its application in studying microbial systems—particularly for creating synthetic biofilms—remains relatively unexplored.

Biofilms, which are surface-associated microbial communities encased in extracellular polymeric substances (EPS), are prevalent in both natural and built environments and play critical roles in processes and problems ranging from nutrient cycling to chronic infections. Their structural and functional complexity, driven by heterogeneity and microbial interactions, emerges from and is deeply intertwined with their physical organization. Existing *in vitro* methods, such as microtiter plates and flow reactors, lack the ability to control the structure of biofilms as they develop, making it difficult to isolate and systematically investigate the interactions that drive their emergent properties.

3D bioprinting enables precise spatial control over biofilm structures, making it a valuable tool for applications such as the generation of living materials and biosensors. Despite these advancements, the potential of 3D bioprinting for creating models with biofilm-like geometries remains largely unexplored.

I hypothesize that light-based 3D bioprinting can be used to fabricate synthetic biofilms with defined structural and compositional characteristics, enabling the systematic study of biofilm heterogeneity and function.

To test this hypothesis, this research focuses on the following objectives:

1. Develop a novel photolithographic bioprinting method for creating thin hydrogel films with embedded bacterial cells.
2. Use this method to fabricate synthetic biofilms with controlled initial cell densities and spatial arrangements.
3. Characterize the growth dynamics, structural heterogeneity, and emergent properties of synthetic biofilms over time.

4. Explore the relationship between biofilm structure and function, including gradients in cellular activity and resource availability.

By integrating advanced 3D bioprinting techniques with biofilm research, this work seeks to provide new insights into biofilm dynamics and establish a versatile platform for studying and engineering biofilms with tailored properties. These findings have implications for both fundamental research and practical applications, including microbial biofabrication and biofilm-based technologies.

In Chapters 2-4 of this dissertation, I present an in-depth background on biofilms and biofilm research (Chapter 2), outline the development of a novel bioprinting technology (Chapter 3), and discuss the fabrication and analysis of synthetic biofilms (Chapter 4).

1.2 High-Throughput Infectious Disease Diagnostics

Emerging infectious diseases pose a persistent threat to global health. Factors such as increased human-wildlife interactions, climate change, and global connectivity create conditions conducive to outbreaks of previously unknown pathogens. Such pathogens are particularly dangerous because they emerge in populations lacking immunity, effective treatments, or vaccines, allowing rapid spread with the chance for significant morbidity and mortality. Pandemic preparedness requires robust tools and strategies for early pathogen detection and outbreak response. Among these tools, diagnostic testing is cruicial for identifying infections, tracking disease spread, and guiding containment efforts.

The COVID-19 pandemic exposed vulnerabilities in global diagnostic capacity. Early detection relied on diagnostics, yet the slow development and deployment of effective tests hindered containment efforts. Existing diagnostic methods, such as reverse transcription polymerase chain reaction (RT-PCR) and rapid antigen tests, face significant limitations. RT-PCR, though highly sensitive, requires costly equipment, trained technicians, and specialized infrastructure, making it unsuitable for low-resource settings. Rapid antigen tests, while accessible, suffer from lower sensitivity and limited applicability in detecting asymptomatic or early-stage infections. These challenges highlight the need for diagnostic platforms that are sensitive, scalable, and widely deployable.

Isothermal amplification methods, such as reverse transcription loop-mediated isothermal amplification (RT-LAMP), offer advantages over traditional diagnostics by operating at a constant temperature. This simplifies nucleic acid amplification and enables deployment with fewer equipment requirements. However, diagnostic applications of RT-LAMP, particularly those tailored to the challenges of outbreak response, have not been fully realized. Addressing these gaps requires innovative approaches to enhance the scalability and accessibility of this promising technology.

This research addresses critical gaps in diagnostic testing by hypothesizing that **a** platform integrating isothermal amplification with custom-designed, 3D printed tools, such as a point-of-care diagnostic device and a rapid serial fluorescence detection system, can overcome existing limitations in throughput and accessibility. Central to this hypothesis is the enabling role of 3D printing, which provides the flexibility, speed, and cost-effectiveness necessary to design, prototype, and refine novel diagnostic tools.

To address this hypothesis, the research presented in this dissertation aims to:

1. Develop a user-friendly point-of-care diagnostic device to support sample collection and test preparation in non-laboratory settings.

2. Create a scalable diagnostic platform that integrates RT-LAMP with 3D-printed fluorescence detection systems.
3. Optimize throughput using a novel serial detection system to efficiently process large volumes of samples.
4. Validate adaptability by detecting diverse pathogens, including SARS-CoV-2, Zika virus, and Infectious Bronchitis Virus.
5. Demonstrate accessibility through low-cost incubation systems that simplify deployment in resource-constrained environments.

In Chapters 5-8, I provide background on diagnostic methods and describe the development of novel testing methods using 3D printing. I present background on current infectious disease diagnostics and their limitations (Chapter 5) and outline the methods used to develop the diagnostic device and equipment using 3D printing (Chapter 6). I then describe the creation of a saliva-based diagnostic device for point-of-care testing (Chapter 7) and finally, I detail the development of a high-throughput diagnostic detector and workflow (Chapter 8).

CHAPTER TWO

BACKGROUND OF BIOFILMS AND MICROBIAL BIOPRINTING

2.1 Introduction to Biofilms and Biofilm Engineering

2.1.1 Biofilm: Surface Associated Microbial Communities

There are an estimated 10^{30} microbial cells on earth, a figure that surpasses the number of stars in the observable universe ($\sim 10^{21}$) by nine orders of magnitude. Current estimates suggest up to 80% of those cells reside in surface adhered microbial communities known as biofilms[1]. Biofilms are foundational to the biosphere and play critical roles in geochemical cycling of essential elements like carbon, oxygen, and nitrogen. The adaptability and complex structures of biofilms allow them to survive in diverse environments, playing critical roles in ecosystem functionality[1–3]. For example, nitrogen fixing biofilms transform atmospheric nitrogen into forms available to plants, contributing to soil fertility and agricultural productivity[4,5]. Decomposing microbial communities break down organic materials into simpler compounds that can be used by other organisms to function, grow, and reproduce[6]. These processes are supported by the biofilm's ability to maintain microenvironments that allow for cooperative interactions between diverse microbial species[2].

Beyond their natural ecological roles, biofilms have been harnessed by humans for a variety of industrial applications. For thousands of years, microbial processes have been utilized for fermentation, which enabled the production of food and beverages like bread and beer for at least 13,000 years[7,8]. Over time, our understanding of microbial communities, including biofilms, has expanded and today, they play crucial roles in modern industries[9,10]. In wastewater treatment, biofilms are vital for breaking down organic waste materials and potential pollutants[11]. For example, aerobic granular sludge systems have revolutionized wastewater treatment by providing efficient removal of carbon, nitrogen, and phosphorus. The biofilm structure allows for metabolic diversity, providing treatment functionality and improving treatment efficiency[10–12].

Biofilm bioprocessing and bioremediation are of significant interest for their ability to transform wastes and/or create valuable products[13]. Microbial communities have demonstrated the ability to produce biofuels[14], bioplastics[15], and a number of other useful products[12]. This approach not only addresses environmental pollution but also offers a sustainable pathway for industrial processes by reducing reliance on finite resources and fostering a more resilient, low-carbon economy[13,16]

The broad functionalities of biofilms have led to their consideration as a foundation for a cyclic bioeconomy – an economic model that aims to minimize waste and maximize resource efficiency by using biological processes. In the current linear economic system, resources are extracted, processed (typically using energy from fossil fuels), used, and then discarded, leading to significant environmental impacts like pollution and resource depletion. In contrast, a circular bioeconomy seeks to close this loop by continuously recycling and reusing materials, thereby reducing waste and extending the life cycle of resources. The metabolic diversity and adaptability of microbial communities in biofilms offer significant potential to drive this model forward by enabling the sustainable conversion of waste into valuable products, contributing to a low-carbon, circular economy[10,13,17].

While biofilms offer numerous benefits, they also present significant challenges. Their ability to adhere to surfaces and form resilient living structures contributes to their destructive roles in several contexts. Biofilms are associated with corrosion of human infrastructure, currently estimated at a cost of over $2.6 trillion per year. Medical biofilms are associated with hospital acquired infections, the rise of antibiotic resistance, and chronic wounds with costs estimated at nearly $400 billion per year globally. Biofilms pose significant risks to human health, industry, and infrastructure[18]. Addressing these challenges requires more effective biofilm control and mitigation strategies, which can be developed through a deeper understanding of biofilm behaviors, interactions, and environmental resilience.

Despite significant advancements in microbial research, our understanding of the full diversity of these microbial communities and their interactions remains limited. Isolating and investigating the behaviors and functionalities of biofilms is challenging owing to the complexity and diversity of the biofilm form and our ability to recapitulate these environments in the lab. For example, most microbial research has been performed with a select number of microbial isolates that have been amenable to the provided *in vitro* environments. However, the vast majority of microbial organisms are currently unculturable using conventional methods[19,20]. This limitation is likely due to the specific and complex environmental conditions these organisms require, which are difficult to replicate outside their natural habitats[19]. This gap highlights the need for innovative culturing techniques that can better mimic aspects of naturally formed biofilms under controlled conditions.

In this chapter I discuss biofilm systems, examining key features of the biofilm form and how specific properties and functionalities emerge from these features. I review current methodologies for culturing biofilms *in vitro*. I also discuss approaches for creating artificial biofilms including methods of hydrogel encapsulation and microbial 3D printing. It is through our ability to isolate, probe, and observe these complex systems that we can derive understanding and gain the ability to control and employ these powerful biological systems.

2.1.2 The Emergent Heterogeneity of Self-Assembled Biofilms

Biofilm formation is a complex multistage process that starts with microbial adhesion to a surface and results in a community of microbes embedded within a matrix of community-produced extracellular polymeric (EPS) materials. This developmental process involves distinct physiological changes, differentiating surface associated microbes from their planktonic counterparts[21,22]. For example, in biofilms formed by *Pseudomonas aeruginosa*, flagella-mediated motility is greatly reduced while genes involved in EPS production are upregulated[23].

As biofilms mature, the EPS matrix can play an influential role in shaping microenvironments within the structure. The suppression of nutrients and waste transport generates localized gradients as molecules must diffuse through the polymeric mesh. Microbes located closer to resource sources (e.g. the biofilm surface) gain preferential access and may consume them before they can reach deeper layers[24]. These systems of diffusion and reaction influence the distribution of resources and cause stratified layers where microbes in different positions within the same biofilm (e.g. top and bottom) experience distinctly different environments and consequently exhibit different physiological behaviors[23–25]. Patterns of localized metabolisms and species emerge from the landscape of resource and waste reaction and diffusion, generating the spatial heterogeneity that is characteristic of the biofilm form.

Spatial heterogeneity is critical to emergent biofilm functions. For example, microbes in resource limited regions of a biofilm can develop resistance to environmental stressors, including antibiotics, due to their slow growth rates or the activation of stress response pathways[24,26].

Moreover, the stratification within biofilms can lead to the development of specialized niches[24]. *Pseudomonas aeruginosa*, capable of both aerobic and anaerobic metabolisms, switches to anaerobic denitrification deep within synthetic biofilms when oxygen is consumed by sister cells performing aerobic metabolism in the top layers of the biofilms[27].

The interdependence between structure (e.g. geometry and composition) and function (e.g. metabolism and gene expression) is pivotal to how biofilms develop, adapt, and persist. Each structural component of a biofilm, from the thickness and composition of the EPS to the spatial arrangement of cells, plays an influential role in its functionality, impacting everything from nutrient uptake and stress resistance to community diversity and metabolic profiles. Conversely, functions such as nutrient uptake, metabolic activity, or phenotype can influence how the biofilm's structure develops over time[2,24]. Biofilms formed by different species within the same environment create distinct biofilm structures[28,29]. In contrast, the same species grown in different environments will also form distinctly different biofilm structures[30,31]. It is evident that structure is critical to biofilm function and vice versa, yet current biofilm methods offer limited control to researchers to produce biofilms with directed structures.

2.1.3 Current Biofilm Methods:

Culturing Biofilms in the Lab

Methods of culturing biofilms in the lab are key to understanding the formation, structure, and behavior of biofilms under controlled conditions. Several methods of growing biofilms *in vitro* have been developed, each with advantages and limitations, and each producing different types of biofilms. These *in vitro* biofilms are shaped by environmental factors such as resource availability, surface interactions, and shear stress[2]. Thus, the method used to culture biofilms plays a critical role in determining the biofilm form and its characteristics, making the method used to culture biofilms important to consider.

Common biofilm forms include pellicle, submerged, and colony biofilms. Pellicle biofilms develop at the air-liquid interface where oxygen is typically abundant[32]. In contrast, submerged biofilms form on surfaces fully immersed in liquid, where gradients in nutrient and oxygen concentrations create spatial heterogeneity in microbial activity[33]. Submerged biofilms are commonly cultured using flow cells and biofilm reactors. With these systems researchers can control surface properties, nutrient concentrations, and flow. Lastly, colony biofilms form on solid surfaces such as agar plates, providing a more controlled environment for studying spatial growth patterns and microbial resistance. These biofilms are useful for high throughput genetic and metabolic studies, as their structure and development can be easily observed. Each biofilm type offers unique insights, and the method chosen to culture biofilms must align with the organism of study and the research objectives.

Several lab-based methods are used to culture biofilms, each catering to different research needs. Microtiter plates are one of the most widely used tools, enabling high-throughput screening of biofilms. This method involves growing biofilms in multi-well polystyrene plates, enabling the growth of multiple biofilm conditions (e.g. 48, 96, and 384) in parallel. For example, 31 different *Listeria monocytogenes* strains were studied in a microtiter plate where epifluorescence microscopy of the resultant biofilms was used to quantify growth across the genetic differences[34]. Typically, bacteria are grown in these systems as submerged and pellicle biofilms. To measure biofilm growth, the plates are emptied and rinsed to remove free floating cells before the adhered biomass is stained. Plate readers are often used to quickly and efficiently gain information about biofilm growth. However, this method selects for cells which have adhered to the wells under the imposed environmental conditions and those which are not removed by washing steps. Sedimentation of free floating bacteria may skew results of this method[32].

To address the limitations of well-surface attachment, the Calgary biofilm device was developed. This method grows biofilms on individual submerged pegs within the well of microtiter plates. Cells that attach to the pegs are more likely to be biofilm formed and to not have originated planktonically before sedimentation[32]. This offers improved isolation of biofilm formation compared to traditional micro-titer plates, but both methods still pose challenges for direct observation of biofilms. Since plates must be rinsed before analysis, and the pegs removed for imaging, these methods often disturb the biofilm or are not conducive to real time biofilm observation. More specialized microtiter plates have been developed which allow for biofilm growth to be monitored using inverted microscopy without disturbing the experiment, but additional processing may still be required to stain or prepare the biofilm for imaging (see Section 3.1)

Rotary biofilm reactors, like the Center for Disease Control (CDC) reactor, offer a method focused on the effects of material surfaces and shear stress on biofilm development. The CDC reactor produces a turbulent, high shear environment around multiple embedded coupons, ideal for studies of biofilm development under varying hydrodynamic conditions[33]. Though the CDC reactor offers consistent flow conditions, it remains relatively complex and expensive to operate, and *in situ* microscopy observation is not feasible without disrupting the experiment[32].

Flow cells facilitate the study of biofilm dynamics under continuous nutrient flow and waste removal. Drip flow reactors, in particular, are designed to generate submerged biofilms while simulating environments with low shear such as in those found in catheters, cystic fibrosis lungs, or the oral cavity[35]. Following a batch culture establishment phase and a continuous flow phase, coupons can be removed for imaging and further analysis. The ability to use glass coupons makes these systems well suited for microscopy base studies. However, the complexity of flow cells is not well-suited for high-throughput applications[32].

Microfluidic devices have gained significant attention in biofilm research for their ability to provide precise environmental control and enable in situ observation of biofilm behaviors[36–39]. Their flexibility in design and ability to model various flow conditions make them powerful tools for studying biofilms. Despite these advantages, the fabrication of these devices is challenging and resource intensive, requiring specialized fabrication knowledge and equipment[32].

Here I have described a variety of biofilm culture methods. Each method produces different growth conditions and, consequently, different types of biofilms[33]. Different methods also offer different advantages and disadvantages in observation, throughput, and ease of use. Additionally, finding the right environmental parameters for inocula to attach, grow, and form biofilms is a common challenge across all methods. This highlights the importance of choosing the right method for biofilm studies, as the method itself can significantly influence biofilm formation.

2.1.4 Mimicking the Matrix: Cell Laden Hydrogels

A defining feature of biofilms are the extracellular polymeric substances (EPS). The EPS is composed of myriad molecules including polysaccharides, proteins, and extracellular DNA[22].

Biofilm community members produce any number of the EPS components dependent on their genotype and physiological state. The excreted EPS contributes to many of the biofilms defining properties including adhesion to the substrate, cellular aggregation, sorption of materials, the formation of chemical gradients, and resistance to stressors[21]. The EPS plays a large role in creating the environment of the biofilm, stimulating microbial behaviors distinct from those of the planktonic state.

Recreating the cellular environment provided by the EPS in a laboratory setting is non-trivial. Artificial biofilm models are of significant interest for studying microbial populations within well-defined structures. Hydrogels, or gels composed of hydrophilic polymer networks with high water content, have emerged as effective extracellular matrix mimics for both eukaryotic and prokaryotic cells[26,40,41]. Hydrogels represent a wide class of materials and include both synthetic and natural polymers that can be crosslinked or entangled to produce soft structures[40].

Natural polymers including agarose, collagen, and alginate, are favorable for their biocompatibility. Moreover, natural polymers can provide binding sites and other bioactive motifs which are important for some cellular processes[41]. Agarose is a polysaccharide derived from marine algae and exhibits thermally reversible gelation wherein it can be heated and solubilized into a liquid before being cooled into a solid form[42]. Agarose has been used to scaffold[43] and embed[26] bacteria to create artificial biofilm models.

A study of *Staphylococcus aureus* embedded in agarose hydrogel was used to mimic characteristics of biofilm infections. The resulting colonies exhibited size gradients as a function of distance from the oxygen-rich surface. Studies of antibiotic susceptibility showed that this biofilm model exhibited key characteristics of biofilm infections including the formation of dense cell aggregates, reduced specific growth rates, oxygen gradients, and antibiotic tolerance[26]. A study of *S. aureus* in agarose droplets was used to develop a model of diffusive transport in biofilm. Here, two artificial biofilm systems, one with high cell density and one with lower cell density, were used to model reaction and diffusion. Control of the embedded cell concentration provided a platform to probe reaction in the system and comparison of the model under controlled conditions[44].

Though natural polymer systems exhibit many desirable properties for cell culture, the ability to modify and tune polymer chemistry provides additional opportunities. For example, synthetic polymers like polyethylene glycol (PEG) and polyacrylamide (PA) can be synthesized to produce polymers with narrow molecular weight distributions and controlled properties like chain length[41]. Moreover, polymer synthesis enables further modification to polymers through the addition of functional groups. I discuss the functionalized synthetic polymer system of polyethylene diacrylate (PEG-DA) for photopolymerization in section 2.2.

The mesh size (i.e. pore) of polymer gels is typically on the order of 10 nm[45,46]. Therefore, embedded microorganisms, which are typically on the order of 1 μm (= 1000 nm), become entrapped. Gel embedded microbes grow to form densely packed spherical or ellipsoidal colonies within the gel, deforming the gel locally to form colonies against the tension of the polymer matrix[47]. While the turgor pressure of a bacterial cell (~10^5 Pa) is orders of magnitude greater than the elasticity of a hydrogel (~10^3 Pa), it is clear that the mechanical properties of the gel can modulate cell behavior[47–49]. For example, a study of methacrylated alginate (MA) demonstrated the growth of *Escherichia coli* bacteria in soft, moderate, and stiff hydrogels with elastic moduli of 0.85, 1.96, and 5.12 kPa respectively and found that stiffer matrices resulted in smaller colony growth. Transcriptional analysis of the embedded bacteria found the significant upregulation of five genes and down regulation of 38. Among the downregulated genes were those associated with the tricarboxylic acid (TCA) cycle, a central pathway in cellular metabolism that plays a key role in energy production. The down regulation of these genes is associated with reduced metabolic activity in the embedded cells, a phenomenon linked to increased antibiotic resistance[49].

The studies described above support the use of synthetic hydrogels as versatile platforms for artificial biofilm studies. Hydrogels not only facilitate control over physical conditions and geometry, but also enable the systematic study of bacterial response to these controlled environments. Such insights are valuable for understanding the links between biofilm structure and biofilm behavior.

2.1.5 Controlling Cell Placement in Three Dimensions

The study of biofilms in the laboratory presents a set of distinct challenges as previously described. Natural biofilms are complex, heterogeneous systems and many distinct biofilm properties emerge from this heterogeneity. Growing biofilms is a challenging task and is highly dependent on the organism, the method, and the prescribed environment. These factors together create a research landscape with little control over the biofilm outcome. Consequently, this lack of control limits researchers' ability to isolate and investigate specific relationships between the structure of biofilms and the functional properties associated with these structures.

Controlling the spatial organization of biological cells has been an area of research for many decades and has produced numerous methods and technologies. In mammalian tissues and biofilms alike, cells are suspended in and surrounded by a complex matrix of polymers, nutrients, and notably other cells, whose proximity, density, and activity influence one another. Our ability to study these systems lies in part in our ability to mimic this complex three-dimensional environment. 3D bioprinting represents a set of methods which use biocompatible materials and 3D printing systems to precisely deposit or otherwise control the spatial organization of biological materials.

One of the first cell positioning methods used modified inkjet printers and graphics plotters to deposit cell adhesion proteins and anti-cell-surface monoclonal antibodies to the surface. The controlled deposition of these molecules facilitated the controlled adhesion of both fibroblast and HeLa cell lines, thereby enabling their controlled spatial position[50]. The use of cytoscribing presented an interdisciplinary solution spanning biology, materials science, engineering, and computing and represents one of the earliest ventures into bioprinting.

Advancements in materials science, biology, printing hardware, and computers offer additional capabilities for cellular organization. One of the earliest bioprinting demonstrations using a bioink (i.e. cell containing, biocompatible ink) utilized a modified desktop inkjet paper printer (HP 660C), replacing the standard printer ink with a cell suspension[51,52]. The inkjet printer used a series of piezo pumps to control bioink deposition, enabling submillimeter placement of endothelial cells in two dimensional patterns. The controlled generation of droplets requires a fine balance of bioink properties like surface tension and viscosity with the printing mechanics including nozzle diameter and the actuation forces. Inkjet printing is capable of precision bioprinting, however the bioink requirements constrain material and cell choice[51,53,54].

Like inkjet bioprinting, extrusion bioprinting employs a method of computer-controlled material deposition. Instead of discrete droplet generation, extrusion printers rely on deposition of material through a nozzle. A bioink is driven through a nozzle using pneumatic, piston, or screw driven forces. Bioinks are typically shear-thinning, exhibiting a decrease in viscosity with an increasing share rate[53,55]. Additional crosslinking mechanisms such as photopolymerization or ionic crosslinking can be used to further strengthen the extruded material[56]. Extrusion based bioprinting is one of the most common bioprinting methods used due to the accessibility of printers and the wide variety of bioinks available. Drawbacks include the interdependence of print resolution on the rheological and crosslinking properties of the bioink as well as the nozzle diameter and printing dynamics. Achieving high resolution (<100 μm) typically requires smaller nozzle diameters. However, smaller nozzles increase the shear force applied to the bioink, which can negatively impact cell viability due to the stress imposed on cells during the extrusion process[55,57]. As a result, extrusion bioprinting is typically limited to resolutions on the order of 100-200 μm dependent on the bioink properties and printer[53].

3D printers using material deposition are in part limited by the material properties of the bioink and the dynamics of the deposition process[53,54]. Light-based methods offer a different set of advantages and constraints. The use of light to generate structures presents a wholly different approach for generating structures; here, resolution is a product of the optics, exposure, and resin chemistry[58–61]. Light based printing is amenable to biological applications by using biocompatible resins and biocompatible wavelengths of light as discussed further in section 2.2.

The first cell-laden SLA bioprint was accomplished using a commercial printer (SLA-250; 3D Systems) and a poly(ethylene oxide) hydrogel scaffold with a 2-methyl-1-2-methyl-1-

propanone (Irgacure 2959) photoinitiator. Chinese hamster ovary (CHO) cells were suspended in the liquid resin and the printer laser exposure was used to sequentially cure a cell laden structure. The resolution was found to be approximately 250 μm in the xy plane and 150 μm in the z dimension, surpassing most extrusion based methods without subjecting cells to significant shear forces [62].

Additional biocompatible resins, printing methods, and cell types have been demonstrated. Common printing polymers include PEG-DA[63–65] and GelMA[66,67]. Several methods of light control can be used to photopolymerize structures including laser scanning in SLA [63,66] and digital light processing (DLP)[67,68]. Several cell types have shown to maintain viability through the printing process including endothelial[69,70], myoblasts[70], bone marrow stromal cells[70], *E. coli*[68], and *Caulobacter crescentus* [68]. Printed structure applications using SLA or DLP include systems to model liver cancer[71], breast cancer[66], and heavy metal sensing[68]. Although light-based printing provides advantages in resolution and flexibility in material rheological properties, toxicity of the photopolymerization process and light exposure are of concern (see Section 2.2).

The aforementioned bioprinting techniques summarize a small subset of the methods developed since the 1980's. Bioprinting is a quickly moving field which has demonstrated a myriad of technologies and applications in just a few decades. Academic researchers have demonstrated wide ranging applications including tissue models, cancer models, and drug discovery models[53,54,72]. These applications are beginning to be commercialized, with a number of companies developing dedicated 3D bioprinting systems and materials for commercial use[73].

Advances in materials science, biology, and engineering will continue to drive advancements in the field of bioprinting.

2.1.6 Recent Innovations and Current Challenges in Microbial Bioprinting

While most efforts in 3D bioprinting originally focused on tissue engineering applications in the domain of microbial cell bioprinting are growing. In fact, many publications mentioning "bioprinting" and "microb*", "microorganism*", or "bacteria" have been published in the last four years (Figure 2.1). The technologies developed for tissue engineering are highly applicable to the study of microbial structures as both involve the manipulation of living cells in soft, biocompatible matrices.

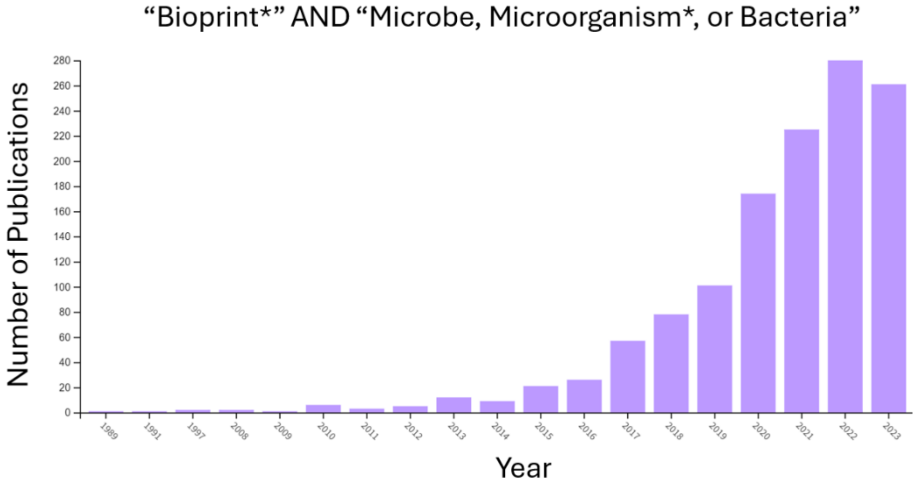

Figure 2.1. Number of publications related to the bioprinting of microbial organisms. A bar chart depicting the number of scientific publications within the Web of Science data base that include "Bioprint*" and "Microbe, Microorganism*, or Bacteria".

3D printing of microbially laden structures offers a new dimension to microbiological research. The ability to control the shape and composition of cell laden structure enables a number of investigations not previously available to researchers. For example, resilient biocompatible structures were created using a glycidyl methacrylate hyaluronic acid (GMHA) polymer modified with biopolymers k-carrageenan (k-CA) and fumed silica (FS) to adjust the viscoelastic properties. This produces a bioink termed “Flink”, which exhibits desirable rheological properties for bioprinting and is capable of maintaining the viability of both *Pseudomonas putida* and *Acetobacter xylinum*. Extrusion printing of a hyaluronic acid (HA) bioink laden with *P. putida* generated living structures with the ability to degrade phenol[74].

There are several examples of using microbial 3D bioprinting to create living structures laden with microbes. However, few examples exist for structures printed with biofilm-relevant geometries, and the biofilm geometry presents a specific set of challenges. Biofilms are typically on the order of 1-1000 µm thick[75,76]. Many bioprinting technologies developed for tissue engineering have effective resolutions between 100-1000 µm, capable of mm sized features but challenged to control sub millimeter geometry and composition at all biofilm relevant length scales[54].

Extrusion printing of an alginate hydrogel was used to create biofilm model structures ranging from 250 µm to 4 mm in thickness with multiple encapsulated bacterial strains including *E.coli, P. aeruginosa,* Methicillin-sensitive *Staphylococcus aureus, and* Methicillin-resistant *Staphylococcus aureus*. This study demonstrated the capability for printed microbial structures to display biofilm like behaviors (e.g. biofilm formation and dispersal) and the ability for the models to be used in antibiotic susceptibility testing[77]. Resolution was, however, limited by the printability of the bioink, and a minimum thickness of 250 µm is representative of only relatively thick self-assembled biofilms. Furthermore, the printing process and observation workflow required the physical manipulation of the printed structure which the authors found to be impossible with constructs thinner than 0.5 mm[77].

Bioprinting living systems for study requires an integrated workflow which considers aspectsfabrication, culturing, and observations of printed structures. There is an inherent tradeoff between the viability of embedded cells and the stiffness of the hydrogel matrix in bioprinting[49,78,79]. Consequently, processes that require the structures to be physically manipulated, especially structures that exhibit biofilm geometries (<0.5 mm thickness), may not be conducive to further observation due to the lack of structural stability[77]. Methods which print onto glass slides or other stiff substrates may be more amenable to continued observation.

A light-based bioprinting technique using Gel-MA scaffolds and a custom upright DLP system was used to produce biofilm-like structures containing both *E. coli* and *C. crescentus*. The system printed hydrogels onto glass slides with resolution on the order of 10 μm with structure thickness 10-200 μm. The light-based bioprinting process demonstrated both high resolution and the ability to print multiple *E. coli* strains within the same structure. Furthermore, the authors demonstrated the ability for printed structures containing *C. crescentus* to absorb neodymium as well as a *C. crescentus* strain containing a uranium-responsive promoter was used to demonstrate a simple biological uranium biosensor[68].

2.2 Introduction to Light-Based Vat Polymerization 3D Printing

Light based 3D printing involves the use of light to additively create structures. These instruments employ components like lasers, galvanometers, and digital light projection to direct light accurately and precisely, enabling the fabrication of intricate structures. Light-based 3D printing techniques include processes such as selective laser sintering (SLS), selective laser ablation, and vat polymerization[80]. In this chapter, I will focus on vat polymerization, which includes variations of stereolithography (SLA), digital light processing (DLP) and masked stereolithography (MSLA), which is also referred to as liquid crystal display (LCD) printing. All of these printing subtypes use similar resins but use different methods of selectively curing resin such as a scanning laser (SLA), a light projecting mirror array (DLP), or an LCD mask (MSLA) (Figure 2.2). The work described in this thesis focuses primarily on SLA 3D printers, but much of the information is broadly applicable to vat polymerization.

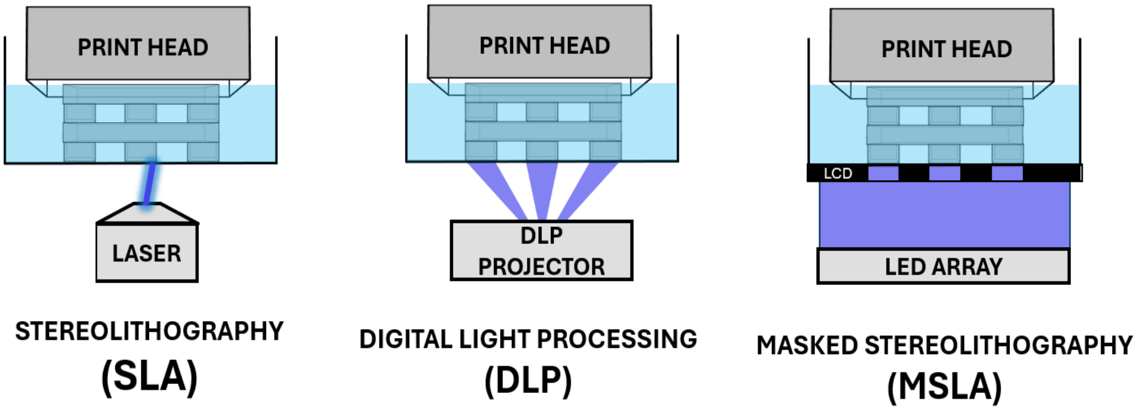

Figure 2.2. Schematic of light-based vat polymerization methods. (Left) Stereolithography (SLA) uses a laser to selectively cure resin. Computer controlled galvo mirrors precisely direct the laser along a 2D path. (Middle) Digital light processing (DLP) uses a micro-mirror array to direct light from a light source in a 2D image formed by the mirrors onto the resin, selectively curing the image. (Right) Masked stereolithography (MSLA) 3D printing uses a liquid crystal display (LCD) to block light.

Vat polymerization is the most commonly used light-based bioprinting technique due to its capability to print at ambient temperatures with biocompatible materials[80]. Vat polymerization 3D printing can be categorized into two approaches: upright and inverted.

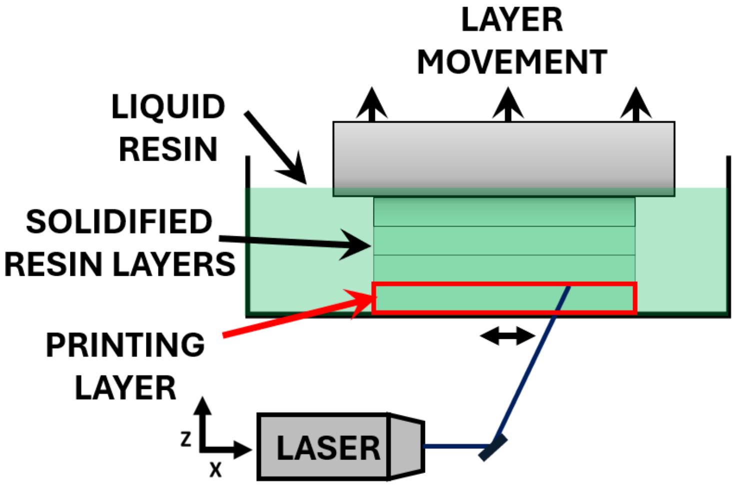

Figure 2.3. Schematic of inverted SLA vat polymerization 3D printing. A vat of photoactive liquid resin is selectively photopolymerized by a specific wavelength laser (e.g. 405 nm). The selective curing in the xy plane produces a 2D cured pattern (labeled in red). Layer movement in the z-direction moves the print platform one layer height. Additional layers are photopolymerized to add to the structure, producing a 3D object.

Upright printing was the first process to successfully additive manufacture polymer systems[54,81]. In this process, a print platform is fully submerged in a vat of photoactive resin, with a thin film of resin between the top of the print platform and the upper air-liquid surface of the resin. The layer of resin above the platform is exposed to 2D patterned light, polymerizing the liquid into a solid. The platform then lowers another layer height, and the process is repeated. By contrast, inverted vat polymerization lowers a print platform into the vat, leaving one layer height between the lower surface of the platform and the bottom of the vat. Light exposure polymerizes the layer to the print platform. However, polymerization of the print layer can create adhesion between the polymerized material and the vat bottom as depicted in Figure 2.3. Thus, the structure must be “peeled” from the bottom of the vat. Forces associated with the layer separation contribute to print failures in inverted vat polymerization and must be carefully managed during the printing process. Low surface energy materials or oxygen permeable materials are typically used to coat the vat bottom. Fluorinated materials like fluorinated ethylene propylene (FEP) offer low adhesion. Oxygen permeable materials like PDMS offer pliability while also introducing oxygen to the interface. Most photopolymerization processes are carried out by free radical polymerization, and oxygen limits this process by scavenging free radicals thus mitigating polymerization at the vat bottom[82].

2.2.1 Considerations for Adhesion and Alignment in Inverted Vat Polymerization

In vat polymerization 3D printing, the first print layer(s) adheres directly to the print platform, forming the foundation of the structure. These initial "burn-in" layers are critical for print success, as poor adhesion can lead to defects or failure. Multiple burn-in layers, also referred to as early layers or bottom layers, are typically used in inverted vat polymerization to improve adhesion, as increased exposure is likely to strengthen layer-layer bonds and attachment to the print platform[83–85]. It is generally recommended that the exposure time for these early layers be approximately 8–12x longer than the standard exposure time for the specific resin[86,87]. In prints > 1 mm, particularly those using sacrificial support rafts, the increased exposure of early layers does not affect the overall structure. The support raft absorbs any excess curing or additional layer thickness, serving as a buffer between the print platform and the printed model which references the vat bottom for the remainder of the layers (Figure 2.4). However, in prints where support rafts cannot be used, increased exposure in the early layers may lead to reduced resolution and off-target polymerization, potentially compromising the accuracy of the final structure.

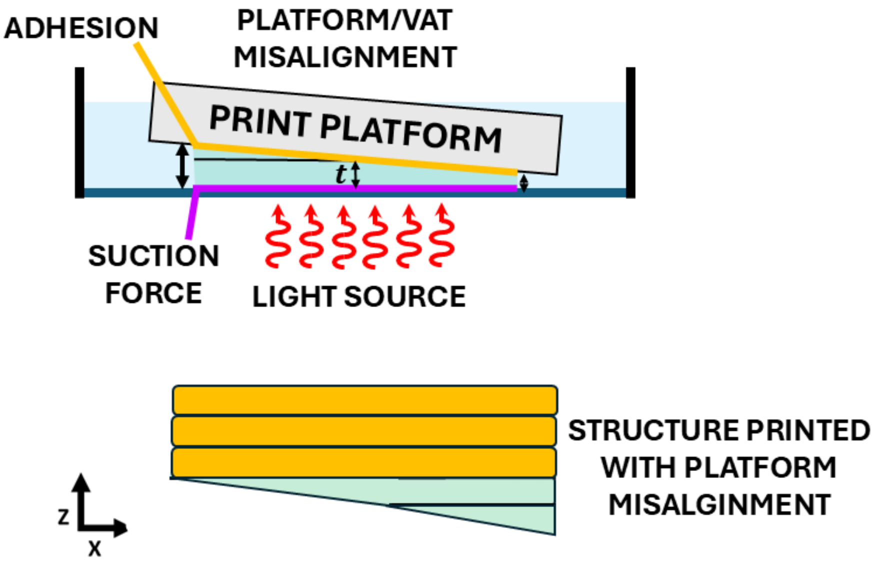

Figure 2.4. Schematic of print platform misalignment in vat polymerization 3D printing. (Top) Misalignment between the plane of the print platform and the plane of the vat bottom may induce uneven early layers. The suction force occurs at the interface of the polymerized layer and the vat bottom (magenta). Adhesion of early layer(s) to the platform provides the base of the printed structure (orange). (Bottom) Example of early layer unevenness created by platform misalignment (green). Even layers are produced once the misalignment has been "absorbed" by the early layers (yellow).

While managing early layer adhesion and layer exposure is critical, a separate challenge can arise from print platform misalignment (Figure 2.4). Manual leveling of the print platform is typical to consumer grade inverted vat polymerization printers[88,89]. This method does not precisely control platform height or parallelism, meaning the platform may be tilted or incorrectly positioned at the start of the print process. This misalignment can cause variability in the gap between the platform and the vat bottom, resulting in inconsistencies in the uniformity or the actual height of the early layer(s).

To compensate for this misalignment, multiple burn-in layers are often employed. Overexposure of multiple layers ensures a strong bond between the printed object and the platform, even in areas initially affected by the misalignment (green layers, Figure 2.4). Once the object's thickness exceeds the misalignment, the effects become negligible, and the rest of the layers reference the plane of the vat bottom (yellow layers, Figure 2.4). For larger prints, this misalignment is often absorbed by the sacrificial raft or is inconsequential to the structure itself, causing minimal disruption to the print. However, when printing thin structures (i.e. print thickness ≈ misalignment length scale) or structures without sacrificial rafts, the impact of print platform misalignment becomes more significant. When printing biofilm-like geometries (i.e. 3-300 µm in thickness) avoiding this misalignment becomes intractable. High-precision alignment between the printhead and the vat can be achieved through the use of precision hardware. However, due to the high cost and complexity of these systems and the typical use of sacrificial raft structures, such precision is uncommon in consumer-level 3D printers.

2.2.2 Photoactive Resins for Bioprinting

While light-based vat polymerization 3D bioprinting requires the use of specialized biocompatible resins, the printing process remains largely unchanged. Bioprinting resins typically have three main components, though more may be added to modify printability or biocompatibility[56,64,90]. The three core components are the polymer precursors (monomers, oligomers, or polymers), photoinitiator, and photoabsorbers[64,91]. In this work I focus on the use of free radical photopolymerization via the photoinitiator, lithium phenyl-2,4,6-trimethylbenzoylphosphinate (LAP). Additional methods of photopolymerization (e.g. cationic photopolymerization) and several photoinitiators have been demonstrated in light-based bioprinting systems.

Precursors

Precursors are typically composed of acrylate-modified monomers or oligomers. Polymer precursors can react through a variety different mechanisms including acrylate, epoxide, and thiol-ene based chemistries[90,92]. Given the abilities of synthetic chemists, polymer precursors can be modified in a number of ways to provide unique and tailored mechanical, chemical, or biological properties. Common photopolymers are polyethylene glycol diacrylate (PEG-DA) and gelatin methacryloyl (GelMA)[64,68,90]. In this work I focus on the use of acrylate-based resin systems due to their well-established cytocompatibility and printability using inverted stereolithography bioprinting methods.

Photoinitiators

Photoinitiators initiate the polymerization process and are essential components in light-based 3D print resins. Upon exposure to specific wavelengths of light, photoinitiators undergo chemical reactions, typically Norris Type 1 (direct cleavage) or Type II (electron transfer with a co-initiator), which generate free radicals. These radicals start the polymerization chain reaction. In bioprinting, photoinitiators must balance properties including solubility, efficiency, and biocompatibility. Efficient photoinitiators reduce the amount of initiator and light dosage required. This efficiency can include quantum efficiency, or the ratio of reactive species generated to the number of photons absorbed. Higher quantum efficiencies are generally preferred in bioprinting as this reduces the required concentration of photoinitiator and the light dosage, improving overall biocompatibility.

Water-soluble photoinitiators like lithium phenyl-2,4,6-trimethylbenzoylphosphinate (LAP) and Irgacure 2959 (2-hydroxy-1-[4-(2- hydroxyethoxy) phenyl]-2-methyl-1-propanone) are both type I photoinitiators that cleave to form free radicals when exposed to UVA and near UV light [93]. LAP has a peak absorbance at a wavelength, λ = 375 nm but is also responsive to λ = 405 nm, making it versatile for various light sources in bioprinting applications[64,94]. LAP has gained popularity due to its high water solubility, relatively low toxicity, and high quantum efficiency. Irgacure 2959, while also widely used, generally requires higher concentrations to achieve efficient polymerization and can pose greater cytotoxicity risks, especially at higher concentrations[94,95].

Eosin-Y, a type II photoinitiator, has also been used in bioprinting, offering advantages such as improved biocompatibility compared to Irgacure 2949. With an absorbance peak within the visible light spectrum (λ = 514 nm), Eosin-Y enables the use of less harmful wavelengths of light to improve cell viability while s till facilitating effective polymerization[60].

Photoabsorbers

Photoabsorbers (or photoblockers) control the penetration of light into the resin via absorptions. Controlled light attenuation enables technicians to modify resin and printing parameters to control cure depth and achieve high-resolution structures without over exposure (see Section 3.1.3). This ensures that polymerization occurs only in the targeted areas, allowing for high-resolution prints and the creation of fine, detailed structures.

Photoabsorbers used for bioprinting include natural and synthetic food dyes that absorb specific wavelengths. For example, tartrazine, a yellow food dye with an absorbance peak around λ = 405 nm, is frequently used due to its biocompatibility and solubility. Moreover, its water solubility and low reactivity enables it to be removed from the print after polymerization, leaving behind a clear polymer structure[96]. Additional photoabsorbers like curcumin and chlorophyllin, have demonstrated predictable light absorption and the ability to be used in water based bioprinting resin formulations to create high resolution structures[91,96].

2.2.3 Photopolymerization of Acrylate Based Resins

PEG-DA is a synthetic gel-forming, polyethylene glycol-based polymer formed by substitution of terminal hydroxyl groups with acrylate, which readily react with free radicals. This reactivity provides the basis for polymerization wherein free radical reaction with the acrylate group initiates a stepwise chain reaction. This polymerization process is termed “free radical polymerization” and occurs in three steps: initiation, propagation, and termination. Initiation occurs when a free radical reacts with an acrylate group. The free radical-acrylate reaction transfers the radical to the monomer, forming a new radical, beginning propagation. The radical continues to react with other acrylate groups, growing the polymer chain in a stepwise chain reaction. Chain growth stops once two free radicals meet and combine in a chain-termination step[97,98]. Free radicals can be controllably generated by a Norrish type I α-cleavage reaction under specific wavelength light irradiation[97]. If sufficient free radicals are produced, a polymer gel network is formed. This mechanism is widely used in manufacturing and applications such as coatings, dental fillers, contact lenses, and 3D printing[97,99]. Photopolymerization through free radical polymerization is a dynamic chemical process. The balance of initiation, propagation, and termination controls the ultimate polymer material properties and the printability and resolution during 3D resin printing.

2.2.4 Biocompatibility of Light Exposure

Light is capable of damaging living systems. Many humans are intimately familiar with the destructive capabilities of ultraviolet (UV) light (e.g. sunburns). Approximately 10% of the sun's electromagnetic radiation falls within the UV range (λ = 100 - 400 nm); however, nearly all UVC radiation (λ = 100 - 280 nm) and most (~95%) of UVB (λ = 280 - 315 nm) radiation is absorbed by the Earth's atmosphere[100]. The effective blocking of UVC and UVB by the atmosphere is critical to life on Earth's surface and is widely implicated in human and environmental health.

UVB radiation is largely responsible for sunburns, causing damage through mechanisms like the fusion of pyrimidine base pairs in DNA and the generation of reactive oxygen species (ROS), which can disrupt intracellular DNA replication and repair processes[101]. UVC, with shorter, higher energy wavelengths, is damaging enough to be employed as a germicidal tool in hospitals and laboratories due to its ability to cause cellular damage through similar mechanisms[102]. UVA (λ = 315 - 400 nm) is less readily absorbed by DNA and is thus less likely to cause direct DNA damage like UVB and UVC[103]. UVA can, however, induce cellular damage through indirect mechanisms[104].

Resin based printing commonly employs near-UV light sources for photopolymerization, with λ = 405 nm being the predominant wavelength due to its availability, safety, and compatibility with photoinitiators[68,105]. While λ = 405 nm is considered a violet light and is part of the visible spectrum (380 nm $\leq \lambda \leq$ 750 nm), λ = 405 nm light sources may emit light into the UV range dependent on the spectral bandwidth of the light source. Notably, λ = 405 nm light has been shown to have bactericidal properties, in part due to its ability to induce the production of ROS within bacterial cells, leading to cellular damage and death. Murdoch et al. found that this antimicrobial action is dose-dependent, reporting that *E. coli* and *S. aureus* can be inactivated at doses as low as 7.2 J/cm^2, with greater inactivation at higher light doses. Light exposure required for photopolymerization is, typically lower than the does reported for inactivation, requiring less than 1 J/cm^2 for photopolymerization[106].

Similarly, Chen et al. investigated the use of $\lambda = 405$ nm light as an antimicrobial treatment and found that prolonged light exposure over 48 hours resulted in several bacterial strains' inactivation. *S. aureus* and *Pseudomonas aeruginosa* were the most sensitive while gram-negative bacteria including *E. coli*, *Listeria monocytogenes*, and *Salmonella Typhimurium* were more resistant. The study suggests these differences could stem from variations in endogenous porphyrin production, which influences the generation of ROS. Notably, inactivation of bacteria continued to decrease with no plateau after 48 hours of continuous exposure (86.4 J/cm^2), indicating that higher doses of $\lambda = 405$ nm light, though not typically used in bioprinting, can be highly detrimental to bacterial cells. This highlights the potential for light exposure to impact bacterial physiology, even if viability is maintained[107]. Non-fatal biological effects of light exposure and the associated polymerization effects should not be overlooked. Significant physiological changes across various cell types have been documented in response to different wavelengths and intensities of light exposure, underscoring the complex biological interactions that can occur in these settings[108–110].

2.2.5 Biocompatibility of Free Radical Photopolymerization

Free radical photopolymerization occurs through the generation of free radicals by the photoinitiator and the subsequent initiation of a polymerization chain reaction. Type I photoinitiators activate through a cleavage mechanism, wherein specific wavelengths of light cause the dissociation of a photoinitiator into two free radicals following photon absorption. Type II photoinitiators may also drive photopolymerization but work through a different mechanism of hydrogen atom abstraction from a secondary co-initiator species when the photoinitiator becomes excited.

In this work I focus on type I photoinitiators with a specific focus on the biocompatible photoinitiator, lithium phenyl-2,4,6-trimethylbenzoylphosphinate (LAP). LAP is a acylphosphinate salt with an absorbance peak around $\lambda = 375$ nm but with measurable absorbance above $\lambda = 400$ nm[64]. When LAP absorbs light of the appropriate wavelength, it dissociates into two free radicals, which initiate free radical polymerization in acrylate-based resins. While effective for resin polymerization, free radicals generated during this process can also interact with biological components like cell membranes, nucleic acids, and proteins. These interactions occur either directly or through the formation of reactive oxygen species, which can damage living cells[111].

Multiple studies suggest that free radical flux is a likely source of toxicity in photopolymerization systems. A study exploring the effects of a type I photoinitiator, Irgacure 2959, and $\lambda = 365$ nm light on human aortic smooth muscle cells (HASMCs) found that while exposure to the UVA light did not significantly affect cell viability, incubation with varying levels of the photoinitiator, without UVA exposure, did result in a decrease in cell viability. The addition of UVA exposure, with photoinitiators, resulted in an ever-greater decrease in cell survival. This study suggests that light is not the primary source of cytotoxicity in this photopolymerization system[95]. A similar study assessed the cytotoxicity and mutagenicity of LAP and $\lambda = 405$ nm light on both mammalian (M-1 mouse collecting duct cells) and bacterial cells (*S. typhimurium* TA98 and TA100). These results suggest that LAP in the presence of light is cytotoxic while exposure to $\lambda = 405$ nm light alone is not cytotoxic. Moreover, a modified

Ames bacterial mutagenicity assay found no evidence of mutagenicity at concentrations of LAP and light exposure associated with significant cytotoxicity, suggesting the photopolymerization process is not mutagenetic for the studied system[92].

Research investigating a GelMA-Irgacure 2959 resin system looked at the interplay of photoinitiator concentration and light intensity on photopolymerization. The researchers' model of free radical generation suggests that reducing light intensity during the photo crosslinking process effectively lowers the free radical flux [112]. While this reduction in light intensity does lead to longer cure times, it can reduce the free radical stress experienced by embedded cells. Furthermore, the total light energy (E_{total}) required to polymerize the photopolymer system is proportional to the square root of the light intensity divided by the photoinitiator concentration (Eq. 2.1).

$$E_{total} \alpha \sqrt{\frac{I_0}{c_i}} \qquad \text{(Eq. 2.1)}$$

Where E_{total} is the total light energy required to complete photopolymerization, I_0 is the light intensity, and c_i is the photoinitiator concentration[112]. This equation indicates that higher light intensities require more total energy to achieve the same level of crosslinking. Therefore, while lower light intensity may prolong the cure time, they can significantly decrease free radical flux and overall light exposure, thereby reducing potential cell stresses [64,112]. These results together suggest that when working with biological systems, which benefit from lower light intensities and lower levels of free radical stress, a minimum level of light intensity should be used to achieve curing, thereby reducing the incident intensity and free radical generation. Moreover, free radicals and reactive oxygen species impact physiological processes in both prokaryotic and eukaryotic cells, influencing a broad spectrum of biological functions and stress responses[111,113].

Several photopolymerization resin systems exist. A select few have been shown to be suitable for bioprinting applications[114,115]. Visible light photoinitiators have also been developed and could serve beneficial for bioprinting applications as well as providing opportunity for multi wavelength printing systems[116]. The continued innovation of photopolymerization and polymer resin systems for bioprinting will provide new and better opportunities and capabilities to the field of biofabrication. Better biocompatibility, printability, and accessibility will provide more adequate platforms for the generation of additively manufactured living structures.

2.2.6 Multi-Material Printing

Multi-material 3D printing enables the creation of more complex structures with controlled continuous or discrete variation of mechanical, chemical, or biological properties. This is particularly relevant to the creation of synthetic biofilms as naturally formed biofilms often exhibit many levels of heterogeneity in material, chemical, and biological properties[2,24]. Replicating this heterogeneity *in vitro* may be crucial for advancing biofilm research.

Several techniques have emerged to facilitate multi-material 3D printing using photopolymerization. Han and Yang (2019) introduced a fluidic cell system for projection micro-stereolithography, enabling fast switching between photoactive polymers at the microscale[117]. Kowsari et al. developed a DLP-based system with an air jet to remove residual resin, minimizing waste during material exchange and allowing multi-resin printing[118]. Miri et al. used microfluidics for fast switching between bioinks, such as PEG-DA and GelMA, to print complex biological models, while Mayer et la. and Wang, Li, et al. integrated microfluidic systems to achieve controlled material gradients and precise resin flow and mixing[119–121]. All systems mentioned utilize various methods of resin exchange, where the printing resin is removed, rinsed with a fluid (e.g. solvent or air), and replaced with a different resin between layer exposures. These techniques enable the fabrication of structures with multiple materials which can include different polymers[117], different cell species[119,121], and different functional compounds[121].

2.3 Considerations for Confocal Microscopy in Biofilm Research

2.3.1 Principles of Confocal Microscopy

Confocal microscopy is a powerful imaging tool widely used across the biological sciences including research of microbial communities and biofilms. The strength of confocal microscopy lies in its use of a pinhole aperture to eliminate out-of-focus light, effectively sectioning the sample optically. Confocal micrographs are collected point by point, typically observing fluorescent molecules that have tagged or stained specific molecules, cells, or processes[122]. Fluorescent stains like SYTO 9 and propidium iodide provide a simple live/dead stain for differentiating between live and dead cells[123]. The library of fluorescent reporters and labels is rapidly advancing, and now there are reporters that allow for the observation of; gene expression[27], metabolism[124], pH[125], substrate concentration[126], and even target nucleic acid sequences of specified species[127].

Although the use of a pinhole enables optical sectioning and the ability to image “into” thick samples like biofilms, confocal microscopy is still limited by certain aspects of light and its interactions with the sample. Light attenuation is a common challenge for imaging biofilms, both natural and synthetic[122]. Light absorption and light scattering of embedded cells and other materials (e.g. EPS) causes an inability to resolve structures beyond a few hundred microns into a biofilm, dependent on cell densities and the light interacting molecules present[122,128,129]. Therefore, very thick or very dense biofilms become difficult to image using conventional microscopy or confocal microscopy methods with some imaging becoming compromised in as little as 50 μm of biofilm[122]

2.3.2 Practical Considerations for Imaging Biofilms

In this subsection, I describe the use of confocal microscopy as the primary tool for observing depth-dependent structures and the dynamics of biofilm growth. Through the collection of image stacks across the thickness of these synthetic biofilms, we can observe, document, and create digital 3D representations of these synthetic biofilms.

Quantitative confocal imaging of synthetic biofilms, produced through 3D printing, demands precise experimental setups and careful acquisition of micrographs. The accuracy of quantitative analysis using confocal microscopy hinges on the control of various parameters to ensure consistent, reliable data across different experimental conditions. Key parameters include scan speed, laser intensity, pinhole size, zoom, and z-thickness step size[122]. Briefly, scan speed controls the dwell time for each pixel and is analogous to camera exposure time. If the scan speed is too slow, the longer dwell time can increase the risk of photobleaching or image saturation, while a scan speed that is too fast may not collect sufficient data for accurate quantitative or qualitative microscopy[122]. Laser intensity roughly controls the number of photons exciting the sample. The correct laser intensity will depend on the fluorophore being excited, the sample's propensity for photobleaching, and the thickness or density of the sample[122].

The pinhole size controls the optical section. Smaller pinhole diameters result in less out of plane light collection. The pinhole size is a balance of light collection and axial resolution.

Confocal zoom reduces the scan angle of the laser which in turn reduces the scanned area of the specimen[122]. This effectively increases the sampling frequency, capturing the same number of pixels within a smaller sample area. Too much zoom can however lead to oversampling[130]. The final core parameter is that of z-thickness, or the step size in between each optical section of an image stack. This parameter is crucial for producing z-stacks and accurate quantitative analysis. The optimal step size will depend optically on the axial resolution of the objective, wherein Leica machines now offer an automatic step size optimization, typically producing a step size between 1-2 µm. A decrease in step size can increase axial resolution but also can lead to increased imaging times, oversampling, and potential for photobleaching[122].

CHAPTER THREE

SYNTHETIC BIOFILM PRINTING METHODS AND METHODOLOGY

3.1 Synthetic Biofilm Bioprinting

This chapter explores light-based bioprinting techniques and the printing of synthetic biofilms. As described in Chapter 2, biofilms are surface associated microbial communities that inhabit nearly every interface on Earth[2]. Biofilms are ubiquitous in human health and industrial problems and offer potential for biotechnology applications[10]. However, current methods to study biofilms laboratory settings are limited. 3D bioprinting offers a promising tool for cultivating biofilms *in vitro* and thereby advancing biofilm research.

3D bioprinting of biofilms presents unique challenges, such as replicating the geometries and length scales of typical self-assembled biofilms, achieving heterogeneities common to biofilm systems, and meeting the requirements of effective observation and analysis following bioprinting. In this section I introduce an innovative approach to 3D bioprinting of biofilms, leveraging a simplified, idealized biofilm geometry (e.g. flat slab) to facilitate the controlled generation of synthetic biofilms. This methods section supplements the methods detailed in chapter 4.

3.1.1 Direct to Glass Printing via Direct Laser Writing

To address these challenges, direct-to-cover glass printing via direct laser writing is proposed as an alternative. In this method, the PEG-DA based bioresin is applied to a glass bottom petri dish or well plate. A modified SLA 3D printer is then used to selectively polymerize a structure directly onto the bottom of the cover glass. This technique eliminates the need for a traditional print platform, thereby addressing the issues of suction forces and platform adhesion that often require additional light exposure for early layers. By removing the print platform entirely, this method also eliminates the problem of platform misalignment. Instead, the glass substrate serves as the reference surface, allowing for the creation of thin films without the inconsistencies associated with platform misalignment (see section 2.2).

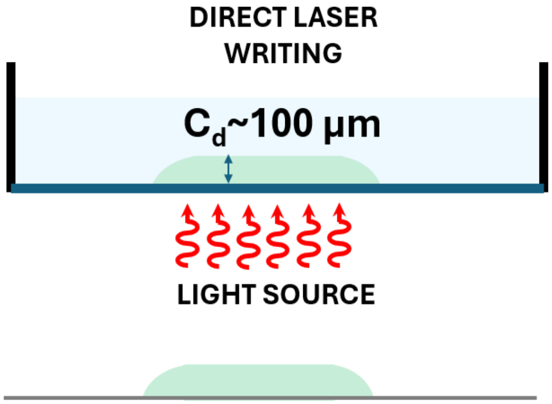

Figure 3.1. Direct-to-glass laser writing photopolymerization. Layers of resin are cured without the use of a print platform. Cure depth (C_d) is controlled using light exposure and resin composition. This method avoids issues associated with the suction force and print platform misalignment.

This approach, akin to direct laser writing or maskless lithography, is well suited for printing thin films but is not applicable to structures larger than ~1 mm in height. Layer height is controlled by photo absorbers in the resin and the laser exposure[91]. Beyond increasing layer uniformity and repeatability, printing into a well plate or petri dish also offers advantages in sterility and observation with microscopy. As bioprinting currently relies on custom built infrastructure, attaining sterile experimental setups is challenging, especially since most 3D printed polymers are not autoclavable and the crevices produced by the layered architecture provide locations for other microbes and contamination to reside. The use of off-the-shelf well-plates eliminates this issue and provides a sterile, accessible, repeatable, and reliable platform for bioprinting experiments.

3.1.2 Well Plate Thin Film Printing

Well plates are a ubiquitous experimental tool common to biology laboratories. Well plates are essential tools in high throughput experimentation and quantitative biology because they enable the simultaneous testing of multiple biological or chemical conditions in a compact and standardized format. Their design allows for efficient use of reagents, automation compatibility, and precise control over experimental conditions — all features crucial for reproducibility and scalability in research[131].

Well plates designed specifically for microscopy applications offer additional advantages for facilitating optical observation of individual wells. These plates are compatible with a wide array of light-based signals generated by the continuously expanding range of bioimaging techniques [27,124–126]. Inverted microscopy-enabled well-plates are particularly well suited for inverted light-based printing due to their optically clear glass bottoms and consistent manufacturing. These plates enable accurate light delivery for resin curing. Additional benefits include well-controlled cleanliness and sterility[132].

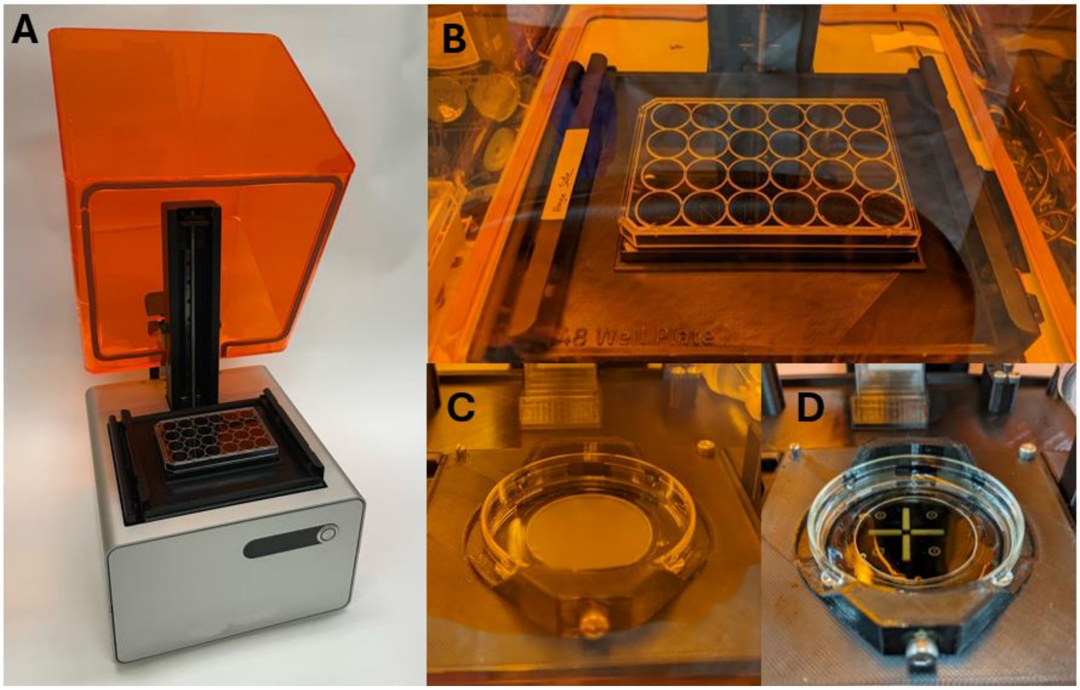

Figure 3.2. Direct to glass 3D printing hardware. (A) FormLabs Form 1+ SLA 3D printer with custom insert to hold multi well plates or petri dishes in position for light exposure. (B). 24 well plate in printing position. (C) Glass bottom petri dish printing setup during printing. A set screw provides repeatable positioning of the petri dish, enabling multi-material printing. (D) Cured structure after rinsing multi material printing process.

For bioprinting experimentation, we use commercially produced petri well-plates and petri dishes within a FormLabs Form 1+ printer as shown in the images in Figure 3.2. Custom machine adapters enable precise alignment and repeatable positioning of the well plates and petri dishes within the print build area. The integration of well plates with 3D printing experimentation creates a robust platform for generating models, testing multiple conditions, and producing replicates with high precision and repeatability. This standardized, sterile setup, common to many biological techniques, supports reproducibility and scalability in research[133].

3.1.3 Multi-Material Direct-to-Glass Printing

Multi-material 3D printing, as described in section 2.2.6, supports the creation of heterogeneous structures featuring discrete or continuous variations in properties such as material, chemical, and species[117119,121121]. Biofilm printing may significantly benefit from controlled heterogenous 3D printing given many self-assembled natural biofilms exhibit heterogeneity. Gaining the ability to fabricate multi-material or multi-niche synthetic biofilms (e.g. aerobic top layer with an anerobic bottom layer) may enable a wide and useful design space for engineering living systems.

To support these efforts, I have developed a method for multi-material thin film, direct to glass 3D printing using a simple method of resin exchange within the glass bottom wellplate or petri dish. In this method, a structure is printed with one resin, after which the resin is removed, the structure is rinsed, and a different resin added before the next light exposure. Multiple exposures within the same layer enable XY heterogeneity. This is depicted by the confocal microscopy tilescan of a PEG-DA hydrogel structure created using the well plate exchange of two resins containing red and green microspheres (Figure 3.3). Multiple layers may also be printed by exposing the same area (x, y location) twice with sequential resins to produce z heterogeneity (Figure 3.3B).

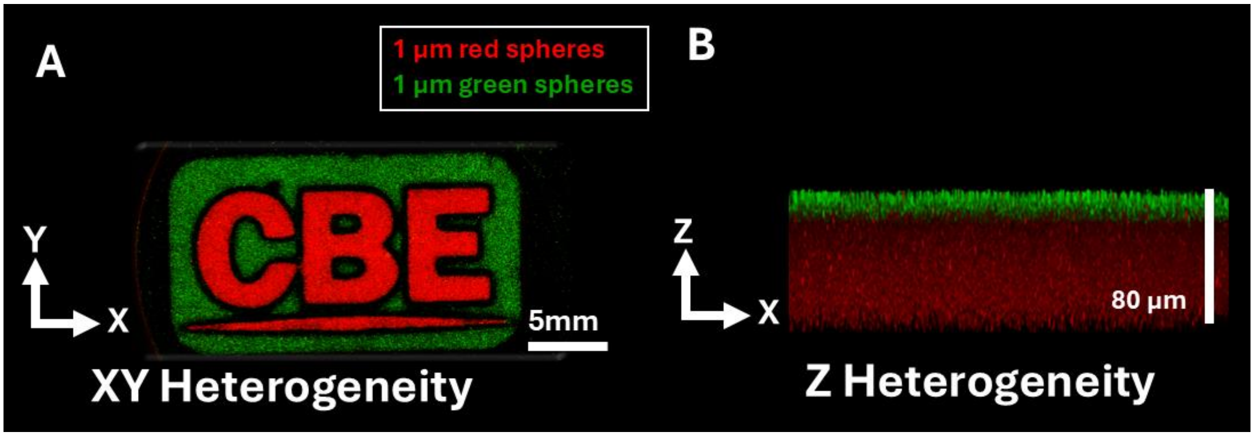

Figure 3.3. Heterogenous hydrogel structures demonstrate multi-material 3D printing using direct to glass method. (A) Hydrogel structure containing fluorescent microspheres of two colors printed with XY heterogeneity using resin exchange and multiple exposures. (B) Example of Z heterogeneity printing using similar procedure but exposing the same area twice.

To create a two-component structure, two similar resins containing 10% PEG-DA, 0.05% tartrazine photoblocker, and 0.01% LAP photoinitiator are mixed with 1 µm red poly(ethylene) microspheres (Thermo Fisher, R0100) and 1 µm green PE microspheres (Thermo Fisher, G0100) respectively. Each resin is vortexed just before printing to ensure microsphere dispersion within the resin.

For XY heterogenous printing, the red microsphere resin is added to a glass bottom petri dish (Mattek 50 mm, P50G-1.5-14-F). The first exposure, forming the letters “CBE”, cures the hydrogel with the red microspheres. The uncured red microsphere resin is removed from the dish before the cured structure is rinsed with deionized water three times. Following rinsing, the green microsphere resin is added to the dish and a second exposure of the outer border is performed. Any uncured resin is removed from the dish and the cured structure is submerged in water to maintain hydration. Inverted confocal microscopy using a 10X objective provides the image shown in Figure 3.3A**.** The process to create Z heterogeneity structure is similar in methodology except for a subsequent exposure of the second green resin in the same area as the initial red resin polymerization. Subsequent exposure penetrates through the gel and cures a thin layer of the green microbead resin on top of the already cured structure as shown in Figure 3.3B

The creation of Z heterogeneity poses additional challenges due to light attenuation through previously printed layer(s), affecting the incident light intensity and therefore polymerization of subsequent layers. Further investigation into the light attenuation and layer polymerization behavior is required to optimize this multi-material printing process. Overall, this method of multi-material printing offers a simple approach for printing microscale thin films with controlled XY and Z heterogeneity which can be applied to multiple applications including the production of heterogeneous synthetic biofilms.

3.1.4 Photopolymerization: Tuning Cure Depth

In light-based 3D printing, the precise control of light exposure is essential for controlling curing of photoactive resins. Achieving high resolution in 3D printing requires a fine balance of the resin properties — such as light absorption, photoinitiation, and polymerization— with the printer's light exposure including intensity, duration, and spatial precision. The resolution of light-based printing largely depends on the ability to locally contain the photopolymerization reaction. Several parameters must be controlled and modulated based on the specific printer and resin system in use. Key parameters include light intensity, light exposure time, photoinitiator concentration, and photoabsorber concentration. Several mathematical models have been developed to inform how light will interact with the resin and how the integration of the systems can be used to produce structures with precision and accuracy[91,115,134].

As light enters the resin, it is subject to absorption and scattering by components of the resin. A portion of incident photons are absorbed by the photoinitiator, triggering the free radical polymerization reaction. Without any other light absorbing species, the incident light may travel many millimeters through a resin, reacting with photoinitiators and polymerizing the gel[91]. The light exposure energy required to reach gelation can be described by the critical exposure energy (E_c), above which the resin becomes a gel, below which, the density of polymerization reactions is insufficient to cause gelation.

Cure depth (C_d) is the distance light penetrates the resin before falling below the critical energy required for polymerization (E_c). For instance, in a PEG-DA/LAP resin without photoblockers, C_d is around 1.85 cm with light exposure similar to that found in SLA printing[91]. For printing of small features (10-1000 µm), controlling light attenuation and cure depth is essential, requiring the addition of photoblocking species to the resin. The Beer-Lambert law models how light intensity decreases with depth into the resin, following exponential decay (Eq. 3.1).

$$E(z) = E_0 e^{\left(-z/D_p\right)} \qquad \text{(Eq. 3.1)}$$

Setting $E(z) = E_c$, and solving for C_d produces:

$$C_d = D_p * \ln\left(\frac{E_0}{Ec}\right) \qquad \text{(Eq. 3.2)}$$

This relationship suggests that the cure depth is directly proportional to the penetration depth and depends logarithmically on the ratio of incident light to the critical exposure energy. By adjusting E_0, E_c, and D_p using resin properties and printing parameters, one can precisely control C_d to achieve the desired printing resolution.

The Beer-Lambert law also expresses the relationship between absorbance (A), molar absorptivity (ε) and species concentration (c_b). In systems containing multiple absorbing species, such as photoinitiators and photoblockers, A can be described as the sum of contributions from both species:

$$A = (\varepsilon_b c_b + \varepsilon_{pi} c_{pi}) \qquad \text{(Eq. 3.3)}$$

Where ε_b and ε_{pi} are the molar absorptivities and c_b and c_{pi} are the concentrations of the photoblocker and photoinitiator, respectively. The relationship between the penetration depth, D_p, and the concentration of photoblocker and photoinitiator can then be described as:

$$D_p = \frac{1}{\varepsilon c_b + \varepsilon c_{pi}} \times \frac{1}{ln(10)} = \frac{0.4343}{\varepsilon c_b + \varepsilon c_{pi}} \qquad \text{(Eq. 3.4)}$$

This equation enables the estimation of cure depth based on the molar absorptivity and molar concentration of the chosen photoinitiator and photoblocker within the described PEG-DA resin system [64,91].

3.1.5 Print Profile Modification

While several bio-specific printers are commercially available, it is straightforward to modify standard 3D printers for bioprinting applications. The compatibility of a 3D printer for bioprinting depends on its light source, the resin system being used, and the ability to adjust critical printing parameters such as light exposure and laser settings. The modulation of printing parameters for a FormLabs Form 1+ SLA printer and a PEG-DA/tartrazine/LAP resin system will be discussed in this section. Similar modification and modulation may be possible with other printer and resin systems.

The FormLabs Form 1+ inverted SLA printer was selected for its open-source printing parameters and customizable material profile system. The open-source capabilities of the Form 1+ allows for users to generate material profiles that specify all parameters relevant to light exposure and the printing process. These parameters include laser power (*P*), laser velocity (*v*), laser scan line spacing (*S*), the number of laser exposures (*N*), and layer thickness (l_z). These values will vary widely between a standard engineering resin and a bioprinting resins, as well as among bioprinting resins with different concentrations of photoinitiator or photoblocker. The average incident exposure can be calculated by equation 3.5:

$$E_0 = \frac{PN}{Sv} \qquad \text{(Eq. 3.5)}$$

This equation assumes that repeated low power light exposures from multiple laser passes is equivalent to a single high power laser exposure[91]. For the printing described herein, all scanline spacing is fixed at $S = 0.09$. Modification of the exposure energy can be made by adjusting the other laser parameters. For example, to increase the exposure energy, the laser power can be increased, the velocity laser scanning can be decreased, or the number of laser passes can be increased. The combination of these parameters enables control over the incident exposure energy and therefore the dynamics of the polymerization reaction.

To achieve tailored printing outcomes with the Form 1+ 3D printer, specialized software and modified printing profiles are required. OpenFL, an open variant of the FormLabs slicer, is designed specifically for the purpose of enabling custom printing parameters. OpenFL must be installed on the computer used for print configuration and machine command upload[135].

To create custom material profiles, modifications to the OpenFL configuration files can be made. These files are used to configure machine parameters for different materials and therefore enable the modification of laser parameters and other machine commands like print platform speed and layer movements. The configuration files can be modified using a text editor like Notepad++. Users can modify settings such as laser power, scan speed, and the number of passes to optimize the printing parameters for specific resins. Once modified, these ".ini" files may be uploaded within the OpenFL slicer under “Load Custom Material” where they will be integrated during machine command generation and uploaded to the printer[135].

3.1.6 Bioprinting Post Processing

Light based 3D resin printing typically requires an extensive post processing workflow. During printing, structures are polymerized in a liquid resin bath, resulting in printed parts that are coated with unpolymerized resin after the process. For standard engineering resins, a solvent bath – most commonly isopropyl alcohol – is used to wash off the uncured resin from the printed structure[136]. In bioprinting, however, many resins are water-based, allowing aqueous solutions to be used for rinsing away uncured resin.

In the presented work, we use a process of rinsing with phosphate buffered saline (PBS) to remove uncured resin from the prints. This acts as an adequate washing solution to remove uncured resin while maintaining cell compatibility. Moreover, for photoblockers like tartrazine which are water soluble, post printing rinses can be used to remove some of the photoblockers from the polymerized structure, leaving translucent structures. In practice, the removal of photoblockers from polymerized structures requires 2-48 hours depending on geometry and thickness.

In light based bioprinting where microbial cells are added to the resin and printing occurs directly in the cell culture vessel (as described in “well plate printing”), microbes have an opportunity to adhere to and colonize the well outside of the polymerized hydrogel. In well plate printing of *P. fluorescens*, we observe that cells that begin outside or on the surface of photopolymerized structures are capable of colonizing the well plate and planktonically within the culture media. This additional growth of microorganisms outside of the gel may significantly impact experimentation, especially in batch culture, or when analyzing the bioprocessing capacity of cells embedded within the gel.

To mitigate the effects of non-embedded cell populations, we implement a short ethanol rinse with 70% ethanol as part of the post processing for this well plate printing process. Following three rinses with PBS, we submerge the printed structures in 70% ethanol solutions for approximately 10 seconds before removing the solution and immediately rinsing with PBS. This step is an attempt to kill bacteria not embedded within the gel that may have adhered to the well plate walls or exist on or near the surface of the gel and are liable to escape the gel and colonize the well plate. This is an imperfect method of removing unwanted microbial members as it may have off-target effects on the microbial members of interest.

3.2 Confocal Microscopy Characterization

3.2.1 Experimental Setup

Microscope objective choice is an important consideration and requires balancing resolution, field of view, and imaging throughput. In the studies described here, the 10x objective was selected for its ability to provide a substantial field of view (775 × 775 µm) while maintaining a manageable z-step size of approximately 2 µm. High magnification objectives offer increased resolution but drastically reduce the field of view and require smaller z-steps for image stacks, often doubling the number of required images per stack and significantly increasing the imaging time and the amount of laser exposure to the sample. Additionally, the working distance of the objective impacts the observable sample thickness. For example, the 10× objective used here provides a working distance of 7.8 mm, allowing for the imaging of very thick samples, while the 20× and 63× objectives have working distances of 0.67 mm and 0.15

mm respectively. When imaging very thick films, these working distances may limit the ability to image full film thickness.

In the observation of RFP expressing *P. fluorescens*, we begin imaging with maximum pixel values equal to roughly half of the dynamic range to allow for pixel intensity to increase with growth without finding pixel saturation. The amount to adjust initial imaging parameters will change with the system and the amount of growth. Full thickness, including additional space both below the gel and above the gel was included in each image stack to ensure that the entire thickness was imaged. Each gel image stack was manually selected as the cover glass bottom may change the relative bottom reference of each gel.

For time lapse imaging, images stacks were taken every one to two hours depending on the number of fields of view taken for the entire experiment. Imaging full format 512 × 512 with small z-step size can limit the overall throughput of imaging. Imaging time of more than 6 gels with multiple fields of view can require two hours or more to take z-stacks. Reducing the format from 512 × 512 pixels to 512 × 64 pixels is an option to reduce imaging time by roughly a factor of eight if the final format is not critical to the analysis. Reducing the number of timepoints to every two hours or more may be required depending on the number of wells and number of fields of view.

3.2.2 Image Analysis of Synthetic Biofilms

Image files and metadata like imaging settings and timestamps are imported into the Imaris software. These files are converted into .ims files. During preprocessing, techniques like Gaussian blur are applied to address challenges like light artifacts and enhance feature visibility. A Gaussian blur is a type of low-pass filter that smooths out high-frequency noise and details in an image. For the biofilm data described here, we are most interested in the general structure of the colonies more than any small features. A low-pass filter reduces this noise and allows the thresholding program to more easily resolve large colonies and get a better count on the structures that form within the biofilms.

Imaris Surface Thresholding

The Imaris automated surface tool is used to threshold and define volumes of fluorescent signals within 3D image stacks. This process involves applying the surface tool and configuring seed points for surface generation based on intensity thresholds. With static threshold values, changes in pixel intensity over time may cause thresholding to overestimate or underestimate biovolume in some conditions as relative intensities change. We instead allow for automated thresholding at each condition and each time point.

Imaris employs two thresholding methods, absolute intensity and background subtraction. Briefly, absolute intensity sets a fixed pixel intensity threshold, in which all pixels are considered part of the object of interest, and below which they are considered background. This method is simple and fast, but it can be affected by variations in signal intensity across the image or between different samples. As a result, it may not be the best choice for images with varying levels of signal intensity or for comparing images acquired under different conditions.

Background subtraction, estimates and subtracts the background signal from the image before thresholding[137]. This method can account for variations in signal intensity and provides a more accurate representation of the true signal from the object of interest. However, background subtraction can be computationally intensive and may require more advanced image processing techniques.

In general, absolute intensity thresholding is suitable for images with relatively uniform signal intensity and low levels of background noise, while background subtraction is more appropriate for images with varying signal intensity and higher levels of background noise[137]. Ultimately, the choice of thresholding method depends on the specific characteristics of the image data and the research question at hand. It may be necessary to try multiple methods and adjust the parameters to obtain the most accurate and reproducible results.

Object Splitting

Accurately quantifying individual cells or objects within overlapping or adjacent structures can significantly affect the outcome of image analysis. Imaris surfaces offer multiple integrated algorithms for segmenting adjacent or overlapping objects based on user-defined criteria.

Imaris will automatically generate seed points based on threshold values previously generated. The seed point size provides a user selected size of the minimum distance between two objects, this should be set to just smaller than the smallest individual object to be defined in the images. Imaris then uses these seed points as a basis for object splitting. Two main methods for splitting include: intensity-based split, which separates objects by setting a threshold for intensity differences, and morphological split, which uses operations such as erosion, dilation, and opening to separate the touching objects. Intensity-based split is fast and simple but may not work well for images with low contrast or complex morphology. Morphological split, on the other hand, is more flexible and can work well for complex images but may require more time and expertise to optimize the parameters[137]. More information on the algorithms used by Imaris and best practices for Imaris can be found in these references[137,138].

Following thresholding and object splitting, Imaris will generate object statistics. Many statistics are available for calculation including information on object intensity, location, size. Each statistic is presented as a data entry with an object ID. If object tracking was selected and successful, object ID can be used to track individual objects over the course of an experiment.

3.2.3 Data Pipelines and Analysis of Synthetic Biofilm Image Data

While Imaris software offers robust tools for data analysis and visualization, full utilization may require additional licenses. Alternatively, data exported from Imaris in CSV format can be analyzed using platforms like MATLAB, which facilitates further data manipulation and visualization. MATLAB scripts import CSV files of object statistics generated by Imaris. These files provide detailed information on the surfaces such as volume, intensity, location. MATLAB is used to import this data and concatenate it into usable data structures for visualization. Example codes of the data import and visualization are included in APPENDIX A. This represents an experiment specific code but should be modifiable to more general Imaris data for future experimentation.

CHAPTER FOUR

3D PRINTING OF SYNTHETIC BIOFILMS USING PHOTOLITHOGRAPHY

Contribution of Authors and Co-Authors

Manuscript in Chapter 4

Author: Isaak J. Thornton

Contributions: Technology development, bioprinting of biofilm models, conducted key experiments, confocal imaging, analyzed the data, and manuscript writing and editing

Co-Author: Kathryn R. Zimlich

Contributions: Conducted key experiments, microbiology including cell growth and characterization, analyzed the data, and manuscript writing and editing

Co-Author: Matthew W. Fields

Contributions: Obtained grant funding, conceptualization, research supervision, manuscript writing and editing

Co-Author: James N. Wilking

Contributions: Obtained grant funding, conceptualization, research supervisor, data analysis, manuscript writing and editing

Manuscript Information

Title: 3D Printing of Synthetic Biofilms using Photolithography

Authors: Isaak J. Thornton[1,3], Kathryn R. Zimlich[2,3], Matthew W. Fields[2,3,4], and James N. Wilking[5*]

Affiliations: [1]Mechanical & Industrial Engineering, [2]Department of Microbiology & Cell Biology, [3]Center for Biofilm Engineering, [4]Civil Engineering, Montana State University, Bozeman, MT; [5]Department of Physiology and Biomedical Engineering, Mayo Clinic, Rochester, MN

*Corresponding author

Status of Manuscript:
☐ Prepared for submission to a peer-reviewed journal
☒ Officially submitted to a peer-reviewed journal
☐ Accepted by a peer-reviewed journal
☐ Published in a peer-reviewed journal

Date of submission: 9/6/2024

Acknowledgments

This research was conducted under support of the Army Research Office through grant W911NF1910288. Imaging was made possible by The Center for Biofilm Engineering Imaging Facility at Montana State University, which is supported by funding from the National Science Foundation MRI Program (2018562), the M. J. Murdock Charitable Trust (202016116), the US Department of Defense (77369LSRIP & W911NF1910288), and by the Montana Nanotechnology Facility (an NNCI member supported by NSF Grant ECCS-2025391). The authors thank Dr. Heidi Smith for invaluable assistance.

Abstract

Biofilms are surface associated microbial communities embedded within self-produced polymeric matrices. These communities are shaped by the interactions of the community members, the matrix, and the environment, resulting in living structures with diverse chemical, physical, and physiological properties that can change over time. The structural heterogeneity that results from these interactions influences many important biofilm properties such as community diversity, metabolic diversity, and stress resistance. Understanding the link between the structural features of biofilms and their functional outcomes is critical to advancing our knowledge of how microorganisms exist and persist in many different environments and conditions, including the harnessing of biofilms in biotechnological applications. This study introduces a novel approach using light-based 3D bioprinting to fabricate synthetic biofilms with control over resultant structural properties. We use confocal microscopy to observe and analyze the development of these synthetic biofilms, revealing insights into the developmental dynamics influenced by the imposed printing parameters. The findings demonstrate the potential for integrating advanced biofabrication techniques and detailed imaging to manipulate and observe biofilm structures. Based on these findings, we propose a framework for designing biofilms with directed structural features.

Introduction

Most microorganisms have been naturally selected for growth in multicellular communities known as biofilms[1]. These communities are implicated in a host of medical[139–141] and industrial[142] challenges, but also play critical roles in global nutrient cycling[143] and waste remediation[144]. Biofilms typically form on surfaces and consist of cells embedded in a polymeric, self-produced extracellular matrix. Within these films, flow is suppressed, and diffusion is the primary means of transport[145]. Consequently, nutrient consumption and waste production leads to the development of chemical gradients, which, in turn, generate heterogeneity in physiological processes like metabolic activity, gene expression, protein production[2,24,25,146]. These heterogeneities contribute to the physiological complexity of biofilms and influence important functions such as stress resistance[25,147] and resource processing[76].

Biofilm structure plays a critical role in the development of gradients and heterogeneity. For example, film thickness and cell density impact local nutrient concentrations and metabolic activity[44,76,145,148]. Conversely, biological processes such as cell growth and matrix production affect biofilm structure[22,47,149]. Understanding the interactions between structure and function could be pivotal in advancing research across biofilm control, bioremediation, and microbial ecology[1,22,76,139,150]. However, elucidating these relationships is challenging because self-assembled biofilms, whether naturally formed or cultivated *in vitro*, often develop complex, heterogenous structures through a series of intricate processes[23,30,32,149,151]. Therefore, there is a need for the development of experimental methods that can effectively control and observe the relationships between biofilm structure and function.

3D bioprinting can provide exquisite control over the structure of living materials at the centimeter-to-micrometer scale[54,152,153]. While microbial bioprinting has not yet been explored to the same extent as the printing of eukaryotic cells and tissues, 3D printed microbial structures have been studied within several diverse applications including living material synthesis[74,154–156], electrosynthesis[157], biosensors[68], synthetic soil aggregate models[158], and antimicrobial resistance models[77]. However, little effort has been made to characterize the structural heterogeneity that develops after printing. Such knowledge is critical for developing a fundamental understanding of structure-function relationships in microbial biofilms and advancing 3D printing applications. Models exist for biofilms based upon multidimensional biomass retention, but spatial heterogeneity and boundary layers can be difficult to capture and/or create computationally intensive models[159]. Therefore, better control of biofilm structure through engineering principles (design-build-test-learn) could enable improved understanding and insight into the complex relationships between diffusion and kinetic effects.

Here, we use light-based bioprinting to create single-layer hydrogel films containing homogeneously dispersed bacteria (*Pseudomonas fluorescens*) and use fluorescence microscopy to characterize the primary structural features of these films. We systematically vary the initial concentration of bacteria over five different concentrations, spanning approximately three orders of magnitude, and follow cellular growth and aggregate development over six days. We make the following observations: (i) dispersed cells grow to form discrete colonies, (ii) colony number at long times is directly proportional to the initial concentration, (iii) average colony volume is inversely proportional to the initial concentration, (iv) all conditions approach the same biovolume independent of initial cell concentration, and (v) the characteristic length scale of the primary structural gradient is related to the initial cell concentration through a logarithmic function. We anticipate these relationships between initial cell concentration and structure could be used to engineer microbial communities with well-defined structures, providing a valuable tool to deepen our understanding of structure-function relationships in microbial biofilms.

Materials and Methods

Preparation of Recombinant Cells and Growth Media.

The *Pseudomonas fluorescens* N2E2 strain harboring the RFP-expressing pGinger suite plasmid was obtained from Dr. A. Deutschbauer (Lawrence Berkeley National Laboratory). The pGinger plasmid in N2E2 was developed under kanamycin selection and constitutive expression via conjugation from *Escherichia coli* WM3064TSB as previously described [160]. Tryptic soy broth (TSB) media was prepared by dissolving 15 g of TSB powder (MP Biomedicals LLC) in 500 mL Milli-Q® water and autoclaving for 20 minutes at 121 °C. TSB media was supplemented with 7.5 g agar to prepare tryptic soy agar (TSA) plates at 1.5% w/v agar concentration. Before pouring plates, kanamycin sulfate (Sigma-Aldrich) was added to a final concentration of 50 μg/mL to prepare antibiotic selection plates for growth of recombinant N2E2. The kanamycin stock solution was prepared at 50 mg/mL by dissolving in Milli-Q® water and filter-sterilizing through a 0.2 μm polycarbonate filter. Kanamycin stock was stored in Falcon tubes at 4 °C as per manufacturer's recommendation.

Preparation of Growth Media

All 3D printing growth experiments were conducted with a defined groundwater media recipe (UGA) as previously described, excluding supplemental metals and antibiotics (Supplemental Tables 4.1-4.5)[161]. UGA was first prepared anaerobically by mixing the UGA salt stock solution, mineral stock solution, sodium bicarbonate, and Milli-Q® water and adjusting pH to 7.2 with 2N HCl in a 1L round bottom flask. The vitamin stock solution was added to a final dilution of 1X along with 1M monobasic sodium phosphate stock. The solution was sparged with an 80% N_2 / 20% CO_2 gas mixture while stirring for 90 minutes, then filter-sterilized into anaerobic serum bottles with 80% N_2 / 20% CO_2 headspace through a 0.2 μm polycarbonate filter. For 3D printing experiments, 45mL of anaerobic media was transferred into a sterile 50 mL Falcon tube under aerobic conditions. Sodium acetate and sodium nitrate were added to a final concentration of 20mM and 0.1mM, respectively. Sodium acetate, sodium nitrate, and monobasic sodium phosphate (Sigma-Aldrich) stock solutions were prepared at 1 M by dissolving into Milli-Q® water and filter sterilizing through a 0.2 μm polycarbonate filter. Stock solutions were stored at 4 °C.

Growth of Inoculum for 3D Printing Experiments.

Cells were stored in 2 mL cryogenic vials (Corning) at -80 °C in 1 mL of 20% v/v glycerol, prepared by mixing 500 μL cell culture grown in TSB at an OD_{600} of 0.8 with 500 μL 40% v/v sterile glycerol. Streak plates were prepared from N2E2 glycerol stocks by streaking cells onto TSA plates under 50 μg/mL kanamycin selection using a sterile inoculating loop and incubating in the dark at 30°C for 36 hours. To prepare cells for 3D printing experiments, a single N2E2 colony from a TSB agar plate was inoculated into 50 mL of TSB media containing 50 μg/mL kanamycin in a 250 mL Pyrex® culture flask. Flasks were incubated at 30 °C, 130 RPM, until an OD_{600} of 0.7 was reached (corresponding to approximately $3x10^8$ CFU/mL). Where applicable, ten- and hundred-fold population dilutions were prepared by a two-step serial dilution of cells into sterile TSB media. Ten-fold and approximate hundred-fold population concentrations were prepared by transferring 50 mL of N2E2 culture at an OD_{600} of 0.7 into a sterile Falcon tube and centrifuging at 10,000 g for 20 minutes at room temperature. Supernatant was poured off and the cell pellet resuspended in 5 mL fresh TSB media for ten-fold concentration, and 0.5 mL fresh TSB media for the highest concentration. Cells were stored in Falcon tubes at room temperature prior to printing for no more than one hour.

Preparation of Photoactive Resin.

The non-cytotoxic photoactive resin was prepared before each experiment. The photoinitiator, lithium phenyl-2,4,6-trimethyl-benzoylphosphinate (LAP) (Sigma Aldrich), was dissolved in PBS at 60°C to a final concentration of 0.1% (w/v). Poly(ethylene glycol) diacrylate (PEG-DA) oligomers (Sigma Aldrich PEG-DA Mn 700) were added at a 10% (v/v) final concentration. A yellow azo dye, tartrazine (Alfa Aesar) acted as a photoblocker and was incorporated at concentrations between 0.01% and 0.05% (w/v). Photoabsorber concentration and light exposures were tuned based on desired cure depth as described previously[91]. The final solution was filter sterilized and stored away from light before printing. Just before printing, bacteria were concentrated to 10X the desired final cell concentration in culture medium. The printing resin was then inoculated with the bacterial solution at a 10% (v/v) final PEG-DA concentration before the solution was vortexed and protected from ambient light immediately pre-printing.

Printing Hydrogels Containing Bacteria.

Print geometries were designed with computer-aided design (CAD) software (Autodesk, Fusion 360), exported as standard triangle language (STL) files, and uploaded to the OpenFL slicing program (FormLabs). Custom laser profiles with control over laser power, speed, and number of passes were created to achieve the desired cure depth, as described previously[91]. Liquid resin was added to a depth of approximately 4 mm to individual wells of a glass bottom well plate (Cellvis 6-well, P06-1.5H-N), and the plate was mounted in the SLA printer (Form 1+, FormLabs) using a custom-built insert. We note local increases in cell density near the cover glass-gel interface, likely due to cell settling during the printing process (Figure S2). We find that manually agitating the resin with cells before loading the well plate and similar manual agitation of the well plate before printing minimizes this effect. To reduce bacteria residence time in resin before printing and minimize cell sedimentation, care was taken to print quickly (<5 min.) following the addition of bacteria to the resin. Following printing, the well plate was immediately removed from the printer and any non-polymerized resin was extracted from each well. The gels were then rinsed three times in sterile PBS, followed by a one-time rinse in ethanol (70% v/v) for ~10 s. Gels were again rinsed three times in sterile PBS before filling the wells with culture media. The ethanol rinse serves to kill bacteria that are not encapsulated in the gel to prevent overgrowth. In 10 s, ethanol will only diffuse ~100-200 μm into the gel[45,145]; thus, killing cells on the gel surface, but not deep in the gel.

Hydrogel Incubation and Media Replacement.

Following the rinse sequence, 5 mL of UGA culturing medium was added to each well, fully submerging the gels. The plates were then incubated at 30°C. Culture media was replaced every 24 h for up to 6 days. For each exchange, old media was extracted, the gel was rinsed in PBS, and 5 mL of fresh UGA media added. Following each exchange, the plates were immediately returned to 30°C incubation.

Confocal Imaging of Printed Hydrogels.

Fluorescence time-lapse confocal microscopy (inverted Stellaris 8, Leica Microsystems) was used to observe the relative activity and growth of the printed biofilms. The use of glass bottom well plates enables non-destructive observation of the printed structures. Recombinant *P. fluorescens* was observed using the mCherry Leica preset (excitation: 587 nm; emission: 610 nm). A 10x dry objective enabled full thickness imaging of the biofilm structures. Laser power was set to roughly half of the dynamic range at the beginning of each experiment to allow for cell growth and increased fluorescence intensity over the course of the experiment. Single fields of view were taken in each well at every time point. The entire thickness of each gel was captured using an image z-stack optimized to each field of view. A z-step size of approximately two microns produced stacks of 60-200 images dependent on film thickness. Imaging was done near the xy center of each gel to avoid imaging the non-uniform geometry caused by light attenuation at the edge of the printed structures (as portrayed in Figure 4.1). For time lapse imaging, image stacks were taken every two hours. Image sets were taken at multiple timepoints to quantify growth spatially within the synthetic biofilms and between conditions and across time. High resolution images were taken near the bottom of the biofilms using a 63x oil immersion objective (Figure 4.6).

Biomass Quantification.

We use image analysis software (Imaris v9.9, Oxford Instruments) to process and analyze image data. A Gaussian blur was used to preprocess images to reduce noise for thresholding. We then use the surface tool to automatically threshold the images and produce 3D reconstructions of the bacterial colonies (*e.g.*, top row of Figure 4.2). Automated thresholding selects appropriate values for each condition and time point, with seed splitting applied to high density prints to enhance segmentation accuracy. Tabulated data detailing colony location and size at each timepoint is exported from Imaris. We use custom MATLAB scripts for data quantification and visualization. To assess variability and calculate averages, each field of view is divided into nine equal sections. For quantification of Z dependent parameters, each section is further divided along the z-axis into bins based on the number of colonies within each section.

Quantification of Biovolume Gradient.

To quantify the biovolume gradients in mature synthetic biofilms, we analyze image data at the final timepoint to assess biovolume distributions. We fit an exponential decay function to model the reduction of RFP expressing biovolume along the z-axis as described by Equation 4.1:

$$V(z) = V_0 * e^{-z/\lambda} \quad \text{(Eq. 4.1)}$$

Here, $V(Z)$ represents the biovolume at depth z, V_0 is the biovolume at the base, and λ is the decay length scale. To determine a characteristic λ for each condition, we fit equation 1 to the volume distribution between the bottom of the biofilm and the biovolume peak. We average the coefficients of each fit to determine a mean λ and V_0 value for each fitted condition. We plot the mean and standard deviation of both λ and log(ϕ_0) before fitting a linear regression to the means (*e.g.*, Figure 4.5D).

Assessing Impact of Resin and Print Process on Cell Viability.

Hydrogels were prepared with identical printer settings and resin preparation as described above. A wild-type culture of N2E2 was grown in TSB to an OD_{600} of 0.7 also as described above, but omitting the kanamycin, as the wild-type carries no plasmid expressing mCherry or kanamycin resistance. The live/dead stain was applied 2, 22, and 48 h after standard printing and rinse procedures, then immediately imaged after each application. Three fields of view were imaged for each hydrogel at each time point with a 20X magnification dry objective. As this is an endpoint analysis, different hydrogels were stained and imaged for each time point. The dead cell fraction was determined by the proportion of cells in each field of view that stain with both live (Cyto) and dead (propidium iodide) stains. A spot filter was applied in Imaris for each fluorescent stain channel and automatic thresholding filters were applied then inspected for accuracy. A killed control was included for the purpose of evaluating the efficacy of the live/dead stain. For the killed control, a hydrogel was immersed in 70% ethanol for 30 minutes before staining, then imaged 2 hours post-printing with the same methodology.

Results & Discussion

To fabricate synthetic biofilm, we use a commercially available inverted light-based 3D printer (FormLabs Form 1+) to selectively photopolymerize a single layer of hydrogel directly onto the surface of a glass bottom multi-well plate (Figure 4.1). We use a well-characterized, non-cytotoxic liquid resin based on polyethylene glycol diacrylate (PEG-DA), which rapidly solidifies when exposed to violet light[64,91]. To demonstrate the bioprinting process, we select the facultatively anaerobic denitrifying bacterial strain *Pseudomonas fluorescens* N2E2, which has been modified to constitutively express red fluorescent protein (RFP) [160]. The organism is added to the liquid resin at well-defined concentrations before printing.

The thickness, h, of the printed film is set to approximately 150 μm by tuning light exposure and photoabsorber concentration[91]. This thickness is relevant for observing physiological heterogeneity in *Pseudomonas* biofilms[162,163]. We print the synthetic biofilms in single uniform layers, avoiding material heterogeneities associated with printing multiple layers or multiple extrusion paths. Additionally, printing directly into a glass bottom well plate addresses common vat polymerization issues by avoiding peel forces and printhead/vat misalignment[84,164]. The use of standardized well plates provides an accessible and sterile printing platform that readily integrates with established microbiology tools, such as inverted confocal microscopy. Moreover, the printed gels remain adhered to the bottom of the wells, facilitating time-lapse microscopy of the synthetic biofilms.

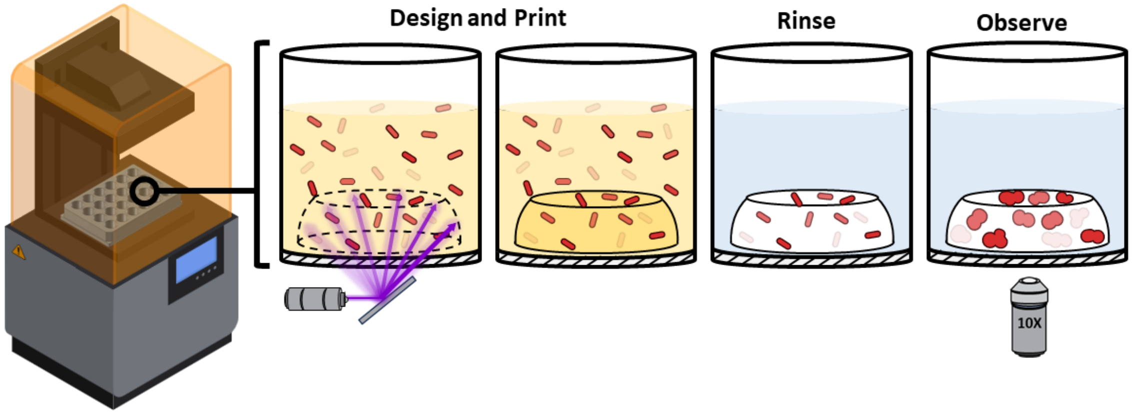

Figure 4.1. Overview of synthetic biofilm printing approach. Design & Print: Bacteria are suspended in a photopolymerizable liquid resin. Exposure to violet light (405 nm) induces solidification of liquid into hydrogel. Cells in the print region become trapped in the hydrogel matrix. Rinse: Excess resin and cells are removed and exchanged with growth media. Observe: Structure and dynamics of microbial colonies are observed with confocal fluorescence microscopy.

Fluorescence confocal microscopy reveals that individual bacteria are distributed homogeneously throughout the gel (Figures 4.6 & 4.7). The mesh size of the printed hydrogel is on the order of tens of nanometers, significantly smaller than bacteria, which have dimensions on the order of micrometers[45,165]; thus, we observe that individual cells replicate but are constrained by the gel and grow to form discrete colonies or aggregates containing densely packed cells (Figure 4.6). Previous studies suggest that bacterial growth within polymer matrices is influenced by factors such as confinement and matrix stiffness, which can affect both the behavior of the embedded cells and the morphological characteristics of the resulting microcolonies[47,49,166,167].

Building on these findings, we use confocal microscopy to quantify the size, number, and three-dimensional position of these colonies over time. This approach allows us to monitor the growth and emergence of structural heterogeneity within the biofilm.

To explore the growth of bacteria within the hydrogel and the influence of initial conditions on population structure and dynamics, we print hydrogels containing different cell concentrations and perform confocal timelapse imaging over six days. For clarity, we refer to the conditions by their starting cell volume fraction, ϕ_0 as determined by image analysis. We print gels containing five different $\phi_0 = 0.0003, 0.002, 0.035, 0.055, 0.119$, spanning nearly three orders of magnitude. While consistent light exposure conditions are used for all prints, we observe an increase in cure depth at high cell densities, suggesting that scattering can impact the print process. As a result, the film thicknesses, h, varied between 100 μm and 250 μm (Figure 4.7, Supplemental Text 2). For each print, we collect 3D image volumes every two hours for the first 20 h, and once a day for the following five days.

We first look at the structures formed by well-developed systems after six days of growth. We find that systems inoculated with different ϕ_0 form dramatically different structures, as shown by the 3D microscopy image volumes (Figure 4.2). Systems printed with low ϕ_0 grow to form a small number of large colonies homogenously distributed throughout the entire gel, whereas systems printed with high ϕ_0 form numerous small colonies concentrated in a narrow region near the surface of the gel. For all but the lowest ϕ_0, there is a clear decrease in colony size and colony number moving into the gel, away from the resource-rich interface. These gradients are well-known structural hallmarks of reaction diffusion systems.

To better compare these gradients and adjust for differences in h, we define the well plate glass surface as the zero point, normalize each gel by its thickness, and plot the *xz* max projection of biovolume data for each condition in the bottom row (Figure 4.2). At the lowest ϕ_0 the biovolume is uniformly distributed in z, indicating that growth is not limited by substrate diffusion through the gel. In contrast, at the highest ϕ_0 the biovolume is heterogeneously distributed in z, indicating diffusion limited growth, presumably a result of microbial consumption surpassing substrate transport by diffusion.

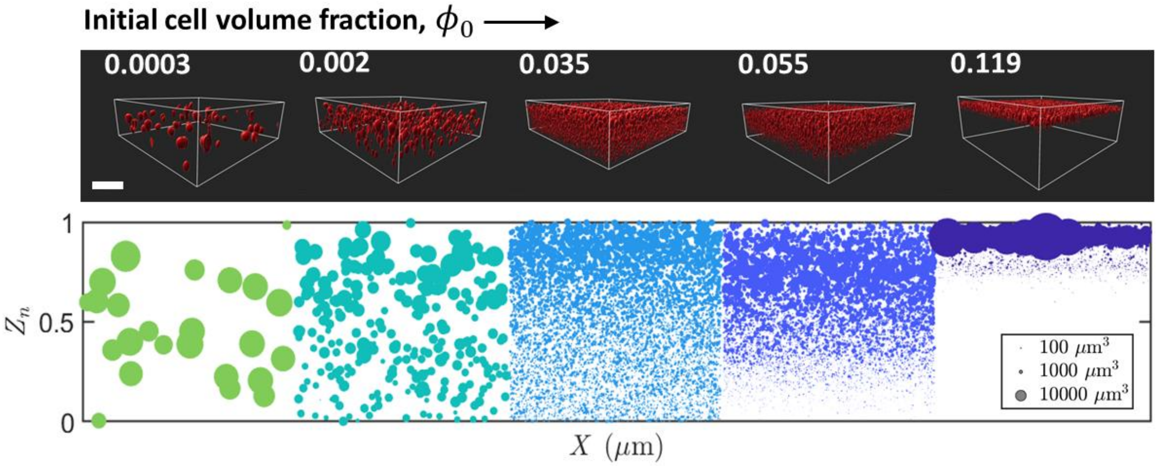

Figure 4.2. Different cell concentrations result in different community structures. (Top row) Three-dimensional renders based on confocal microscopy images of Pseudomonas fluorescens-containing films printed with varying ϕ_0 over nearly three orders of magnitude reveal dramatically different structures. Biofilms imaged after six days of growth. Scale bar is 200 µm. (Bottom row) Corresponding two-dimensional xz maximum projection plots of the imaged volumes. Here, Zn is the z position normalized by the thickness of the gel. Each xz projection represents a 400 µm wide section. Circle size corresponds to colony volume, V, as depicted in the legend.

To better understand these structures, for each ϕ_0 we determine the number of individual colonies, n in each imaged volume as a function of time. We find that for all other cell concentrations, n decreases with time before reaching a steady state, n_s after ~48 hours (Figure

3A, log-linear plot). Distinguishing individual colonies at long times for the highest ϕ_0 is challenging due to their proximity (see S1 Text); so, we include these data but interpret them with caution as they likely underestimate n. Normalizing $n(t)$ by n_0 (n at $t = 0$), we find that for all but the highest initial cell concentration, $n(t)/n_0$ decreases to approximately $n_s/n_0 \approx 0.44 \pm 0.09$ (Figure 4.3B, linear-linear plot). Remarkably, the total number of colonies at long times is related to the initial cell concentration through a simple proportionality constant ($n_e \approx 0.44n_0$). This result, observable across more than two and a half orders of magnitude in cell concentrations, suggests a mechanism that is intrinsic to the cell population. Similar observations have been made with both environmental samples as well as bacterial cultures. For example, a significant percentage (20-80%) of bacteria recovered from a variety of natural environments were shown to be metabolically inactive[168], and for lab-cultured *Vibrio parahaemolyticus*, approximately half the bacterial population was reported to be metabolically inactive[169]. It is likely that various factors, including metabolic heterogeneities, light exposure, and free radicals contribute to this result[108]. Further work will be needed to delineate these possible effects, but 3D bioprinting could be a useful tool to enable visualization of cell-to-cell variability in bacterial populations, including biofilms.

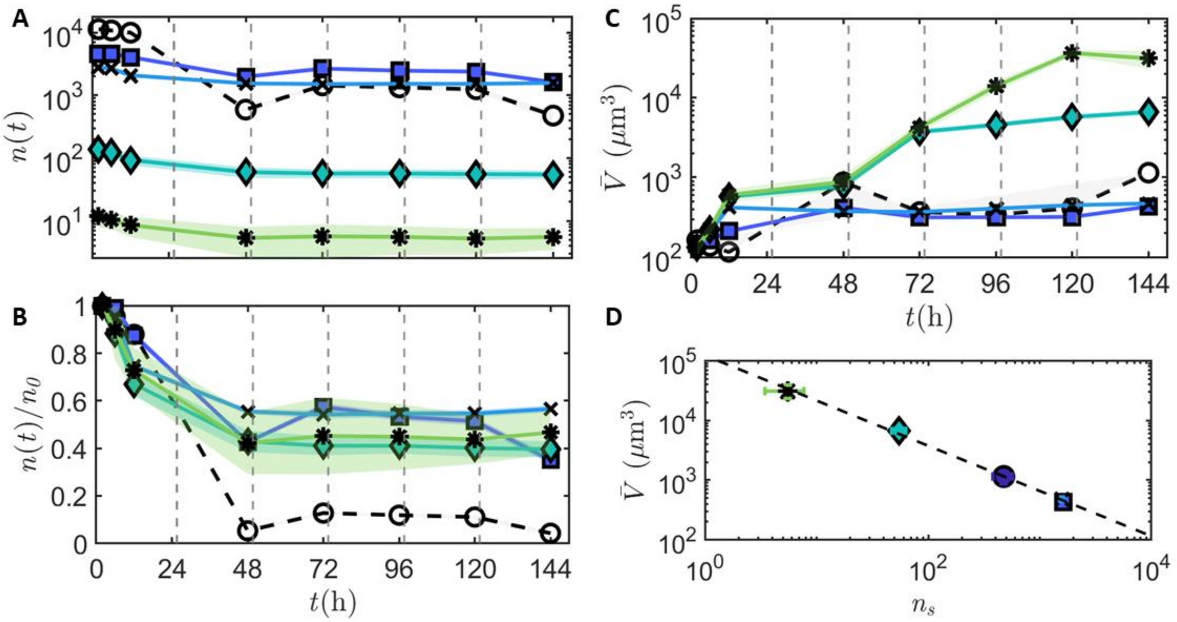

Figure 4.3. Time-dependent analysis of colony number and volume. (A) Total colony number within image volume, $n(t)$, plotted as a function of time for the five conditions shown in Figure 2 (ϕ_0 = 0.0002 (*), 0.002 (♦), 0.033 (**x**), 0.060 (■), and 0.118 (○)). The shaded area around each line represents standard deviation and vertical dashed lines indicate media exchange. (B) Normalized colony number $n(t)/n_0$ from (A) plotted as a function of time. For all but the highest ϕ_0, at long times $n(t)/n_0$ approaches ≈ 0.44 ± 0.09. (C) Mean colony biovolume, $\overline{V}$, plotted as a function of time. (D) Mean colony biovolume at long times, $\overline{V}_s$ plotted as a function of colony number at long times, n_s is fit well by a power law with exponent, a = -0.78 (R2 = 0.99).

We next determine the individual volume, V of all the imaged colonies in each condition and plot the average colony volume, $\bar{V}$ as a function of time (Figure 4.3C). For the higher cell ϕ_0 conditions (0.035 and 0.055; excluding 0.119) we find that $\bar{V}$ increases by less than an order of magnitude and plateaus after 48 h; while at lower ϕ_0 the colonies continue to grow, and plateau at longer times. This volume difference is consistent with a reaction-diffusion system, where colonies far from one another have more available nutrients to utilize for metabolism and growth than colonies near one another.

In an ideal system, where all available nutrient is converted into biomass and V does not impact growth, the average volume at long times, $\bar{V}_s$, should be inversely proportional to n_s ($\bar{V}_s \propto {n_s}^{-1}$). Plotting $\bar{V}_s$ at long times (t = 144 h) as a function of n_s, we find that $\bar{V}_s \propto {n_s}^{-0.78}$ (Figure 4.3D). This indicates that colonies at low ϕ_0 have grown less than expected or colonies at high ϕ_0 have grown more than expected. This could be due to a variety of factors. For example, differences in colony density and size likely lead to different cell phenotype distributions and thus differences in resource utilization (*e.g.*, anabolic metabolism vs. matrix production). Additionally, as colonies become larger, the colony surface to volume ratio, S/V decreases, possibly influencing resource and waste transport into and out of the colonies, respectively. Finally, the physical properties of the hydrogel (*e.g.*, elasticity, diffusivity, osmotic compressibility) could impose constraints on colony expansion, with larger colonies experiencing greater compressive stresses than smaller colonies[45,49,79].

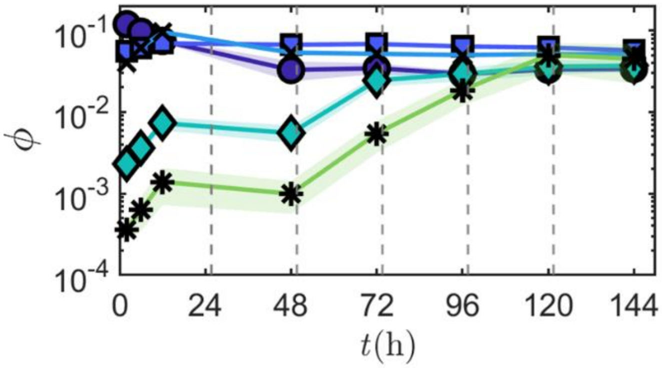

Figure 4.4. Time-dependent analysis of total biovolume fraction. Biovolume fraction, $\phi(t)$ plotted as a function of time for the five conditions shown in Figure 2 (ϕ_0 = 0.0002 (*), 0.002 (♦), 0.033 (x), 0.060 (■), and 0.118 (○)). At long times, ϕ for all conditions approaches ≈ 0.040 ± 0.021.

In microbial ecology, the carrying capacity, K is the maximum population size for a given organism that a system can sustain[170]. In the context of 3D printed microbial systems, it is important to understand how K varies with ϕ_0 because this parameter is related to total system function and output. Here, it is difficult to resolve individual microorganisms; so, we assume that the dimensionless biovolume fraction ϕ, is proportional to population size and plot ϕ for the five different conditions shown in Figure 4.2. We find that $\phi(t)$ for high ϕ_0 remains relatively flat (0.035 and 0.055) and even decreases slightly (0.119). At the highest ϕ_0, this decrease occurs as many small, high-density colonies grow near the film surface but cells deep in the gel become inactive, likely due to resource depletion (Figure 4.4). For the two lowest ϕ_0 conditions, we observe that ϕ increases over time for the first 120 h, growing large individual colonies more uniformly across the film depth (Figure 4.4). For these conditions, there is a slight decrease between 24-48 h, which is likely due to the decrease in n shown (Figure 4.2A, B) which likely results from the reduction in RFP-active colonies within the first 48 hours as the reduction in colony number momentarily surpasses the increase in average colony volume. Remarkably at long times, all conditions converge to a similar $\phi \approx 0.04 \pm 0.02$, suggesting that the system reaches an equilibrium K (in terms of total biovolume) independent of initial conditions.

The structural parameters discussed this far (n, $\bar{V}$, and ϕ) are bulk parameters and do not capture the spatial gradients apparent in Figure 4.2. To investigate these gradients, we plot the distribution of biovolume, $V(z)$ as a function of z for each condition and at specific times in Figure 4.5. At short times, immediately following printing, bacteria are uniformly distributed and $V(z)$ for all conditions is nearly independent of z (Figure 4.5A), except for possible boundary effects (see Methods). At long times, $V(z)$ for the three highest ϕ_0 becomes highly dependent on z, exhibiting a sharp decrease with increasing depth (Figure 4.5B). The development of this gradient as function of time is shown for $\phi0 = 0.035$ in Figure 4.5C. The gradient is established as colonies near the upper surface of the gel (high z) grow more than colonies and cells near the bottom (low z), and even become inactive. Interestingly, at long times, $V(z)$ for the two lowest ϕ0 do not develop significant spatial gradients (Figure 4.5B).

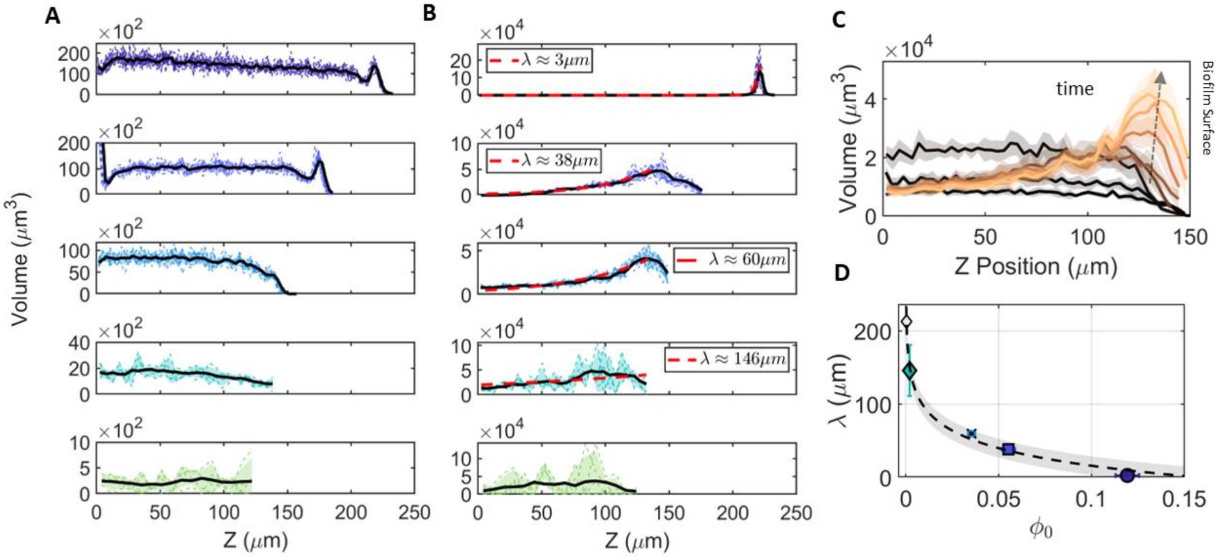

Figure 4.5. Gradient development in synthetic biofilms. Biovolume distributions plotted as a function of z for synthetic biofilms with different ϕ_0 at (A) t = 0 h and (B) t = 144 h. Each plot contains biovolume subvolumes (dashed lines), mean (black line), and standard deviation (shaded region). At early times (A), bacteria are homogenously distributed throughout the film. At long times (B) for the highest ϕ_0 sharp gradients have developed, while for the lowest ϕ_0 the distributions appear homogenous. Fits to an exponential decay function (red dashed line) and resulting characteristic length scale, λ, for the four highest ϕ_0 are shown in (B). Blue dashed line shows distribution as predicted in subpanel D. (C) Volume distributions for ϕ_0 = 0.035 at different times shows development of gradient. (D) Relationship between λ and $\log(\phi_0)$ for the four highest ϕ_0 (0.002 (♦), 0.033 (**x**), 0.060 (■), and 0.118 (○)) fit with an exponential function ($\lambda(\phi_0) = -80\log(\phi_0) - 64$, R2 = 0.93) as shown by the black dashed line and shaded 95% confidence interval. Markers represent mean λ and ϕ_0 with error bars representing the respective standard deviations. The open diamond denotes a value of λ = 213 µm for ϕ_0= 0.0002 as predicted by the linear regression.

To quantify these gradients, we fit the long-time distributions of the four highest ϕ_0 in Figure 4.5B to an exponential decay (red dashed lines). We exclude the lowest ϕ_0 (Figure 4.5B, lowest plot) due to insufficient data for fitting. The characteristic length scale, λ, associated with each fit provides a measure of the rate at which the biovolume decreases with depth into the gel. Across the observed conditions, λ increases with decreasing ϕ_0, from 3 μm (ϕ_0 = 0.119) to 146 μm (ϕ_0 = 0.002). For an exponentially decaying function, V is reduced by a factor of $1/e$ = 0.368 every distance λ. So, at the highest ϕ_0, the volume decreases to approximately 5% of the maximum value within ~3 λ (~9 μm), suggesting that a majority of the biovolume is near the top of the gel, as observed in Figure 4.2 and Figure 4.5B. In contrast, for ϕ_0 = 0.033, where λ = 146 μm, a similar volume reduction spans 438 μm, significantly larger than the thickness of the gel, and the distribution appears much more homogenous (Figure 4.2 and Figure 4.5B). To determine the dependance of λ on ϕ_0, we plot λ as a function of ϕ_0 and find that the data is well fit to a logarithmic function (Figure 4.5D). Based on this fit, ϕ_0 = 0.0002 is expected to have $\lambda \approx 213$ μm. While the theoretical basis for this dependence needs future work, the developed methods for synthetic biofilm allow empirical estimations of gradient scales for a given microorganism that could offer predictive power for engineered-living materials.

The results presented here provide a framework for creating synthetic biofilms with well-defined structures and could be used to better understand structure-function relationships in microbial biofilm communities. The steady state colony number, n_s, colony size, $\bar{V}_s$, and characteristic length scale λ are all dependent on the initial starting cell number, n_0; thus, these parameters can be set by controlling n_0, and, because ϕ_s is independent of n_0, the relationship between structure and function (*e.g.*, resource utilization and allocation, *etc.*) could be systematically explored while keeping ϕ_s fixed [27]. It is likely that the different structures shown in Figure 4.2 exhibit significantly different chemical and physiological heterogeneities, resulting in differing functions. In future studies, it would be interesting to explore ways to control n, $\bar{V}$, and λ independently of one another. For example, in the limit of thin, low ϕ_0 biofilms where $\lambda >> h$, the functions $n_e \approx 0.44n_0$ and $\bar{V}_s \propto {n_s}^{-0.78}$ may change. Because the films created here are flat, uniform, and initially homogenous, they can be modeled more easily than self-assembled biofilms with more complex structures. Utilization of the growing library of fluorescent reporters to observe processes like gene expression[27], metabolism[171], and substrate consumption[124], in combination with advanced imaging and modeling techniques, will enable investigations of specific biofilm structure-function relationships[27,44,145]. This integrated engineering approach opens new possibilities for both innovation in biofilm research and technology as well as improved understanding of underlying biofilm fundamentals.

Conclusion

In this study, we introduce a method of light-based 3D printing to create synthetic biofilms with engineered structures. By embedding *Pseudomonas fluorescens* bacteria within a PEG-DA hydrogel matrix, we actively control the biofilm environment, enabling precise manipulation of the initial cell density and biofilm thickness. This controlled approach reveals how varying initial cell densities significantly impacts the resultant biofilm structure, with higher densities leading to numerous small colonies near the gel surface, and lower densities resulting in fewer but larger colonies evenly distributed throughout the gel. Through quantitative confocal microscopy, we observe that these structural dynamics evolve over time with micrometer resolution. We observe synthetic systems develop heterogeneities in growth and active biovolume similar to those observed in natural biofilms. We further quantify the resultant structures of active biovolume with respect to imposed printing parameters, establishing a framework for engineering synthetic biofilms with specified structural characteristics that could possibly match different stages of a natural biofilm life cycle.

The methodological advancements introduced here enhance our understanding of synthetic biofilm dynamics and present new opportunities for microbial biofabrication and biofilm research. Detailed observation and quantification provide a foundational framework for engineering biofilms with directed characteristics. This technique addresses some of the limitations associated with self-assembled biofilm models and offers a valuable tool for advancing our ability to manipulate, observe, and understand the structural dynamics and functional outcomes of both natural and fabricated biofilms.

Supplemental Information

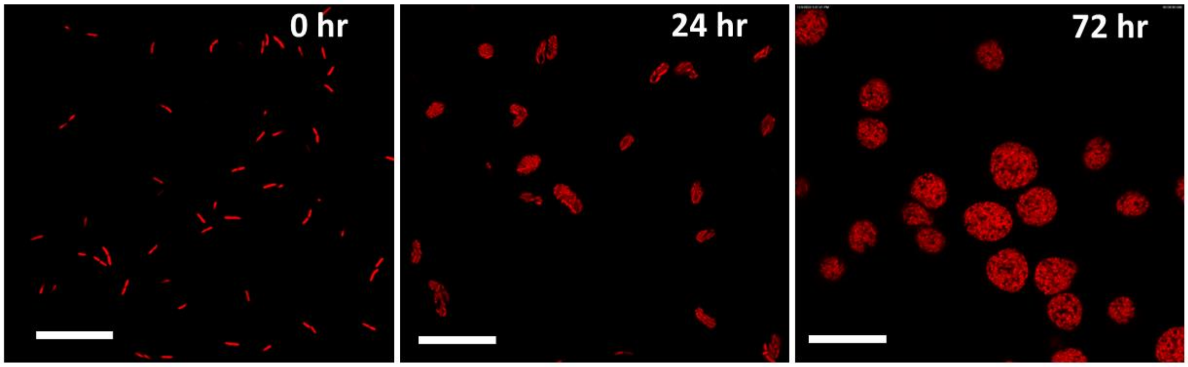

Figure 4.6. Growth of discrete colonies following bacterial inoculation in printed hydrogels. High resolution confocal microscopy images (Leica Stellaris 8, 63× oil immersion objective) show representative growth of encapsulated bacterium *Pseudomonas fluorescens* over 72 hours. Colonies start as individual cells or small groups of cells and grow into densely packed discrete colonies. Initial volume fraction shown is approximately 0.035. Scale bars represent 20 µm.

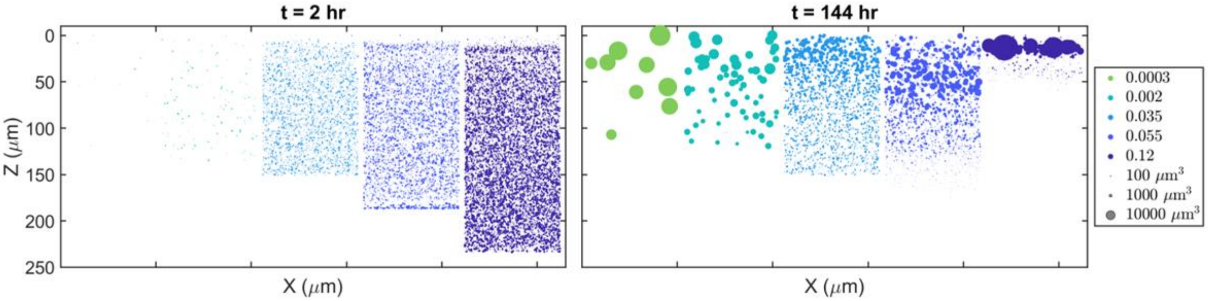

Figure 4.7. Colony distributions at early and long times. Image analysis data showing colony location and size as XZ max projection. (A) Max projection at 2 hours following printing. Cell distribution is nearly homogenous. We observe slight increases in cell density at the bottom of high density prints and attribute this to settling of cells and cell aggregates during the printing process. (B) Colony distribution following 6 days of culture. Heterogenous distributions of colonies emerge in mature biofilms. Large colonies depicted in higher density biofilms can include multiple discrete colonies counted together as one larger colony (Supplemental Text 1).

Component	**Amount**	**Units**
NTA Disodium Salt	1.5	g/L
MgSO4*7 H$_2$0	3	g/L
MnSO4* H$_2$0	500	mg/L
NaCl	1000	mg/L
FeSO4*7 H$_2$0	100	mg/L
CaCl2*2 H$_2$0	100	mg/L
CoCl2*6 H$_2$0	100	mg/L
ZnCl	130	mg/L
CuSO4*5 H$_2$0	10	mg/L
AlK(SO4)2*12 H$_2$0	10	mg/L
Boric Acid	10	mg/L
Na2MoO4*2 H$_2$0	25	mg/L
NiCl2*6 H$_2$0	24	mg/L
NaWO4*2 H$_2$0	25	mg/L
Na2SeO4	20	mg/L

Table 4.1. Minerals stock solution recipe for defined groundwater media recipe (UGA)

Component	Amount	Units
Ammonium Chloride	5	g/L
Potassium Chloride	2.5	g/L
MgSO4*7 H_20	12.32	g/L
CaCl2*2 H_20	367	mg/L
NaCl	250	mg/L

Table 4.2. Salts stock solution recipe for UGA

Component	Amount (mg/L)
d-Biotin	2
Folic Acid	2
Pyridoxine HCl	10
Riboflavin	5
Thiamin	5
Nicotinic Acid	5
Pantothenic Acid	5
Vitamin B12	0.1
p-Aminobenzoic Acid	5
D,L-6,8-Thioctic Acid	5

Table 4.3. Vitamins stock solution recipe for UGA

Component	Amount
dd H_20	467 mL
Salts Stock Solution	20 mL
Vitamins Stock Solution	5 mL
Minerals Stock Solution	5 mL
NaH_2PO_4 (1M stock)	2.5 mL
$NaHCO_3$	1.25 g

Table 4.4. Defined groundwater media recipe (UGA)

Components	Volumes	Stock Concentration
$C_2H_3NaO_2$	900 mL	1 M
$NaNO_3$	4.5 mL	1 M

Table 4.5. UGA recipe post-filter sterilization additions for 45 mL aliquots.

Supplemental Text 1 – Limitations of individual colony resolution

Several limitations may impact the accuracy of colony quantification in synthetic biofilm systems when using fluorescence microscopy. Microscope resolution and light attenuation can significantly affect image quality, particularly in dense biofilm regions. High-density biofilms are known to cast shadows and scatter light in accordance with Beer's Law, complicating the ability to observe fluorescent biovolume within high density structures and limiting the ability to resolve individual colonies[128,129]. Despite these challenges, we find that measuring the total biovolume remains a reliable indicator of biomass accumulation within these systems. This metric is less susceptible to the difficulties of resolving individual colonies, providing a more consistent measure across different experimental conditions.

Supplemental Text 2 – Effects of cell density on photopolymerization cure depth

For this study we hold all printing parameters constant across the different initial conditions to standardize both the cell light exposure and polymerization of the hydrogel. Strikingly, we observe that cure depth of the polymerized structures increases significantly with an increase in cell density (Figure S2). This finding contrasts with previous studies on particle-filled photoactive resin systems where an increase in particle volume fraction corresponds with a decrease in cure depth due to light attenuation associated with absorption and scattering[134,172]. This surprising result suggests that these bacterial cells interact with light differently compared to conventional fillers like ceramic particles. We hypothesize this phenomenon may be a product of multiple scattering and an increase in light path length caused by light interactions with the suspended cells[173–175]. While adjustments to printing parameters, such as photoblocker concentration and light exposure, may be able to account for these changes in cure depth, it is crucial to consider how these adjustments affect the embedded organisms and the properties of the resulting hydrogel. Further research is needed to explore the relationship between photopolymerization and resin microbial density.

Supplemental Text 3 – Viability of 3D printed *P. fluorescens* bacteria

To assess biocompatibility of this resin system with *P. fluorescens*, we 3D printed hydrogels with a wild-type population and performed a live/dead stain. The wild-type was chosen to avoid fluorescent signal crosstalk between the mCherry RFP and the propidium iodide fluorescence signals. In the killed control, 99.24% of the observed cell population encapsulated was stained with propidium iodide two hours after printing. For the experimental treatments, average dead cell fractions of 30.67% were observed after two hours, 37.67% after 22 hours, and 29.33% after 48 hours. Several factors could contribute to this reduction in cell viability. Delayed negative effects of the printer laser on the cell population are possible. For instance, exposure to visible light irradiation in a seawater environment has been shown to produce a viable but non-culturable state in *E. coli* in the presence of a methylene blue[108]. Physiological differences among individuals that are missed when describing the cell population with average values (such as intrinsic growth rate or generation time) may contribute to sensitivity towards laser exposure and/or the unpolymerized resin, though exposure to these conditions is only minutes long.

Under the chosen incubation conditions, the fluorescent stains penetrated approximately 500 μm into the hydrogels. This is likely due to diffusion constraints of the stains into the hydrogel matrix. Thus, the observable cell population was restricted to the outer ~500 µm edge of each hydrogel. While several fields of view could be obtained to calculate an average dead cell fraction, the interior regions of the hydrogels could not be imaged using fluorescence microscopy with this methodology. Although we expect uniform cell distribution throughout the hydrogel, occasional settling at the substrate interface might lead to variations in the dead cell fraction between the internal regions and the periphery of the gel.

Hydrogels were prepared with identical printer settings and resin preparation as described in the Methods. A wild-type culture of N2E2 was grown in TSB to an OD_{600} of 0.7 also as described in the Methods, but omitting the kanamycin, as the wild-type carries no plasmid expressing mCherry or kanamycin resistance. Live and dead stains were applied 2, 22, and 48 h after standard printing and rinse procedures, and each was then immediately imaged. Three fields of view were imaged for each hydrogel at each time point with a 20X magnification dry objective. The dead cell fraction was determined by the proportion of cells in each field of view that stain with both live (Cyto) and dead (propidium iodide) stains. A spot filter was applied in Imaris for each fluorescent stain channel and automatic thresholding filters then inspected for accuracy. A killed control was included for the purpose of evaluating the efficacy of the live/dead stain. For the killed control, a hydrogel was immersed in 70% ethanol for 30 minutes before staining, then imaged 2 hours post-printing with the same methodology.

CHAPTER FIVE

EMERGING INFECTIOUS DISEASES AND INNOVATIONS IN DIAGNOSTIC TOOLS

In chapters 5-8, I discuss research at the intersection of emerging infectious diseases and technologies for pathogen diagnostics. Infectious diseases are significant, and often detrimental, components of global ecosystems, impacting biodiversity, influencing evolutionary processes, and regulating population dynamics across all forms of life[176]. In humans, the shift to agrarian societies brought about an epidemiologic transition where increases in population density enabled the emergence and spread of virulent human pathogens[177]. Throughout history, these diseases have triggered several devastating outbreaks. For instance, infections caused by the bacterium Yersinia pestis (i.e. the plague) resulted in the death of 30-50% of Europe's population during the 14th century with an estimated 200 million casualties[178]. Several epidemics, introduced during European colonization, led to the loss of approximately 95% of Indigenous American populations, with an estimated 20 million deaths[179]. Between 1918-1919, a pandemic of influenza A/H1N1 (i.e. Spanish flu), resulted in approximately 500 million infections and 50 million deaths[178]. As of June 2024, there have been over 700 million confirmed SARS-CoV-2 infections and over seven million deaths reported[178,180].

5.1 Diagnostics in the Context of Emergent Infectious Diseases

The emergence of infectious diseases is an inevitable aspect of our interconnected world[177,181]. To mitigate the human and economic costs of future outbreaks, significant investments in the development of pandemic preparedness is essential. A wide array of tools and technologies are now available to support these efforts. By innovating and strategically investing in pandemic preparedness tools, we enhance our abilities to better manage and potentially contain future pandemics. Conversely, failure to bolster these systems could leave us vulnerable to the uncontrollable spread of infectious diseases, risking widespread mortality and profound societal impacts.

5.1.1 Emerging Infectious Diseases

The World Health Organization (WHO) uses the term “Disease X” to describe a currently unknown pathogen with the potential to cause the next serious pandemic[182]. The WHO lists Disease X, along with eight additional priority diseases, including Zika virus, Ebola virus, and severe acute respiratory syndrome (SARS), as capable of causing serious outbreaks[182]. A wide range of pathogens, including viruses, bacteria, protozoa, fungi, and parasites are responsible for emerging infectious diseases (EIDs). Zoonotic carriers represent the most common source of infectious diseases, with wildlife encroachment and an increase in wildlife interactions elevating the rate of spillover events[181]. Furthermore, factors such as human population density and antibiotic use are contributing to an increase in the emergence of non-zoonotic pathogens. The interconnectivity of today’s global society further magnifies the challenge of containing diseases once they begin to spread[177,181].

The COVID-19 pandemic illuminated many deficiencies in global pandemic response. Interventions including social distancing, travel bans, and lockdown are effective at stemming disease spread if adopted widely and early, but the social and economic costs are substantial[183,184]. Vaccines have played an important role in mitigating disease prevalence, yet challenges such as emergent viral strains and public vaccine hesitancy can compromise their overall effectiveness[185]. Additionally, the development time required for effective vaccines limits their immediate utility in responding to disease outbreaks[185,186]. Diagnostic testing has emerged as a key strategy for reducing viral spread, but it also faces challenges including issues of accessibility, accuracy, and scalability [187–190].

5.1.2 Diagnostic Strategies of COVID-19

Diagnostic testing may be categorized into two approaches: symptomatic diagnosis and population level screening[190]. Testing of symptomatic individuals helps to inform therapeutic treatments and provides information on the level of positivity in the community. However, asymptomatic carriers accounted for over 32% of SARS-CoV-2 Omicron infections, meaning symptomatic testing alone is not adequate to contain spread[191–193]. In contrast, population screening offers a strategy for controlling outbreaks by identifying and isolating infected individuals, even when asymptomatic or presymptomatic[190]. Multiple studies from the COVID-19 pandemic have suggested population screening reduces the transmission rate within the community tested[190,194]. While the ideal testing strategy and required testing capacity remains undetermined, population screening in combination with contract tracing and isolation of infected individuals is one of the few countermeasures available in the context of emerging infectious diseases. However, attaining the capacity for population level screening poses a significant challenge[190].

Lack of testing capacity was most notable during the early stages of the COVID-19 pandemic[195,196]. The time required to develop a diagnostic test in combination with the requirements of mass manufacturing and test administration all contribute to the challenges of scaling testing capacity[188,190,197]. Researchers were able to develop a reverse transcription-polymerase chain reaction (RT-PCR) test within hours of receiving the published viral genome and within one month, RT-PCR diagnostic tests were approved under emergency use authorization (EUA) by the United States Food and Drug Administration (FDA) [198]. This short turnaround time elucidates current capabilities of scientists and researchers to look at the genomes of pathogens and quickly generate diagnostic tests. With the help of computational tools, researchers can select an abundant, unique, and highly conserved RNA (or DNA) target sequence from the pathogen genome and design diagnostics specific to the sequence[199]. This results in tests that are sensitive to small amounts of viral material, specific to the pathogen of interest, and more capable of being adapted to future mutants[200]. The ability to generate these tools extends to every pathogen with a known DNA or RNA sequence, making it particularly well positioned for timely deployment in outbreak scenarios[201].

5.1.3 Diagnostic Capacity, Accuracy, and Throughput: How Many Tests Do We Need?

There is no definitive evidence that a specific testing strategy or testing capacity can contain an outbreak or prevent a pandemic. However, data from past outbreaks strongly suggests that diagnostics can play critical roles in outbreak management[190]. For example, a study modeling the 2013 Ebola epidemic in West Africa suggests that diagnosing just 60% of patients in one day instead of five days could have contained the viral spread. In reality, delays led to an infection rate of over 80%[188,202]. Testing delays and insufficient capacity resulted in additional lives lost and billions of dollars in extra costs due to this inadequate response. Similar relationships are suggested for outbreaks of diseases including Ebola, Lassa Fever, and Zika, where testing provides a critical tool for infection identification, but lack of capacity and delayed deployment significantly reduce the ability for diagnostics to contain outbreaks[188].

The COVID-19 pandemic further illuminated the critical role diagnostics fill, most notably in identifying asymptomatic infections. Estimates suggest that between 20-60% of COVID-19 cases were mildly symptomatic or asymptomatic, with many of these cases still capable of spreading the disease[203]. The limited testing capacity, often reserved for symptomatic individuals, meant many COVID-19 cases went undetected, contributing significantly to the pandemic's spread. Notably, studies testing entire populations during the COVID-19 pandemic show marginal results. In October 2020, the country of Slovakia tested its entire population using rapid antigen tests. A decrease in reproduction number was observed in areas of high viral prevalence; however, areas of low viral prevalence saw little effect from the monumental testing effort which required significant resources and logistical planning[190,194]. However, this was most likely associated with the sensitivity (< 80%) of rapid antigen tests used and the lack of validation with RT-PCR, resulting in significant numbers of false negative tests[194].

The question of how many tests are needed to contain an outbreak does not have a simple answer. However, metrics like test positivity rates and the pathogen's reproductive number can provide insights into whether testing efforts are sufficient[188,190]. Studies of viral load dynamics suggest that tests with rapid turnaround times, even if less sensitive, can be effective in identifying and isolating infectious individuals. In this context, timely, widespread, and accessible testing plays a critical role in controlling the spread of disease. The more efficiently and quickly testing resources are mobilized, the more effective they become[204].

5.1.4 Desirable Characteristics of Diagnostics in the Context of Disease Response

Effective diagnostics are critical for managing infectious diseases, particularly in resource-limited settings where access to healthcare is constrained. The REASSURED diagnostics framework lists the characteristics that make diagnostics tests ideal: real-time connectivity, ease of specimen collection, affordability, sensitive, specific, user-friendly, rapid and robust, equipment free operation, and deliverable to end-users[205]. This framework outlines the many facets of diagnostics in terms of providing tests that are accessible and effective. Point-of-care (POC) diagnostics are particularly desirable, as they can be conducted near or by the patient, providing fast and actionable results without the need for centralized laboratories. Paperfluidic rapid antigen tests are examples of this approach and are routinely and effectively used to diagnose infections including malaria, human immunodeficiency virus (HIV), and syphilis[205].

However, the balance between sensitivity, affordability, and accessibility remains a challenge. While rapid diagnostic tests like paper fluidic antigen tests are effective for widespread, low-cost screening, there is currently a tradeoff between sensitivity and simplicity, which can lead to false negatives[200,205]. The evolution of molecular diagnostics, particularly nucleic acid amplification tests (NAATs), offers a more sensitive alternative, but requires sophisticated instruments and technical expertise. To better understand these tradeoffs, the following sections will cover two major categories of diagnostics: polymerase chain reaction (PCR) and rapid antigen tests, followed by a discussion of isothermal nucleic acid amplification, which aims to bridge the gap between sensitivity and simplicity in diagnostic testing.

5.1.5 Polymerase Chain Reaction Diagnostics

PCR testing is widely regarded as the current gold standard for pathogen diagnostics due to its high sensitivity and specificity[206]. PCR works by amplifying small quantities of DNA (or RNA) in a sample, such as saliva or mucus, to detectable levels. The process involves repeated heating and cooling cycles, known as thermocycling, which facilitates the replication of pathogen-specific nucleic acid sequences. Key to this process are primers, which are short sequences of nucleotides designed to match specific regions of the pathogens DNA. These primers bind, or anneal, to complementary sequences during the thermocycling process, initiating their replication[207].

Primers guide a DNA polymerase enzyme, which begins to synthesize new DNA strands starting from the primer location. The specificity of the primers ensures that only the pathogen's genetic material is amplified, allowing for highly targeted detection. In a typical PCR run, 25-40 cycles of this amplification are performed, with each cycle doubling the amount of the target sequence, enabling detection even when only small quantities of pathogen DNA or RNA are present in the initial sample[207]. This entire process often takes 2-6 hours, depending on the batch size and the thermocycling machine used[200].

To measure sequence abundance, researchers typically include a DNA intercalating fluorescent dye which actively inserts between the base pairs of DNA, causing a structural change in the dye that results in increased fluorescence. This fluorescence is correlated with the amount of amplified DNA present in the reaction. Optical systems, either integrated into the thermocycling machine, or standalone instruments, measure the fluorescence of the assay. Alternative methods of diagnostic readout including turbidity and color change are also available (see 5.1.8).

PCR's reliability and utility in research laboratories is well-established. However, its reliance on expensive precision equipment and skilled technicians poses challenges for adapting to efforts of high-throughput population screening. During the COVID-19 pandemic, major diagnostic efforts were carried out using high-throughput PCR machines such as the Cobas 8800 (Roche Molecular Diagnostics) and the Abbott Molecular m2000 (Table 5.1). These machines enable the automation of some RT-PCR workflow steps including nucleic acid extraction, purification, amplification, and detection. However, the complexity of these tasks necessitates complex precision systems. Some example systems used for central laboratory PCR testing during the COVID-19 pandemic are shown in Table 5.1. Beyond the cost and complexity, these machines still require significant hands on time (HoT) and run time to produce results and thus have relatively low throughputs in the context of population level screening[200].

The highest throughput of any system listed is the Cobas 8800, with an average throughput of 132 samples per hour. While its throughput is impressive, the Cobas 8800 is a large, complex, industrial machine costing on the order of $600,000 and weighing 2405 kg[208,209]. These machines are well suited for laboratory use and support a wide range of assays[210]. However, their size, complexity, and cost make them impractical for deployment in low-resource areas, where more accessible and deployable diagnostic solutions are needed. Moreover, the multi-step PCR workflow requires significant use of reagents and consumables, such as pipette tips, which became limiting factors during the spread of COVID-19[196]. As a result, accomplishing PCR testing at scale currently requires a large amount of capital and human resource, with only the most affluent countries of the world able to afford the cost of administering these tests at scale.

PCR System	Hands on Time (HoT)	HoT min/sample	Workflow Throughput	Averaged Hourly Throughput	References
Cobas 6800	58 min/297	0.2	384 /8hr	48	[200,211,212]
Cobas 8800	60 min/960	0.06	960-1,056 /8hr	132	[200,210]
Abbot m2000	75 min/135	0.5	470 /24hr	20	[200,213,214]
Hologic Panther (Fusion)	2hr/120	1	335 /8hr	42	[215]
Hologic Aptima (Aptima)	2hr/120	1	275 /8hr	34	[215]
BioFire Defense	36min/12	3	72 /8hr	9	[215]

Table 5.1. Comparison of commercially available laboratory PCR platforms.

Diagnostic Method	**Sensitivity**	**Specificity**	**Limit of Detection (copies/mL)**	**Approximate Time to Result**	**Cost Per Test**	**Time to FDA EUA from coronavirus detection**	**First Published diagnostic**
RT-PCR	96% ** [216]	100% [216]	1-100 [217]	45 minutes - 9 hours [200,212,218]	$51-101 [219]	28 days [220]	Jan 21 2020 [199]
RT-LAMP	92%** [216]	99% [216]	1e6*** [221,222]	11-45 minutes [223,224]	$3-50 [225,226]	181 days [227]	April 9 2020 [228]
Rapid Antigen	34-88%* [217,229,230]	99% [217,230]	1e6-1e7 [217]	5-30 minutes [217]	$10-45 [219,231]	120 days [227,232]	N/A

Table 5.2. Comparison of common diagnostic testing methods.

* 34% Among asymptomatic patients.

**Patient Positivity

***1000 RNA copies / reaction (1uL for RT-LAM, 10 uL for PCR)

5.1.6 Rapid Antigen Diagnostics

Rapid antigen tests operate by using antibodies to detect specific pathogen antigens, such as proteins, which may be present in patient samples. A common form of antigen test is the lateral flow test (LFT), wherein a cellulose pad containing the test nanoparticles carries the patient sample and detects the presence of infection. In brief, the patient mixes their sample (e.g. blood, urine, saliva, or vaginal swabs) with a buffer solution and applies a small amount of the mixture to the cellulose strip. Here, the sample interacts with the antibody nanoparticles and capillary action drives flow. Color changing indicators further down the strip use additional antibodies for both the same pathogen antigen (Test) or the antibody alone (Control) to identify if pathogen specific antibodies captured antigens, indicating a positive or negative result within 5-30 minutes[217].

The FDA approved the first rapid antigen test for COVID-19 roughly three months after the first RT-PCR test became available[217,233]. The typical development time for antibody-based tests is on the order of years, but increased investment and the urgency of the COVID-19 pandemic accelerated the development of LFTs for SARS-CoV-2[217]. Although an expedited development time relative to past antigen tests, the urgency of diagnostic deployment as a countermeasure marks this timeline as less than ideal for outbreak response. In the example of COVID-19, by the time of the first LFT there had been nearly 5.8 million reported cases and more than 360,000 deaths worldwide[234].

The test's operational simplicity, self-administration, and short time-to-result make it an efficient, low cost, point-of-care diagnostic tool. However, lacking molecular amplification, rapid antigen tests are less sensitive than NAATs and are more susceptible to false negatives. A meta-analysis of COVID-19 data, including 8,360 positive and 34,674 negative samples, reported 69% sensitivity compared to PCR. This indicates that 31% of individuals that tested positive by RT- PCR tested false negative with a rapid antigen test[230]. Although lateral flow rapid antigen tests represent one of the most accessible diagnostic platforms currently available, the critical shortfalls of development time and sensitivity limit their applicability in outbreaks of unknown pathogens[205,217]. Novel methods of antibody development using artificial intelligence may significantly change deployment timelines in the future[235]. The efficacy of antigen tests may also be disease specific. Given the viral load dynamics of SARS-CoV-2 and the prevalence of asymptomatic carriers, the increased sensitivity of RT-PCR is able to detect SARS-CoV-2 infections 24-48 hours before rapid antigen tests[204]. However, this differential may change depending on the infection and the dynamics of viral loading, and antigen tests may be more or less effective depending on the pathogen[236].

5.1.7 Isothermal Nucleic Acid Amplification Diagnostics

Isothermal amplification, like PCR, is a form of nucleic acid amplification test (NAAT). Both methods amplify specific pathogen nucleic acid sequence(s) present in a sample, enhancing the sensitivity of detection. Reverse transcription loop-mediated isothermal amplification (RT-LAMP) is a highly specific and sensitive isothermal NAAT. Unlike PCR, RT-LAMP amplifies nucleic acids continuously at a single temperature (65°C) (Figure 5.1). A clever combination of six distinct primers and a strand-displacing polymerase creates a continuous cycle of nucleic acid amplification[224]. Heated aluminum blocks, water baths, and other simple heating methods can drive isothermal amplification[237]. RT-LAMP is relatively resilient to variations in temperature, pH, and incubation time, creating opportunities for lower-cost incubation equipment and a more robust assay overall[238–240]. Opportunities to utilize conveyor ovens or similar continuous heating methods may be an option for high throughput incubation.

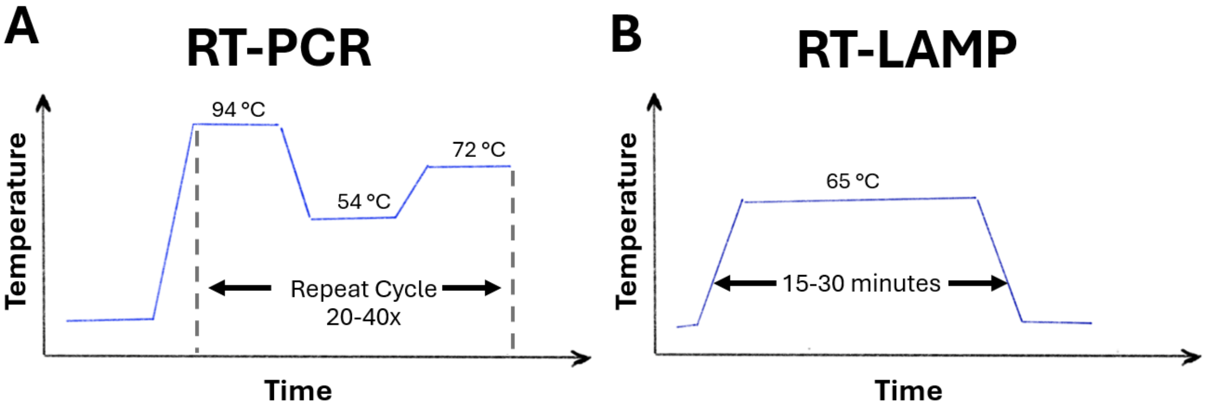

Figure 5.1. Incubation profiles for RT-PCR and RT-LAMP. (A) RT-PCR requires thermal cycling, modulating the temperature of the assay between three temperatures 20-40 times to complete the amplification process. (B) RT-LAMP is capable of continuous amplification at a single temperature.

5.1.8 Nucleic Acid Amplification Readout

NAATs, including RT-LAMP assays, utilize various methods for readout including turbidity, color changing dyes, or fluorescent dyes. Turbidity and color changing dyes enable measurement with the naked eye or photosensitive sensors (e.g. cameras or photodiodes)[241]. In RT-LAMP assays, turbidity is generated due to the formation of magnesium pyrophosphate as a byproduct of the amplification reaction. Increased turbidity (i.e. cloudiness), as measured manually or with a spectrophotometer, can be used to determine the result of the assay[242]. Similarly, color-changing dyes are commonly used as visual indicators for NAATs. These dyes are sensitive to specific chemical reactions, such as changes in pH, that occur during the amplification process[243]. This color change can be detected either manually by a technician or through photosensitive sensors, such as cameras and photodiodes[221,244]. However, both turbidity and color changing dyes pose challenges in population scale testing, where manual detection can introduce human error and reduce scalability.

Fluorescence-based detection is a widely used method for readout in both PCR based and LAMP based assays. While fluorescence requires more equipment compared to visual methods – such as an excitation light source, emission filter, and photosensitive detector – the strong, easily quantifiable signals it produces make these methods effective for assay readout. DNA intercalating dyes, such as SYBR green, are commonly used for fluorescence detection[241]. These dyes bind to any DNA present, and their interaction (i.e. DNA intercalation) increases the dye fluorescence. Some intercalating dyes can inhibit the amplification reaction, necessitating an open-tube method where the dye is added post-amplification. While this process is amenable to laboratory settings, it reduces throughput in high-volume testing environments and poses significant contamination risk. Successful amplification of a DNA sequence produces high concentration of amplicons, or amplified DNA sequences, which if released from the tubes, pose significant cross contamination risks upstream into pre-amplified test tubes. Furthermore, turbidity, colorimetric dyes, and intercalating dyes are all sequence-independent, meaning they measure the total amplification of any DNA, not just the sequence of interest. Unintended amplification of off-target sequences is possible with RT-LAMP and other NAATs, making sequence-independent detection methods prone to false positives[245].

Sequence-dependent indication methods specifically target the sequence of interest. For instance, quenching of unincorporated amplification signal reporters (QUASR) fluorescently label amplicons. In the case of RT-LAMP, a QUASR probe replaces one of the six primers. The probe functions similarly to the original RT-LAMP primer while also emitting fluorescence when incorporated. A complementary quencher probe binds to any unincorporated QUASR probes, quenching the fluorescent signal. This quenching mechanism is temperature dependent and is only active below the typical incubation temperature of LAMP (< 55°C). Therefore, cooling the reaction to ambient temperature before measurement effectively quenches any unincorporated QUASR probes, yielding a specific reporter fluorescence signal corresponding to the DNA sequence of interest[245]. The accessibility and the adaptability of RT-LAMP make it a relatively low-cost NAAT, which aligns with the need for deployable, cost-effective, and high-throughput diagnostic solutions[243,246].

5.1.9 Innovative Approaches in Diagnostic Testing

Several PCR-based and LAMP-based diagnostic systems have been proposed to address the challenges of affordability, portability, and throughput. Mendoza-Gallegos et al. developed a 3D-printed thermocycler as an affordable, portable quantitative PCR (qPCR) instrument. Made from 3D-printed parts and off-the-shelf components such as a 5 W resistor, fan, blue LED, and CMOS camera, the system offers a cost-effective alternative to commercial benchtop thermocyclers. However, its single-channel design limits throughput, making it more suitable for small-scale testing rather than community-scale diagnostics[247].

To address challenges associated with throughput, Wu et al. developed a High-throughput Optical Fiber-integrated Immunosensing System (HFIS). This system uses microwell plates for immunoassays to detect SARS-CoV-2 nucleocapsid protein (NP). The system employs optical fibers and a smartphone-based reader to measure results, offering high sensitivity, low cost, and ease of use.

Several LAMP-based diagnostic systems have also been proposed. The FABL-8 system, developed by Buultjens et al. is an open-source RT-LAMP system designed for high-performance fluorescence detection. At a reported cost of $380, it uses a heat block, computer, and an optical system for detecting assay fluorescence[248]. While its low cost and portability are advantageous, the system is limited to processing only eight samples at a time, limiting the throughput to approximately 19 samples per hour. Similarly, Papadakis et al. developed a portable, battery-powered LAMP platform that uses colorimetric detection and a mini RGB camera to analyze results[249]. While highly portable and capable of running for 5 hours on battery power, its throughput is similarly constrained by the eight-sample capacity.

In the commercial space, LUCIRA health developed the first over-the-counter, at-home molecular test for COVID-19 using RT-LAMP technology[250]. The device allows for patient-collected nasal samples and delivers results in as little as 11 minutes[223]. Though convenient for home use, each single-use device costs around $50 and includes integrated heaters and detection hardware all powered by batteries, making it a costly and potentially wasteful option in the context of population scale testing. These systems highlight the ongoing innovation in diagnostics, balancing accessibility and cost with the need for high throughput solutions.

5.1.10 Developing Diagnostics for the Next Outbreak

Pandemics are defined as the *global* spread of disease. The interconnectivity of the global population means highly transmissible diseases are more likely to spread globally regardless of origin[181]. Ensuring equitable public health measures strengthens global capacity to respond to outbreaks. Investment in global health infrastructure is an important facet of pandemic preparedness. Initiatives such as the “100 Days Mission”, aim to deploy diagnostics, treatments, and vaccines within the first 100 days of an outbreak. An emphasis on having scalable, adaptable, and rapidly deployable technologies is critical to timely response[251]. Developing diagnostics that can be quickly developed, manufactured, and distributed during an outbreak is critical to these efforts.

Ultimately, the development of diagnostics for the next outbreak requires a proactive, global approach. It involves not only advancing the technologies for faster, more accurate testing but also ensuring that these technologies are accessible, affordable, and scalable in a global context. By investing in global health infrastructure and fostering innovation in diagnostics, the world can be better prepared against the next emerging infectious diseases.

CHAPTER SIX

RAPID PROTOTYPING OF DIAGNOSTIC METHODS AND METHODOLOGY

This chapter describes the application of 3D printing in the research and development of medical diagnostics. These sections serve to supplement the methods described in chapters 7 and 8. Using 3D printing we design, fabricate, and iterate several technologies including point-of-care (POC) devices, fluorescence detectors, and an automated device handling system. Utilizing principles of design for additive manufacturing and bottom-up design methodologies, we create prototypes that are easily fabricated and iterated.

6.1 Point-of-Care Diagnostic Device

In this section I describe the design of a POC device with the goal of facilitating RT-LAMP assays in a self-contained, user activated system. I include information on design choices, device functionality, device fabrication, and device integration within the proposed diagnostic workflow. Further details describing the device design and its function are included in Chapter 7.

6.1.1 Design of Point-of-Care RT-LAMP Diagnostic Device

POC tests are highly valued for their accessibility and ease of use, particularly in resource limited settings[200,205]. To approach POC testing using the current state of the art NAAT methods, we develop a novel method of sample collection, and an integrated diagnostic workflow based on a one-pot RT-LAMP NAAT. This workflow attempts to combine multiple functions – sample collection, reagent storage, assay mixing, incubation, and test readout. The result is a simple, patient-activated, low-cost, and high-throughput diagnostic method that leverages available molecular diagnostic technologies to create a high-throughput, POC diagnostic. The work to develop the POC device including the integration of assay reagents, patient sample metering, and patient actuation of the device will be described briefly here to provide context to the greater workflow.

6.1.2 Device Body Minimization

Device actuation and user ergonomics are key considerations in the design of the POC device. The device described in chapter 7 includes a syringe-like plunger, allowing thumb-driven actuation of the blister, resulting in a device sized to fit comfortably in the hand (Figure 6.1A). For overall optimization of material use, device packing in heating systems, and for high-throughput device detection schemes, a smaller more optimized device offers advantages.

To address this, I develop a minimized device body that retains compatibility with the same plunger and saliva forks operating scheme but removes the hand-sized plunger in favor of a button press thumb-actuation mechanism. This change reduces the device's size while maintaining similar functionality. The primary focus of this device design is to enhance integration into a high-throughput workflow. The smaller form factor improves packing efficiency and facilitates technician handling during incubation and assay readout. The compact shape also supports automated positioning.

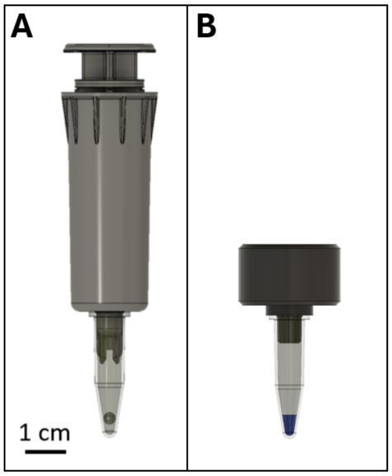

Figure 6.1. Render of point-of-care (POC) devices for RT-LAMP based assays. (A) Render of POC device designed for patient activation, featuring a plunger mechanism that actuates an integrated liquid-filled blister. This design is handheld and ergonomically optimized for thumb activation, similar to the action of clicking a pen (see Chapter 7). (B) Render of a minimized device body, providing proof-of-concept device for testing assay workflow. This design is optimized for packing efficiency, material use, and automated handling but is not a fully functional POC prototype (see Chapter 8). Scale bar represents 1 cm.

6.2 Design and Rapid Manufacturing of Custom Fluorescence Detectors

To accomplish assay readout, we design and build a fluorescence measurement system specific to the device and assay. For the proposed RT-LAMP assay, we include a fluorescence reporter dye and a fluorescence reference dye. These two fluorescence signals are measured to indicate the result of the assay (see Chapter 8). Laboratory tools like plate readers and thermocycling machines are capable of making these measurements; however, these machines are expensive and are based around laboratory specific assays and protocols, which can be restrictive in rapid-response or field settings typical of outbreak scenarios[210,252,253].

To address these limitations, we design and fabricate a custom fluorescence detector specifically engineered for high-throughput readout, aligning with the needs of POC testing. The primary goal of the fluorescence detector is to accurately and repeatedly optically measure two fluorescence channels to read out the results of each RT-LAMP assay. This goal is accomplished through the design and fabrication of an optical system tasked with both the illumination of the sample and the capture of the emitted fluorescence light (6.2.2). The second goal of the detector is to achieve high-throughput detection. This is accomplished through the active positioning of individual devices within the optical path using automated mechanization (6.2.3).

6.2.1 Fluorescence Detection Systems Prototyping

We develop a camera-based fluorescence detector prototype using a bottom-up approach, starting with the core functionalities like the LED illumination and camera/sample alignment, and subsequently building the remainder of the system around these core elements. Modularity and design for additive manufacturing are emphasized, leveraging 3D printing to improve prototype cycle time and ease of system iteration. FDM 3D printing (MK3S+, Prusa) using polyethylene terephthalate glycol (PETG, Hatchbox) is used to prototype and iterate the structural components. The initial prototypes were built around the optical system, consisting of a monochromatic camera to capture fluorescence emissions from samples illuminated by two LED sources (Figure 6.2). A commercially available macro camera lens (55 mm f/2.8 Micro Nikkor, Nikon) was adapted using a 3D printed mount, which integrated a dual-bandpass emission filter, filtering out non-fluorescent light from the camera's field of view.

For alignment, the detector uses stainless steel linear motion rods (8 mm, 6459K111, McMaster) to provide a rigid, high precision structure that supports the alignment of the optical components and the assay volume as visible in Figures 3.2 A, B. A 3D-printed LED mounting system positions the LEDs at 45-degree angles, obliquely illuminating the microcentrifuge tube containing the sample Figures 3.2 B. The LEDs are integrated into the sample holder to ensure consistent alignment between the LEDs, assay volume, and the camera. As the prototype evolved, the camera lens was updated (16 mm CS-mount, Arducam) to optimize sensor usage and reduce the overall footprint and size of the detector system. Figure 6.2D shows the entire detector system consisting of the Raspberry Pi (i), the Arduino microcontroller (ii), and the detector (iii) housing the camera, LEDs, and sample holder.

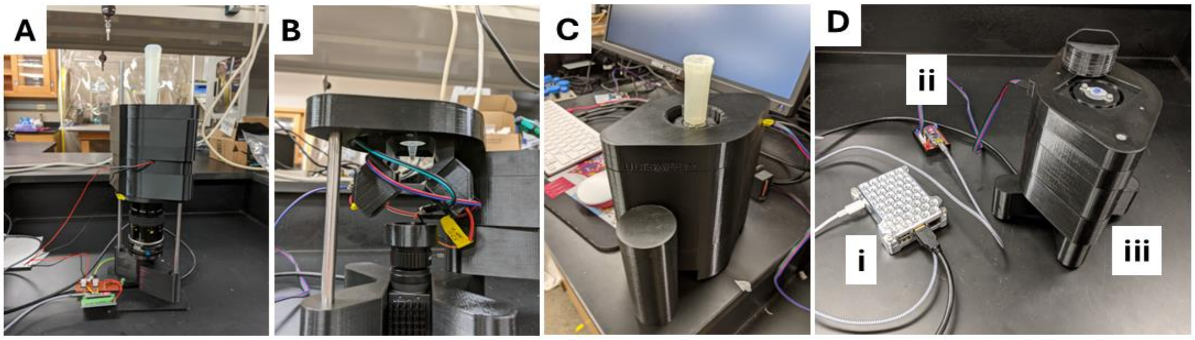

Figure 6.2. Initial prototyping of camera-based fluorescence detector. (A) Image of first prototype fluorescence detector featuring a standard photography camera lens, integrated excitation filter between the lens and camera body, and stainless-steel rods to support camera/sample alignment. (B) The top assembly of the fluorescence detector features a sample holder, and two LED mounts angled up at 45 degrees, obliquely illuminating the bottom of the microcentrifuge tube as depicted. (C) Updated camera lens and light blocking case enable reduction in size. A device is shown in the fluorescence measurement position in the top of the detector with the camera facing up from below, concealed by the detector's case. (D**)** The full detector system consists of: i) a single board computer, ii) a microcontroller, and iii) the fluorescence detector with integrated camera and LEDs.

6.2.2 Adaptation of Fluorescence Detector for High-Throughput Detection using 3D Printing

The fluorescence detector prototype supports the measurement of assay volumes individually. Manual positioning of the samples by a technician is required for each sample, limiting the throughput of detection. Given camera-based fluorescence measurement for the described optical system requires less than one second, sample positioning becomes the limiting factor in terms of measurement throughput. This limit is addressed by a motorized positioning system integrated into the fluorescence detector.

Following a bottom-up approach, we prioritize precise and repeatable positioning of devices. We use a rotary carousel design for its simplicity, requiring only a single stepper motor to reliably move each test into the optical path (Figure 6.3). A modular five-point hub on the motor shaft allows for quick interchange (Figure 6.3A, B). Several different designs were tested to prevent jamming and to ensure consistent sample pick-up with each rotary step. Figure 6.3 D shows the carousel and inlet prototype without any optical systems. This depicts a modular prototype developed to test device motion and stepper motor integration. Figure 6.3 E shows the integration of the device positioning carousel with the optical system subassembly. This prototype demonstrates the complete functional detection system, excluding the light enclosure. The light enclosure was designed around the positioning and optical systems, resulting in a unique angular design (Figure 6.4C). This enclosure was designed to minimize material usage and be 3D printable without supports, forming a tilted shell that effectively provides structure and blocks light to the internal components. The enclosure also features an access door to enable technician operation and hardware updates.

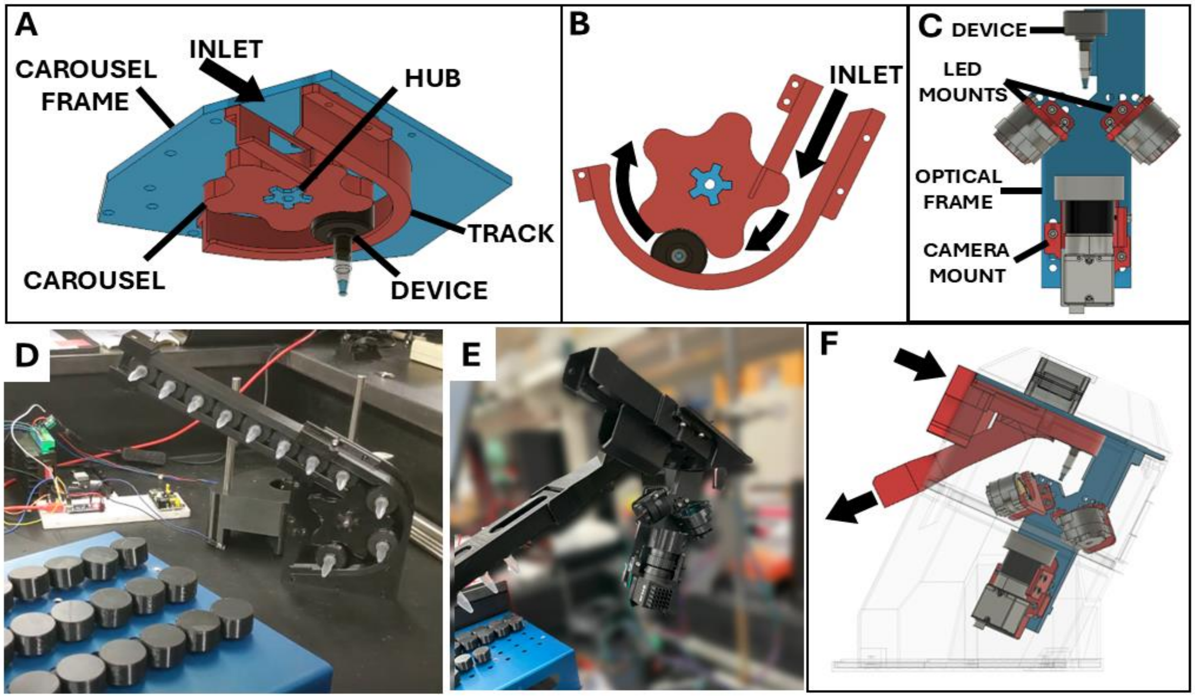

Figure 6.3. Development of high-throughput detector subsystems. (A) Render of the carousel assembly featuring a frame (blue) and modular carousel components (red). The device positioning carousel, optical subassembly, and device track all interface with the carousel frame. (B) Device tracks guide the devices into the carousel. (C) Render of optical sub assembly. The LEDs, filters, and camera all interface with the frame (blue) through 3D printed mounts (red). (D) Minimal functional prototype of active positioning carousel featuring a stepper motor and modular carousel design. (E) Image of carousel prototype with optical subassembly attached positioned at an angle for gravity fed devices. (F) Render of detector including subassemblies and modular components (red).

Modular Design and Adjustability

To better support prototype iteration, we use modular design. The active positioning system and the optical system are designed as subassemblies as depicted by Figures 6.3A and 6.3C respectively. Within each subassembly, components that may need to be updated based on experimental results or changes to the assay can be designed to be modified, printed, and swapped out quickly and easily. Even though entire subassemblies could be printed as monolithic structures, the ability to modify and change only the necessary components reduces the iteration cycle time while also minimizing use of resources.

An optical subassembly frame acts as a central hub for all optical components, allowing independent modification and replacement (Figure 6.3C). The position of the LEDs, filters, sample, and camera can all be modified based on the specific assay and optical component requirements (e.g. camera focal length). This design also supports flexibility in adapting to new fluorescent probes or sample geometries, ensuring the system can accommodate changes in the assay or future diagnostic needs with minimal changes to the overall system. Heat set threaded inserts (M3x0.5mm, McMaster 94180A333) provide a simple method of providing reusable threaded fastening points. All optical subassembly printed components are printed in one piece without support, enabling fast fabrication with minimal post processing.

Following a similar design approach, the carousel is modular, and each component is designed for printability. A rigid main frame provides fastening points for modular components, including device tracks and the stepper motor (Figure 6.3A, B). This modularity enables rapid iteration and easy replacement. For example, a carousel design prints in approximately one hour and can be swapped in under 10 minutes. This flexibility in the carousel and track system supports efficient development and quick adjustments to critical system functions.

6.2.3 Device Handling

To support the handling and systematic processing of diagnostic devices, we construct racks and cartridges that transfer devices into and out of the detector (Figure 6.4). Device racks (fabricated by Huck Medical Technologies, Inc., Jacksonville, TX) hold five rows of six devices, with spacing aligned to an aluminum dry block heater insert. This alignment facilitates the simultaneous handling of device batches (1-30 devices). Device cartridges are used to transport rows of six devices from the racks into the detector, allowing technicians to efficiently load devices faster than the detector can process them (Figure 6.4 B,C). Device cartridges also serve to collect devices at the outlet, maintaining order and enabling organized data collection and replicate measurements. The cartridges feature a hinge and locking mechanism which mates and locks into the outlet and inlet of the detector. This feature enables the technician to quickly slot and lock the cartridge into the detector to either load or capture devices (Figure 6.4 B, C). This handling system enables repeated measurement of the experimental samples while maintaining the same sample ordering. Device barcoding or other methods would reduce the requirements of sample ordering. Furthermore, real-world testing may also dispose of devices safely following measurement while network interactions relay the test result to the patient.

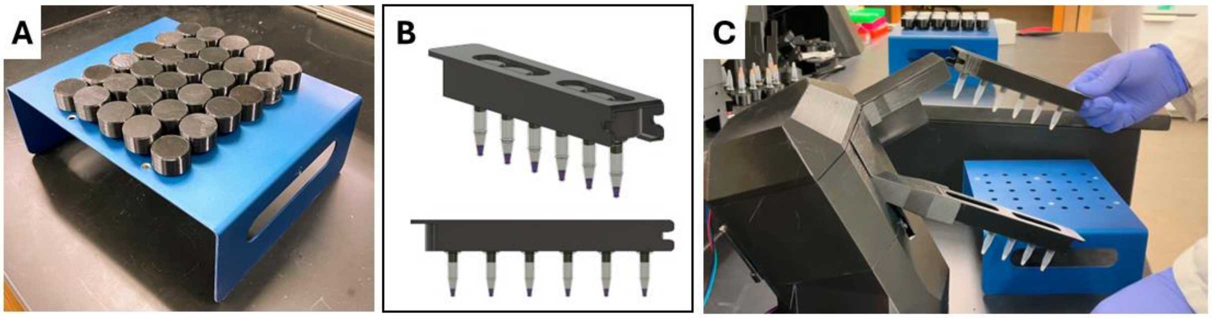

Figure 6.4. High-throughput device handling systems. (A) Device racks designed to transfer batches of tests into and out of heater. (B) Device cartridges are designed to transfer rows of devices into and out of the fluorescence detector. (C) Image of technician loading devices into the detector inlet, transferring a row of devices from the rack into the detector’s inlet. A separate cartridge catches devices at the outlet.

6.2.4 Fluorescence Measurement and Data Analysis

Fluorescence measurement serves as the indicator for determining assay results based on the relative intensities of two fluorescence signals (see Chapter 8). This dual-signal approach provides a robust and normalized metric for identifying successful nucleic acid amplification. During the measurement process, the detector captures two fluorescence signals. All data, including raw and background-subtracted fluorescence images, as well as calculated fluorescence ratios, are automatically stored by the system's single-board computer (Raspberry Pi) for traceability and later analysis. Data logs are generated for each set of measurements and saved as text files on the computer's hard drive. Custom C++ code processes the fluorescence ratios, and further analysis is performed using MATLAB. The MATLAB script reads the text files, which include raw fluorescence data, background-corrected values, calculated ratios, sample numbers, and sample names, ensuring efficient and organized data analysis (Appendix B).

CHAPTER SEVEN

SPOC-LAMP: SALIVA POINT-OF-CARE LAMP DEVICE FOR DETECTION OF SARS-COV-2

Contribution of Authors and Co-Authors

Manuscript in Chapter 7

Author: Thomas B. LeFevre Contributions: Technology development, experimental execution, data analysis, and manuscript writing and editing.

Co-Author: Isaak Thornton Contributions: Technology development, experimental execution, manuscript writing and editing.

Co-Author: Dimitri A. Bikos Contributions: Technology development, biochemistry, experimental execution.

Co-Author: Perry Ellis Contributions: Technology development, experimental execution.

Co-Author: Connie B. Chang Contributions: Research supervision, conceptualization, funding acquisition.

Co-Author: David A. Weitz Contributions: Research supervision, conceptualization, funding acquisition.

Co-Author: James N. Wilking Contributions: Research supervision, conceptualization, funding acquisition, and manuscript writing and editing.

Manuscript Information

Title: SPOC-LAMP: Saliva Point-of-Care LAMP Device for Detection of SARS-CoV-2

Authors: Thomas B. LeFevre[1,2], Isaak Thornton[2,3], Dimitri A. Bikos[1,3], Perry Ellis[4], Connie B. Chang[7], Michael R. Pavia, David A. Weitz[4,5,6], and James N. Wilking[7]*

[1]Department of Chemical and Biological Engineering,
[2]Department of Mechanical and Industrial Engineering,
[3]Center for Biofilm Engineering,
Montana State University, Bozeman, MT, USA
[4]John A. Paulson School of Engineering and Applied Sciences, Harvard University, Cambridge, MA, USA;
[5]Department of Physics, Harvard University, Cambridge, MA, USA; and
[6]Wyss Institute for Biologically Inspired Engineering, Harvard University, Boston, MA, USA
[7]Department of Physiology and Biomedical Engineering, Mayo Clinic, Rochester, MN

*Corresponding author

Status of Manuscript:
☒ Prepared for submission to a peer-reviewed journal
☐ Officially submitted to a peer-reviewed journal
☐ Accepted by a peer-reviewed journal
☐ Published in a peer-reviewed journal

Acknowledgments

This work was supported by ULTSafety, Inc.

Abstract

Human microbial pathogens including viruses, bacteria, and fungi pose a profound threat to human health, as evidenced by the SARS-CoV-2 global pandemic. To limit the spread of infectious disease, frequent, widespread diagnostic testing is critical. Specifically, there is a need for low-cost, accurate point-of-care (POC) molecular assays. Isothermal amplification methods offer a potential solution, and molecular-based POC tests offer tremendous potential for rapid, accurate POC testing, but to keep reagent costs low, methods for aliquoting exact volumes of specimen sample onto the assay device are needed. Here, we describe a low-cost, hand-held, manually operated device for rapid POC pathogen detection. The device includes a two-pronged fork geometry which enables transfer of small volumes of saliva from flocked collection swabs and contains all reagents needed for isothermal nucleic acid amplification and fluorescence detection. We describe the design and operation of the device and demonstrate use of the device for isothermal nucleic acid amplification and fluorescence detection using loop-mediated isothermal amplification of the SARS-CoV-2 virus in saliva.

Introduction

Human microbial pathogens pose a profound threat to human health, as evidenced by the SARS-CoV-2 global pandemic[254]. To limit the spread of infectious disease, control measures like handwashing, respiratory masks, social distancing, contact tracing, and vaccination have been shown to be highly effective. Another critical control measure is diagnostic testing[255]. Frequent, widespread testing for infection has been shown to mitigate pathogen spread; yet, diagnostic tests for human microbial pathogen infections remain underdeveloped.

Diagnostic tests can be classified in several different ways. One defining attribute is the location where the test is performed. Laboratory-based tests[256–259] are performed in a laboratory separate from the sample collection site, whereas point-of-care[260–267] (POC) tests are performed directly at the collection site. Laboratory-based tests are generally more accurate and sensitive than POC tests, but more costly and time-intensive. Another defining attribute is the choice of infection marker. Molecular[268–271] tests detect pathogen genomic material, whereas antigen[272–275] tests detect the presence of pathogen proteins. Molecular tests are generally more accurate than antigen tests, but require genomic amplification, and thus are more costly and time intensive to perform.

Benchmark molecular diagnostic tests are based on the polymerase chain reaction (PCR)[276–279]. While these molecular tests have traditionally been laboratory based[280–283], a number of POC PCR-based tests have recently been developed[207,284,285]. Yet, these POC tests still require temperature cycling to amplify pathogen genomic material. A promising alternative is isothermal amplification[224,242,286,287], which achieves amplification at a constant temperature and does not require thermocycling equipment, allowing them to be performed with minimal training in a POC environment. These isothermal, molecular-based POC tests offer tremendous potential for rapid, accurate POC testing. However, the cost of each assay remains high, largely because of the cost of isothermal amplification enzymes. To minimize the cost of POC isothermal molecular assays, methods for aliquoting exact volumes of specimen samples onto the assay device are required. Without this, the cost of POC assays will limit frequent, widespread diagnostic testing.

Here, we describe a low-cost, hand-held, manually operated device for rapid point-of-care pathogen detection. The device includes a two-pronged fork geometry which enables transfer of small volumes of saliva from flocked collection swabs and contains all reagents needed for isothermal nucleic acid amplification and fluorescence detection. We describe the design and operation of the device, including a geometry for optimal transfer of saliva from a sample collection swab to device, a one-step actuation that requires minimal forces and provides tactile user feedback. Finally, we demonstrate use of the device for isothermal nucleic acid amplification and fluorescence detection using loop-mediated isothermal amplification of the SARS-CoV-2 virus in saliva.

Results and Discussion

The device consists of two main portions, an upper syringe-type portion, and a microcentrifuge tube, as illustrated in Figure 7.1A. The syringe-type portion contains a plunger and a liquid-filled blister pack adhered to the inside floor of the syringe cylinder. Before device actuation, the plunger is positioned inside the syringe cylinder in a raised position (Figure 7.1B, left). Depression of the plunger compresses the blister and presses the foil-sealed underside of the blister against spikes (Figure 7.1B, middle). This action pierces the foil, driving liquid into the tube beneath. Liquid expelled from the blister carries the saliva sample with it and mixes with lyophilized reagent.

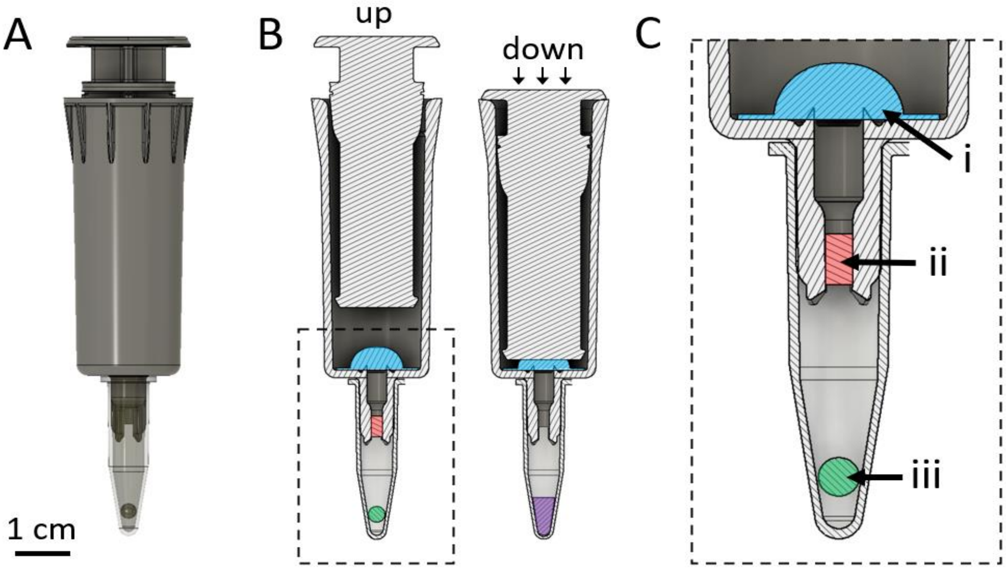

Figure 7.1. Device overview. (A) Illustration of the assembled device consisting of an upper syringe-type portion and lower microcentrifuge tube. (B) Cross-sectional view of device with plunger in the “up” and “down” positions. Pressing the plunger compresses and ruptures the blister (blue), driving liquid and saliva (pink) into the tube with the lyophilized reagent (green), resulting in a mixture (purple). Region enclosed by a dashed line is an expanded view of the lower portion of device: (i) liquid filled blister, (ii) saliva sample and (iii) lyophilized reagents. An expanded view of the lower portion of the device highlights the blister pack, spikes, and sample fork features (Figure 7.1B, dashed line).

To conduct the assay, three components are required: the syringe-type device containing a liquid-filled blister pack with the plunger in the “up” position, a flocked specimen swab, and a microcentrifuge tube (Figure 7.2A). The tube contains lyophilized reagent and is sealed with a laminate foil seal to protect the lyophilized reagent. Test operation steps are as follows. First, to collect saliva, the swab is removed from its packaging and the flocked end of the swab placed in the mouth for 10-20 s (Figure 7.2B). To transfer saliva from the swab to device, the swab is then drawn through the forks of the device (Figure 7.2C). The foil-sealed microcentrifuge tube is then pressed onto the forks with the beveled fork points piercing the foil until the rim of the tube fits snugly over the base of the forks (Figure 7.2D). Finally, the device is gripped in one hand and the plunger depressed by thumb until the plunger top is fully seated in the device tube (Figure 7.2E). Saliva, blister contents, and lyophilized reagents are now combined at the bottom of the vial (Figure 7.2F).

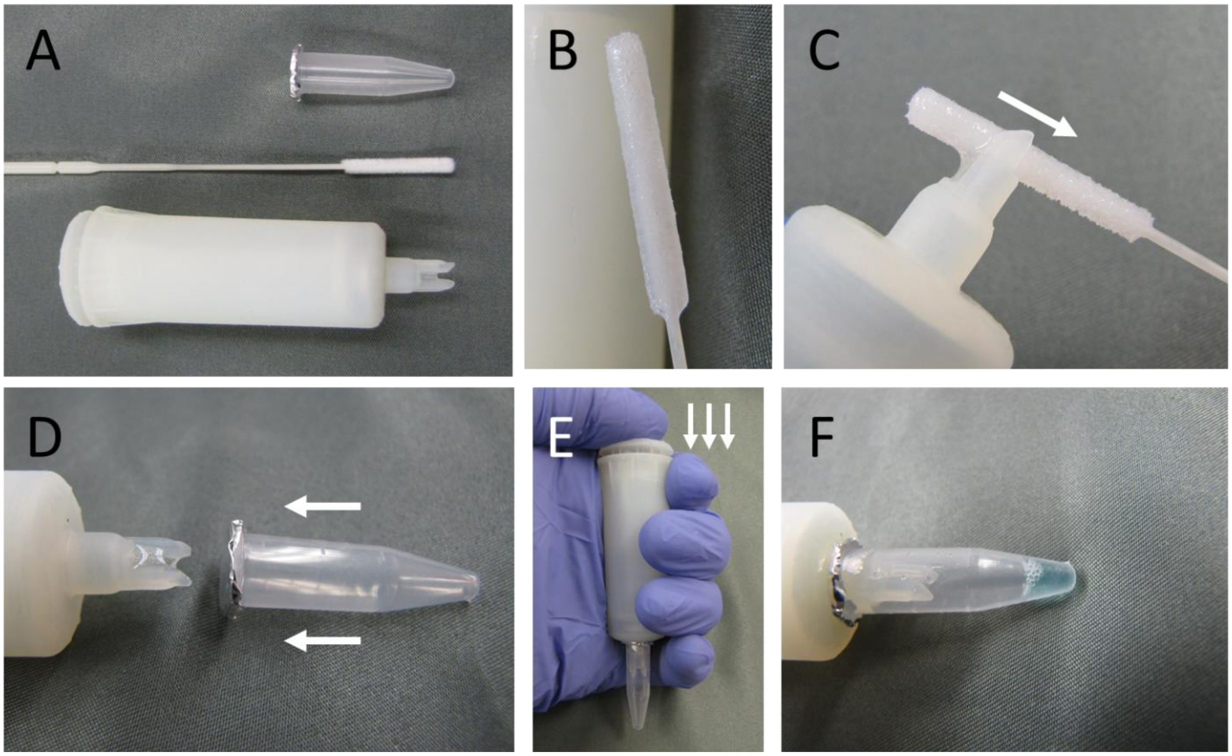

Figure 7.2. Device operation. (A) Components of the test include syringe-type device, flocked specimen swab, and vial. Lyophilized reagent in vial not shown. (B) Saliva is collected by soaking the swab in the mouth for 10 – 20 s. (C) Saliva is then transferred to the device by drawing the swab through device forks. (D) The tube is attached to the device by pushing the forks through the foil seal. (E) The plunger is depressed to express blister contents through the forks into the vial. (F) Saliva, blister contents, and lyophilized reagents are now combined at the bottom of the tube. Blue dye is included for visualization.

A critical feature of the device are the device forks, which enable small volumes of saliva to be transferred from the collection swab to the device. The forks are composed of two prongs separated by a gap distance d as illustrated in Figure 7.3A. As a swab is drawn between the forks, a combination of surface wetting, swab fiber compression, and gravity draws saliva from the swab to the device and the trough beneath, as shown by the series of high-speed images in Figure 7.3B. To determine an ideal d, we measure the saliva transfer volume V_F from a flocked swab with a flock tip outer diameter d_{swab} from devices over the range 1.3 mm $\leq d \leq$ 2.3 mm. The data does not show a strong correlation between d and V_F. The experiments resulted in an average V_F of approximately 13 – 20 uL. However, there was an apparent optimal d based on usability. We chose $d = 1.7$ mm. At $d < 1.7$ mm, it became difficult to draw the swab through the forks, which is undesirable from a user standpoint and resulted in greater variance in V_F. At $d > 1.7$ mm, it was more difficult to tell if the swab drag had been done correctly because there was less frictional tactile feedback as the swab was drawn through the forks, and anecdotally it seemed that a low volume swab with $V_S < 60$ µL had a higher risk of depositing a very low trace amount of saliva when d was significantly above 1.7 mm. It was also clear that other d would have likely worked but $d = 1.7$ mm seemed to be a reasonable choice. Primarily, we didn't want to risk getting zero saliva and that risk seemed greater at higher d.

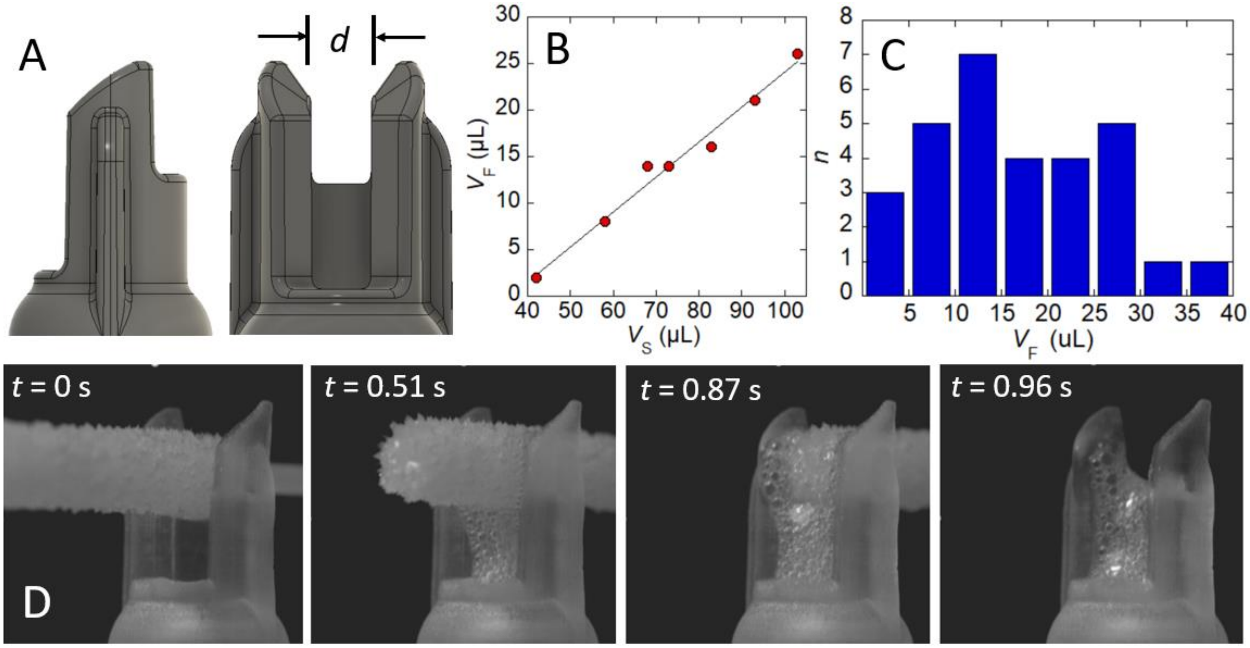

Figure 7.3. Saliva transfer from swab to device. (A) Geometry of device forks. Forks beveled to pierce tube foil seal. (B) Saliva volume transferred between device forks VF plotted as a function of saliva volume in swab VS. Line is linear fit. (C) Histogram of VF for multiple individuals. (D) Time-lapse image series of saliva transfer process captured at 3000 fps. We find that VF is proportional to the volume of saliva contained in the collection swab VS, as shown by the plot in Figure 7.3C. To get a measure of the variability in VF between individuals, we recruit ten individuals to collect and transfer their own saliva from swab to device (n = 3 each). Plotting the data, we find a distribution in VF with a peak near 10-15 µL (Figure 7.3D) with an average of 16.3 µL. This volume of saliva is sufficient to detect low pathogen counts while keeping reagent costs low.

For most molecular diagnostic assays, delivery of exact volumes of aqueous media to the reaction tube is critical. To accomplish this, we design the plunger to translate by a well-defined distance and compress the blister by an exact amount. The initial position of the plunger is held in place by a positive snap ring in the syringe which seats within a negative feature in the plunger (Figure 7.4A). The mirror symmetry of the negative feature also resists removal of the plunger from the tube. The final position of the plunger is set by contact between the underside of the plunger rim and the top rim of the syringe tube (Figure 7.4A). Compression of the blister and the corresponding expulsion of liquid is shown in the series of images in Figure 7.4B. Actuation of the device is easily achieved by grasping the device in a single hand and depressing the plunger by thumb. Actuation is accompanied by a tactile snap, which provides the user feedback of successful actuation.

The force required to complete the compression of a blister within our device is $F_b = 39.8$ N ± 10.9 N. Partial compression of the blister requires significantly less force than full compression; thus, we design the device such that plunger actuation does not fully compress the blister. To measure the force profile required to actuate the device, we perform blister device actuation measurements using a normal force transducer. We observe two peaks in the force profile. The first peak in the normal force corresponds to displacement of the negative feature in the plunger from the positive snap feature. Following this peak, the normal force drops but then increases again as the plunger begins to compress the blister (Fig 7.4C). We define this second, larger peak as the maximum force required to actuate the blister F_b. Device actuation during these measurements is performed with a fixed plunger translation velocity, $v = 0.1 - 0.5$ mm/s. By contrast, manual actuation is accomplished in a less controlled manner and at a significantly higher velocity. So, while this does not directly characterize the forces required when the plunger is actuated manually by hand because the rate of actuation is slower with a rheometer, it does provide some measure of the profile of resistance that the plunger is overcoming. That is because this force results in an acceleration of both the plunger and the user’s thumb that results in enough kinetic energy to help compress the blister dome without requiring additional effort from the user. We want the user to continue pressing on the plunger until it bottoms out, but not to have to exert extra force after the initial “snap” as the plunger disc moves past the snap ring of the syringe.

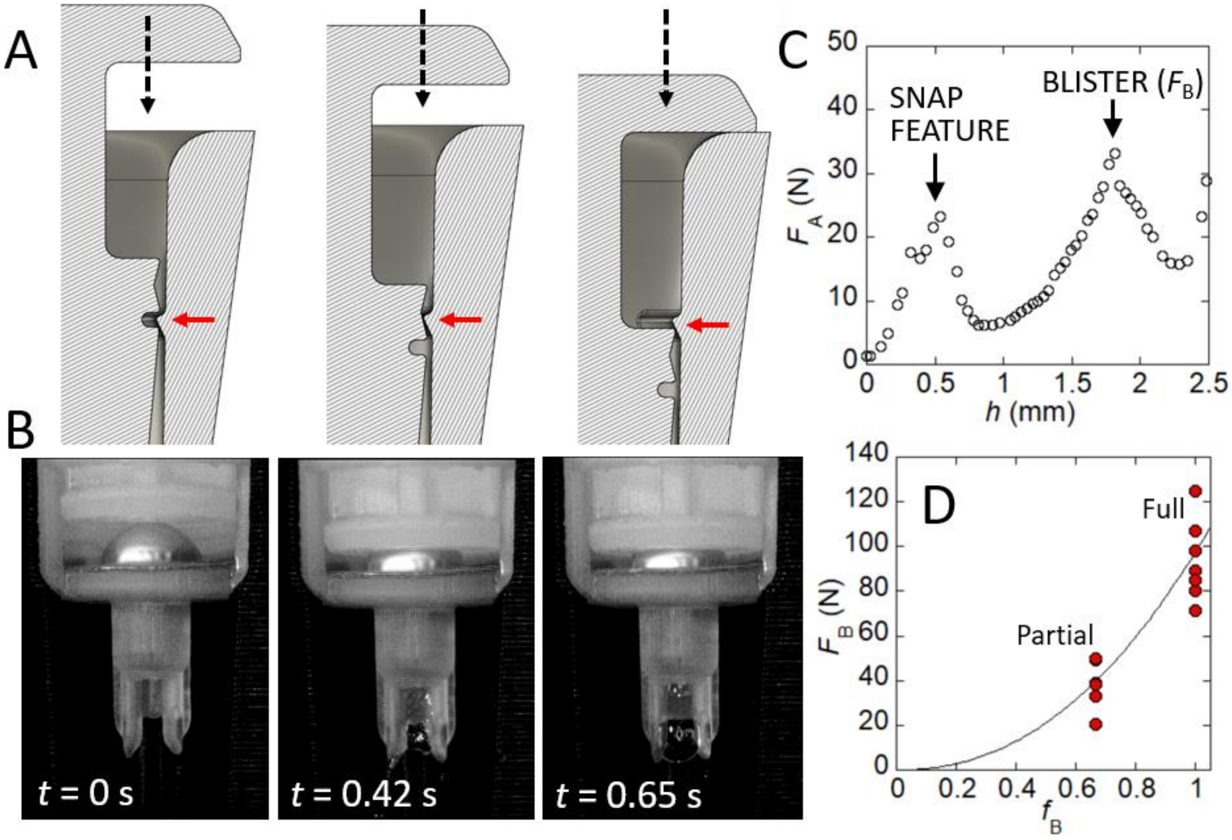

Figure 7.4. Blister compression forces and dynamics. (A) Series of illustrations depicting position of snap features inside plunger and syringe tube during depression of plunger. Red arrows indicate the position of the internal snap ring. (B) Series of high-speed images depict plunger depression, blister compression, and expulsion of blister liquid. (C) Representative measurement of force required to depress the syringe plunger, FA as a function of plunger displacement, h. (D) Force required to compress a 130 μL blister in the device, FB plotted as a function of blister compression fraction, f_B. Curve is a fit to $F_B = 97.549 f_B^{2.2092}$.

We plot the distribution of F_B as a function of blister compression distance given our chosen partial compression compared to full compression of a blister (Figure 7.4E). There is a squared relationship between blister compression distance (normalized by the blister height) and the force required to actuate the blister, which indicates that a partial compression is much easier for the user than a full compression. Since the blister is pierced in both cases, we assume the greater force in the full compression is coming from the structural element of the blister dome and thus would be present even if the blister were not completely filled with water (as was observed anecdotally with half-filled blisters).

We test our device using a common RT-LAMP formulation to show that it successfully captures the accurate amount of saliva, punctures the water-filled blister, delivers the water and saliva to the vial, and adequately mixes the water, saliva, and lyophilized reagents in the vial. Then we place the device in a dry bath vial heater at 65° C for 30 minutes. We use saliva that has been spiked with synthetic viral RNA. We lyophilize the LAMP reagents in individual PCR vials using a lyophilizer. The sample that did not have viral RNA does not show an increased fluorescence (Figure 7.5 i) whereas the sample spiked with viral RNA exhibits increased fluorescence (Figure 7.5 ii).

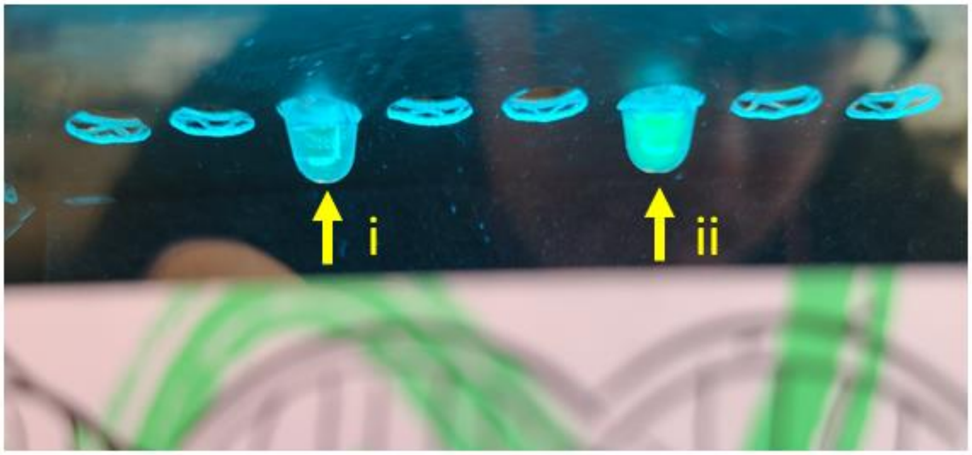

Figure 7.5. Device validation. The sample with no viral RNA present (i) exhibits less fluorescence intensity than the sample with viral RNA present (ii). Both samples were heated at 65° C for 30 minutes. The injection moldable design facilitates easy scale-up and is designed to work with swabs and vials that already exist on the market. The test requires only a simple, inexpensive processing system that allows the test to be set up in a variety of institutions at low cost.

Conclusion

Here, we describe a low-cost, hand-held, manually operated device for point-of-care molecular pathogen detection. The device consists of an upper syringe-type assembly containing a plunger and a liquid-filled blister pack, as well as a microcentrifuge tube containing lyophilized reagents. Key features include a two-pronged fork geometry that precisely transfers small volumes of saliva from flocked collection swabs and a plunger that delivers exact reagent volumes while providing tactile feedback to the user. We identify an optimal fork gap distance of 1.7 mm, which balances ease of use with consistent saliva transfer. Force measurements confirm that partial blister compression requires minimal effort, making the device easy to operate for users without specialized training. This device presents as a promising solution for widespread, accessible diagnostic testing, particularly in low-resource settings where rapid, accurate, and cost-effective pathogen detection is needed.

Methods

Fabrication

Devices were fabricated using a FormLabs 3D printer (Form 2) and FormLabs resin (Durable). Durable resin was chosen for its mechanical properties, which are similar to polypropylene, a polymer commonly used for injection molded diagnostic devices. Devices were cured in a FormLabs curing station (Form Cure) for 2 h following fabrication to ensure that the internal spike features were rigid enough to pierce the underside of the blister. Other materials included capless polypropylene microcentrifuge tubes (Sarstedt, 0.5 mL, 72.698.200), diagnostic reagent blisters (J-Pac Medical, 135 uL), and PCR sealing film (Southern Labware, P1001-Q). Lyobeads were produced by Evik Diagnostics.

Assay Formulation

For each reaction vial, the following LAMP formulation components were freeze dried using a commercial freeze-drier (Millrock LD85). Warm Start 2x Master Mix (12 uL, NEB), dUTP (0.175 uL), UDG (0.5 uL), SYTO 82 (0.5 uL, 25 uM solution; Invitrogen SYTO-9 Green Fluorescent Nucleic Acid Stain, cat no. S34854), nuclease free water (4.325 uL, NEB), 10x primers (2.5 uL), SARS-CoV-2 E-gene (10^5 c/uL, 2 uL).

Force Measurements

Partial blister compression measurements were performed using the normal force transducer on a mechanical rheometer (TA Instruments, AR-G2). The device was held vertically upright in a 3D printed holder which was centered on the lower plate of the rheometer. The normal force transducer was tared, and the upper plate of the rheometer lowered to contact the top of the plunger. To actuate the device and compress the blister, the upper plate was lowered 2.8 mm at a rate between 100 µm/s and 500 µm/s.

Full blister compression measurements were performed on an electronic scale (W-8250-50BS, Accuteck). A 3D printed holder was used to hold the device vertically, which was centered on the scale. The scale was tared and the device actuated manually by hand. The force required to actuate the device was read by eye.

Design Considerations

General considerations: The asymmetric fork geometry with a “trough” for saliva collection was designed to avoid trapping and compressing air in the channel between saliva and the blister pack. This design allows for consistent collection of saliva volumes (10-20 μl).

Injection molding considerations: Wall thickness was kept as uniform as possible throughout the device to achieve proper plastic flow and packing during injection molding. Corners were rounded to standards[288] for injection molding for polypropylene, about 0.5 to 1.5 times the adjacent wall thickness. Snap features in the plunger and tube were designed with mold construction and device demolding in mind. Pinch points in the design that could restrict plastic flow were avoided.

Ease-of-use considerations: The device was designed for the average adult hand. The average adult hand width[289] is 8.4 cm and the syringe portion of the device is 5.3 cm tall, which we found to be easily graspable by the average adult hand. The device was also designed so that plunger actuation can easily be performed by hand and provides tactile feedback. The average adult can easily exert 20-45 N using their thumb, which we achieved by designing partial compression of the blister. Snap features were added to provide tactile feedback to the user. The user does not experience two noticeable force maxima (Figure 7.4D), but only feels the initial click of the snap features as the plunger moves past the snap ring in the tube. This is because the force required to overcome the first force peak is significant enough that the resulting momentum punctures and compresses the blister without any additional noticeable force. The minimum sample and blister liquid volumes were chosen based on the amount of total liquid visible to the user after expression from the blister. This provides additional confirmation to the user that the device has been successfully actuated. Additionally, we considered the minimum saliva volume that could be repeatedly transferred from the swab to device; too little saliva could result in a false negative.

CHAPTER EIGHT

HIGH-THROUGHPUT DIAGNOSTIC WORKFLOW FOR EMERGING INFECTIOUS DISEASES USING RT-LAMP AND AUTOMATED FLUORESCENCE DETECTION

Contribution of Authors and Co-Authors

Manuscript in Chapter 8

Author: Isaak Thornton Contributions: Technology development, experimental execution, data analysis, manuscript writing, and editing.

Co-Author: Dimitri A. Bikos Contributions: Technology development, biochemistry, experimental execution, manuscript writing, and editing.

Co-Author: Thomas B. LeFevre Contributions: Technology development, manuscript editing.

Co-Author: David A. Weitz Contributions: Research supervision, conceptualization, funding acquisition.

Co-Author: Connie B. Chang Contributions: Research supervision, conceptualization, funding acquisition.

Co-Author: Peter R. Lu Contributions: Research supervision, conceptualization, programing, experimentation, data analysis, manuscript writing, and editing.

Co-Author: James N. Wilking Contributions: Research supervision, conceptualization, funding acquisition, and manuscript writing and editing.

Manuscript Information

Title: High-Throughput Diagnostic Workflow for Emerging Infectious Diseases Using RT-LAMP and Automated Fluorescence Detection

Authors: Isaak Thornton[1,3], Dimitri A. Bikos[2,3], Thomas B. LeFevre[2,3], David A. Weitz[4,5,6], Connie B. Chang[7], Peter J. Lu*, and James N. Wilking[7]*

[1]Department of Mechanical and Industrial Engineering,
[2]Department of Chemical and Biological Engineering,
[3]Center for Biofilm Engineering,
Montana State University, Bozeman, MT, USA
[4]John A. Paulson School of Engineering and Applied Sciences, Harvard University, Cambridge, MA, USA
[5]Department of Physics, Harvard University, Cambridge, MA, USA; and
[6]Wyss Institute for Biologically Inspired Engineering, Harvard University, Boston, MA, USA
[7]Department of Physiology and Biomedical Engineering, Mayo Clinic, Rochester, MN

*Corresponding authors

Status of Manuscript:
☒ Prepared for submission to a peer-reviewed journal
☐ Officially submitted to a peer-reviewed journal
☐ Accepted by a peer-reviewed journal
☐ Published in a peer-reviewed journal

Abstract

Emerging infectious diseases pose significant risks to global human health, particularly during the early stages of an outbreak when vaccines are unavailable, and herd immunity is absent. Rapid and accessible diagnostics can play a crucial role in managing outbreaks by enabling timely identification of cases, informing patient care, and supporting effective public health interventions. However, current diagnostic methods have limitations. Polymerase Chain Reaction (PCR), the current gold standard, is highly sensitive but requires specialized equipment and infrastructure, limiting its testing capacity and access. Rapid antigen tests are cost effective and provide fast results but are typically less sensitive and require many months to develop. To address these limitations, we present a diagnostic workflow designed for rapid, high-throughput testing during outbreaks of emerging infectious diseases. Our workflow integrates reverse transcription loop-mediated isothermal amplification (RT-LAMP), sequence-dependent fluorescent probes, and a custom 3D printed far-field fluorescence detector with automated result readout. This system achieves nucleic acid amplification without thermocycling and provides high-throughput fluorescent measurement, capable of processing over 2,000 tests per hour. We demonstrate the amplification and detection of viral RNA from SARS-CoV-2, Zika virus, and Influenza B virus (IBV). Additionally, we demonstrate diagnostic multiplexing capabilities through the simultaneous detection of IBV and SARS-CoV-2 within the same test. Finally, we show the feasibility of using a low-cost incubating water bath, demonstrating the potential for deploying isothermal amplification in resource-limited settings. This work demonstrates how existing technologies, such as isothermal amplification and fluorescence detection, can be integrated into new diagnostic methods that address current limitations, providing scalable and

adaptable solutions for rapid, high-throughput diagnostic response to emerging infectious disease outbreaks.

Introduction

Emerging infectious diseases continue to pose significant risks to global human health. These diseases, which can be caused by viruses, bacteria, and other disease causing agents, are becoming more common as factors such as wildlife encroachment, climate change, and global interconnectivity increase the likelihood of outbreaks[177,181]. At the onset of an emergent disease outbreak, when vaccines are not yet available and herd immunity is absent, options for controlling disease spread are limited[185,186]. In this context, medical diagnostics can play a critical role in identifying infections, informing patient care, and providing tools for tracking disease spread [193]. However, the effectiveness of existing diagnostic methods during outbreaks of emergent diseases is often limited by lengthy development times and challenges associated with their deployment and widespread accessibility[190,205,290].

Polymerase chain reaction (PCR) is the current gold standard method for diagnostic detection of infections[206]. These nucleic acid amplification tests (NAATs) utilize short nucleic acid sequences, known as primers, to selectively amplify targeted pathogen nucleic acid sequences[207]. Researchers use computational tools to select target sequences and design PCR tests based on a pathogen's genome within days. For example, a PCR-based diagnostic for SARS-CoV-2 was created within three weeks of obtaining the virus's genome, providing a critical tool for monitoring the virus's initial spread[199]. While quick to develop, PCR testing requires well-equipped laboratories, trained personnel, and specialized thermocycling equipment. A typical PCR procedure requires multiple sample preparation steps followed by a thermocycling incubation process involving 75-135 precise temperature changes, typically requiring several hours to run each sample batch[200]. These process requirements make PCR-based testing time-consuming, costly, and challenging to deploy at scale, particularly in resource limited settings[190,205,290].

Lateral flow rapid antigen tests provide simple, low-cost, and decentralized diagnostic options. Antigen based tests utilize antibodies to detect pathogen associated material (e.g. viral proteins) in a patient sample without the need for amplification, enabling self-administered testing without specialized lab equipment. Despite their accessibility, the development of these tests is time-intensive, often requiring several months to identify suitable antibodies[217]. The first rapid antigen test approved by the US FDA for SARS-CoV-2 was not available until nearly a year after virus identification, highlighting their limited utility as tools for emergent disease response[217,233]. Moreover, studies conducted during the COVID-19 pandemic indicate that more than one-third of antigen tests administered to infected patients produced false negative results when compared to PCR-based diagnostics, revealing a significant limitation in the sensitivity of these tests[230]. Given the limitations of current diagnostics related to infrastructure, time, cost, and sensitivity, there is a pressing need for diagnostic methods that can be developed quickly and deployed widely in the early stages of future outbreaks.

Isothermal NAATs, such as loop mediated isothermal amplification (LAMP), offer several advantages for addressing current diagnostic needs. Like PCR, LAMP-based diagnostics use primers that can be designed quickly based on a pathogen's genome[224]. Unlike PCR, LAMP operates at constant temperature, removing the need for thermocycling machines and enabling incubation with simple heating devices like heat blocks, thermal water baths, and ovens[237–240].

Moreover, LAMP diagnostics can be performed in a single reaction with minimal sample preparation, reducing the need for technician handling[246].

When combined with fluorescent labeling, NAATs allow for readout using fluorescence detection[241]. Sequence-dependent fluorescent reporters, such as QUASR, employ dye-labeled primers that integrate into the amplified DNA during incubation. Incorporated QUASR probes are fluorescent while unincorporated probes are quenched, reducing background fluorescence and improving the signal-to-noise ratio when compared to dyes common to NAATs like SYTO or SYBR Green. Moreover, several traditional NAAT dyes inhibit the amplification reaction, therefore, reaction chambers must be opened following amplification to add the dye, adding an additional processing step and increasing the risk of contamination. QUASR probes do not inhibit LAMP reactions, allowing for direct measurement of fluorescence following incubation without additional processing. Additionally, the sequence dependence of QUASR allows for the detection of multiple targets within a single reaction, enabling diagnostic multiplexing[241,245]. Despite the current capabilities of both LAMP based diagnostics and sequence-dependent fluorescent probes, applications of isothermal amplification for population-scale, high-throughput testing remain limited.

Here we present a diagnostic workflow designed for high-throughput testing during outbreaks of emerging infectious diseases. We utilize RT-LAMP for isothermal amplification of viral RNA sequences. We employ accessible heating devices, such as block heaters and thermal water baths, for incubation. Results of amplification are indicated by sequence-dependent fluorescent probes. To quantify fluorescence signals and determine diagnostic outcomes, we design and fabricate a far-field fluorescence detector. To improve detection throughput, we implement an automated rapid serial detection system capable of processing over 2,000 samples per hour. Using this system, we demonstrate detection of viral RNA from three distinct pathogens, SARS-CoV-2, Zika virus, and influenza B virus. Furthermore, we demonstrate diagnostic multiplexing by detecting two disparate viral RNA sequences within the same sample using two independent fluorescent channels.

Experimental

We prepare RNA positive and negative samples using extracted SARS-CoV-2 RNA (see Methods). We follow a "one-pot" RT-LAMP protocol, combining all assay reagents, fluorescent probes, and extracted RNA in a single reaction vessel (i.e. microcentrifuge tube)[246]. We incubate the prepared samples in a dry block heater for 30 minutes at 65°C for assay amplification (Figure 8.1).

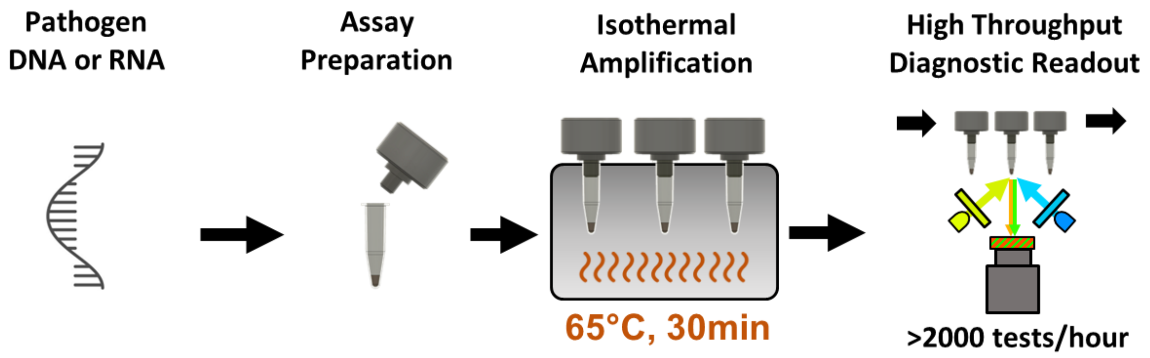

Figure 8.1. LAMP isothermal amplification and rapid serial detection workflow. Isothermal amplification enables diagnostic testing platforms with low-cost and high throughput. The combination simple sample collection, assay preparation, isothermal heating, and rapid serial detection offers diagnostic capabilities for community level testing not currently available.

Following incubation, we remove the samples from the heater and allow them to cool to ambient temperature. QUASR fluorescent quenching is temperature dependent, therefore the cooling step is crucial to the final fluorescent signal[245]. The fluorescent signal from the incorporated probes increases with the quantity of amplified DNA. To reduce variations in detected fluorescence intensity due to several practical factors, such as reaction vessel manufacturing variations, evaporation, or heating fluctuations, we include 6-carboxy-X-rhodamine (ROX) as a passive reference dye. ROX provides a consistent fluorescent signal that remains stable throughout the amplification process, allowing for normalization of non-amplification related fluctuations in fluorescence[291].

Fluorescence Detector

To measure end-point sample fluorescence, we design and build a two-channel fluorescence detector. The detector employs two sets of light-emitting diodes (LEDs) with bandpass filters to selectively illuminate the samples at the excitation wavelengths specific to each dye (Figure 8.2A). A monochromatic camera equipped with a dual bandpass emission filter captures the fluorescent emissions from the sample (see Methods). To independently measure the two fluorescence channels, we alternate LED illumination, capturing images of the reporter and reference fluorescence sequentially with the same camera (Figure 8.2B). A single board computer and a microcontroller LED illumination, image acquisition, and image processing.

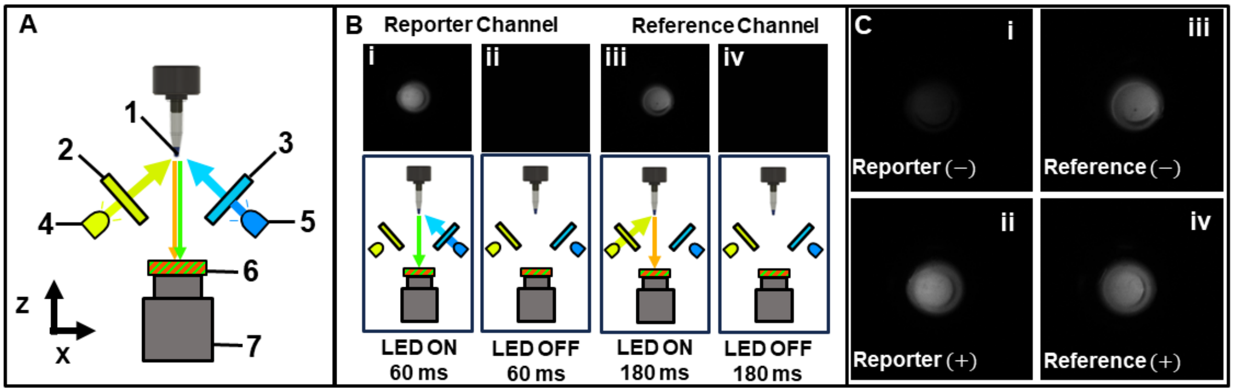

Figure 8.2. Far field optical fluorescence measurement of RT-LAMP assay with two fluorescent channels. (A) Schematic depicting the components of the detector optical system. The sample volume (1) is illuminated by two LEDs (4,5) and two excitation filters (2,3). The LEDs are triggered individually, exciting both fluorophores independently. A dual bandpass filter (6) separates and a monochromatic camera (7) captures the fluorescence emission for both channels. (B) Representative images of both the reporter fluorescence as illuminated by the blue LED (i, ii) and the reference sample fluorescence as illuminated by the yellow LED (iii, iv). Images i and iii represent a RNA-negative sample while images ii and iv display images of a RNA-positive sample. (C) Imaging routine for fluorescent measurement. LEDs illumination is alternated for: (i) reporter fluorescence, (ii) reporter background, (iii) reference fluorescence, and (iv) reference background.

We position the sample volume within the illumination path of the LEDs and the camera’s field of view (FOV) as depicted in Figure 8.2A. For each sample, we capture images in two channels to independently measure the reporter and reference fluorescence signals. For each channel, we acquire one image with the LED on to record sample fluorescence and one with the LED off to obtain a background measurement for subtraction (Figure 8.2B). We adjust the camera’s exposure time and gain for each channel, capturing the reporter fluorescence in 60 ms and the reference fluorescence in 180 ms. Representative fluorescence images for both a positive and negative sample are shown in Figure 8.2C. We calculate overall fluorescence values for each channel by summing the individual pixel values across the entire image. We divide the sum of the reporter fluorescence by the sum of the reference fluorescence to yield a normalized endpoint fluorescence measurement which we refer to as the fluorescence ratio.

High Throughput Detection

To facilitate high-throughput fluorescence readout, we develop an automated system to position samples within the optical path in rapid succession. Although far-field fluorescence measurements take <1 s per sample, manually positioning the samples within the FOV by technicians is time-consuming, requiring a minimum of at least several seconds per sample to align, initiate the fluorescence measurement, and remove the sample from the detector. To improve throughput, we implement a rotary carousel driven by a stepper motor, enabling rapid and precise rotation of samples into and out of the optical path as depicted in Figure 8.3C.

The carousel operates by accepting samples at the inlet and advancing them through discrete steps to the camera’s FOV for imaging (Figure 8.3C). We load devices into the carousel using cartridges, which enables efficient handling of up to six samples at a time (Figure 8.3). We angle the inlet and outlet at 25 degrees to facilitate gravity-driven movement of samples into and out of the carousel. As the carousel rotates, each sample advances sequentially to the next position. When a sample reaches the third position, it is aligned within the camera's FOV as depicted in Figure 8.3. The carousel pauses to allow for fluorescence imaging of both the reporter and the reference dyes. Following imaging, the carousel rotates again, moving the imaged sample out of the FOV and advancing the next sample into position for imaging.

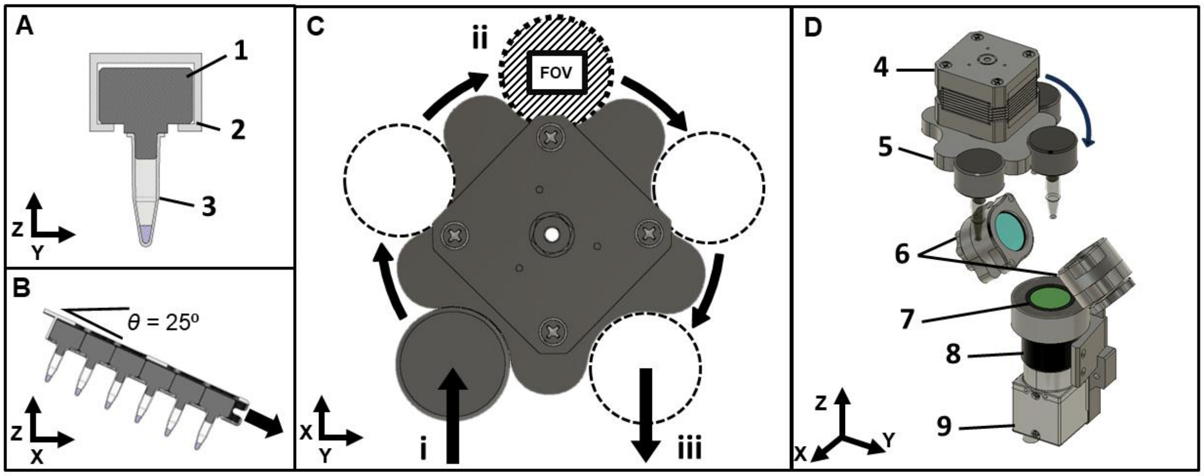

Figure 8.3. Schematics and renderings of active device positioning system for high throughput fluorescence measurement. (A) Cross sectional render of device body (1), device guiding track (2), and reaction chamber (3). (B) Cross sectional render of devices loaded into inlet chute. The inlet is angled at 25 degrees to allow gravity driven motion of the devices along a confined path. (C) Schematic of active positioning carousel with five sample positions. Devices enter the carousel at the inlet (i) and are advanced in discrete 1/5 rotations of the carousel. The measurement position (ii) places the reaction chamber within the optical path of the camera and excitation LEDs. Following imaging, the device is advanced two more steps to the final position (iii) where it exits the detector. Each discrete rotational step and measurement routine takes less than two seconds combined (D) Rendering of carousel and optical system assemblies. A stepper motor (4) drives the carousel (5) with precise rotation, positioning samples within the optical system's field of view. Two excitation LED and filter assemblies (6) are used to illuminate the sample independently. A dual bandpass emission filter (7) blocks non-fluorescent light from the sample. A camera lens (8) focuses light onto the monochromatic camera's (9) sensor.

The single board computer synchronizes carousel rotation, LED illumination, and camera exposure. A microcontroller and a stepper motor driver manages the stepper motor rotation, ensuring accurate and efficient sample movement. For the described carousel, we determine that an acceleration of 6.25 rev/s^2 provides smooth and reliable motion. This acceleration rate effectively balances the motor's torque capabilities with the system's friction and inertia, providing rapid positioning without compromising accuracy. Accelerations above this value result in motor stall or loss of steps, causing unreliable positioning of the samples within the

FOV. Including rotation and imaging time, the total cycle time per device is approximately ≈1.7 s as calculated by the average detector run-time required to process 960 sample measurements.

Sous Vide Heating

To demonstrate a low-cost and accessible method for sample incubation, we assemble a thermal bath using a sous vide circulating heater and a bucket of water. We place the reaction vessels in a floating tube rack and submerge the sample volumes in the heated water, ensuring consistent thermal contact. The large thermal mass of the water mitigates thermal fluctuations. We incubate the samples for 30 min at 65°C similar to incubation with the standard laboratory dry block heater.

IBV and ZIKV Assays

To expand the scope of our diagnostic workflow, we develop additional RT-LAMP assays for Influenza B (IBV) and Zika virus (ZIKV), following the same methodology used for SARS-CoV-2 detection. Using published genomic sequences, we design RT-LAMP primers and QUASR fluorescent probes specific to IBV and ZIKV respectively (see Methods). The procedure for sample preparation, incubation, and fluorescence detection remains unchanged.

Multiplexing

To demonstrate further capabilities of the RT-LAMP amplification process and the sequence dependence of QUASR probes, we develop a multiplex diagnostic test capable of simultaneously detecting SARS-CoV-2 and IBV RNA within a single reaction. We combine RT-LAMP primers and QUASR probes for both pathogens within the same test. Two orthogonal QUASR fluorescent probes provide independent fluorescent signals: a green fluorophore to indicate SARS-CoV-2 and a red fluorophore to indicate IBV, allowing for simultaneous detection. To measure the multiplex test fluorescence, we repurpose the fluorescence channel originally used for the reference dye (ROX) to detect the red fluorophore associated with IBV amplification. We adjust the gain and exposure settings for the detection of the IBV QUASR fluorescence. Following a similar imaging routine, we capture images for each channel and perform background subtraction to independently quantify fluorescence signals for both pathogens.

Results

Fluorescence Detection of SARS-CoV-2 Nucleic Acid Amplification

Discriminating between positive and negative tests relies on accurate measurement of fluorescence following sample incubation. The reporter dye (QUASR) fluorescence indicates amplification of the target RNA, while the reference probe (ROX) fluorescence provides a stable fluorescent signal that is used to correct for any variations unrelated to amplification. To observe the development of both fluorescent signals with amplification, we conduct incubation time-series experiments on the RT-LAMP assay using synthetic SARS-CoV-2 RNA samples. We prepare both RNA positive and RNA negative samples within microcentrifuge tubes and vary sample incubation times from 0 to 45 min to observe the progression of fluorescence signals. In RNA-positive samples, the reporter fluorescence begins to increase noticeably after 15 min, reaching a peak with a nearly fourfold increase in fluorescence pixel sum after approximately 30 min as shown in blue in Figure 8.4A. The reference fluorescence remains stable throughout the incubation period, confirming fluorescence independence from amplification. In contrast, RNA-negative samples show no significant increase in reporter fluorescence over time, indicating the absence of non-specific amplification (Figure 8.4A).

Keeping the incubation time consistent at 30 min, we compare 24 SARS-CoV-2 assays comprising 12 RNA-positive and 12 RNA-negative samples. The raw end-point fluorescence measurements display distinct separation between positive and negative samples along the reporter fluorescence axis (Figure 8.4B). After normalizing the reporter fluorescence to the reference fluorescence, the mean fluorescence ratio values are separated by more than five standard deviations (Figure 8.4C). The fluorescence ratios in negative samples remain low (0.3 ± 0.03), indicating effective fluorescence quenching and minimal background signal.

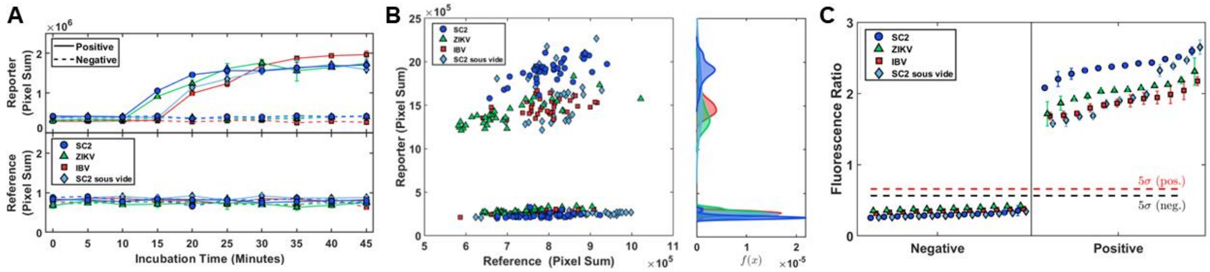

Figure 8.4. Fluorescence detection of nucleic acid amplification. (A) Time evolution of fluorescence pixel sums with sample incubation of RT-LAMP assays. The upper panel displays the reporter fluorescence pixel sum, providing indication of amplification, while the lower panel displays the reference fluorescence pixel sums. (B) Raw fluorescence pixel sums of both the reference signal (x-axis, ROX) and reporter signal (y-axis, QUASR) for four viral assays (○ - SARS-CoV-2, △ - ZIKA, and ■– IBV, ◊SARS-CoV-2- Sous Vide). Two groups are clearly separated along the y-axis, demonstrating clear grouping of RNA-positive and RNA-negative sample fluorescence measurements. A histogram depicts the frequency distribution of reporter fluorescence measurements. (C) Normalized fluorescence measurements depicting the ratio of reporter fluorescence pixel sum to reference fluorescence pixel sum. Thresholds for both positive and negative values show five standard deviations from the positive and negative group means.

Generalizability to Multiple Pathogens

A significant strength of nucleic acid-based diagnostics is the ability to adapt the assay to virtually any pathogen by targeting DNA or RNA sequences specific to the pathogen. To demonstrate the generalizability of our RT-LAMP assay and fluorescence detection system, we generate two additional assays to ZIKV and IBV RNA sequences respectively.

Time-series fluorescence measurements for RNA-positive samples of ZIKV and IBV show similar amplification kinetics to those observed for SARS-CoV-2, with increases in reporter fluorescence corresponding to successful nucleic acid amplification as depicted in green and red markers for ZIKV and IBV in figure 8.4A respectively. In end-point assays, both ZIKV and IBV RNA-positive samples exhibit significantly higher reporter fluorescence compared to RNA-negative controls, with separation between positive and negative groups exceeding five standard deviations (Figure 8.4C). Low fluorescence ratio values in negative samples across all pathogens suggest high specificity of the assays and no off-target amplification.

Low-Cost Incubation Using Sous Vide Heating

Recognizing the importance of accessible incubation methods for isothermal amplification, we evaluate the use of a low-cost sous vide heater for sample incubation. SARS-CoV-2 assays incubated using the sous vide thermal bath display fluorescence signals comparable to those incubated with a standard dry block heater as depicted by the light blue markers in Figures 4B and 4C. While the variability in endpoint fluorescence of positive samples increases slightly with the sous vide method (standard deviation of 0.36 versus 0.14 for the dry block heater), the separation between positive and negative sample means remains greater than five standard deviations.

Multiplex Detection of SARS-CoV-2 and IBV

Multiplex diagnostics offer significant advantages by enabling the simultaneous detection of multiple pathogens, improving efficiency and reducing the need for separate tests. This approach is valuable in situations where non-specific symptoms may complicate diagnosis. To assess the potential for multiplex detection, we develop an RT-LAMP assay targeting both SARS-CoV-2 and IBV within a single reaction. Using two orthogonal QUASR fluorescent probes emitting at different wavelengths, we successfully detect both viral RNAs independently. The fluorescence measurements reveal four distinct clusters corresponding to the four possible combinations of RNA-positive and RNA-negative samples for the two viruses (Figure 8.5A). The separation between positive and negative samples for both SARS-CoV-2 and IBV exceeds four standard deviations, confirming the assay's ability to accurately identify each pathogen without cross-interference.

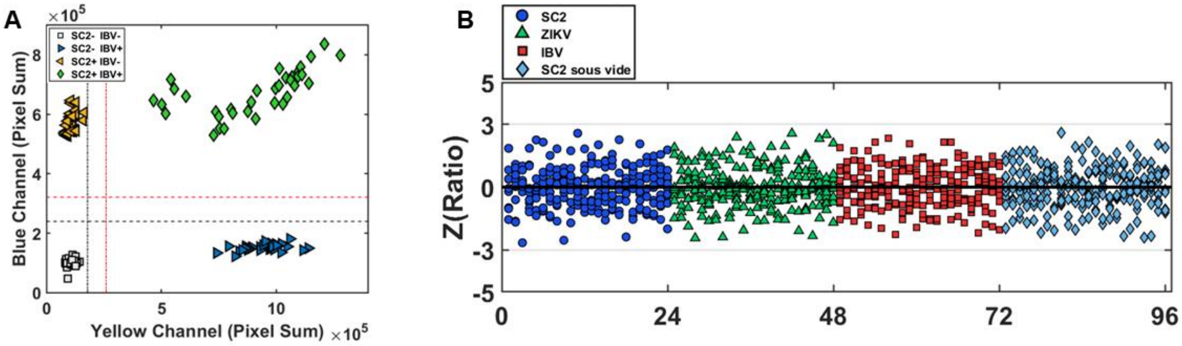

Figure 8.5. Multiplex diagnostic dual channel fluorescence and high throughput detection results. (A) Raw fluorescence pixel sums of both the yellow fluorescence channel (x-axis, IBV-QUASR) and blue fluorescence channel (y-axis, SARS-CoV-2-QUASR) for 48 samples including all permutations of RNA-negative and RNA-positive samples of SARS-CoV-2/IBV samples. Four groups representing the four permutations are clearly separated. Threshold lines indicate four standard deviations from the negative (black) sample and positive (red) sample means for both SARS-CoV-2 (dashed line) and IBV (dotted line) sample sets. (B) High throughput measurement of 96 RT-LAMP assays. Each sample was measured 10 times for a total of 960 measurements. Run time was just over 27 min for a rate of detection > 2,100 samples per hour. The Z-score

based on the fluorescence ratio for each sample is shown. All normalized fluorescent measurements fall within three standard deviations of the mean.

High-Throughput Fluorescence Measurement

High-throughput diagnostic systems are essential for large-scale testing, particularly during outbreaks of emergent diseases, where timely and accurate detection is critical. Efficient processing without compromising measurement accuracy ensures that such systems can meet the demands of population scale testing. To assess the throughput and consistency of our detection system, we conduct rapid serial fluorescence detection on 96 RT-LAMP assays, each measured ten times, resulting in 960 measurements in under 28 min. This corresponds to a detection rate of approximately 2,100 samples per hour. The calculated Z-scores for each sample fell within three standard deviations of the group means, demonstrating excellent repeatability and reliability (Figure 8.5B). These high-throughput capabilities, combined with the assay's sensitivity and specificity, position the diagnostic platform as a valuable option for large-scale testing during infectious disease outbreaks.

Discussion

The proposed diagnostic workflow addresses some of the limitations of current testing methods by integrating isothermal amplification, sequence-specific fluorescent probes, and automated fluorescence detection for high-throughput testing during infectious disease outbreaks. Key to this workflow is RT-LAMP, an isothermal amplification technique that eliminates the need for complex thermocycling equipment traditionally required for PCR-based diagnostics. RT-LAMP allows for rapid nucleic acid amplification at a constant temperature, significantly reducing the time and complexity of sample incubation. To facilitate the use of isothermal amplification tests in areas with limited laboratory infrastructure, we demonstrate a low-cost incubation method using a sous vide heater. This accessible approach demonstrates that effective nucleic acid amplification is achievable without specialized equipment, expanding the potential for deployment in resource-constrained environments.

To complement the amplification process, we design and build a custom fluorescence detection system that provides assay-specific, multi-wavelength measurements for diagnostic determination. We integrate automated sample positioning into the detector to improve throughput compared to manual sample handling. With this automated setup, we achieve a detection rate of over 2,100 tests per hour-- a critical feature of the proposed system for increasing diagnostic throughput during pathogen outbreaks.

In agreement with previous studies that emphasize the importance of early deployment of diagnostic tools during outbreaks, the proposed workflow is adaptable to any pathogen nucleic acid sequence, including SARS-CoV-2, ZIKV, and IBV, demonstrating the flexibility of the assay and detector system. This adaptability is crucial for responding to novel or emerging pathogens, allowing for rapid development and deployment of diagnostic tools with minimal delay. Additionally, the use of sequence specific fluorescent probes enables multiplexed diagnostics, where multiple pathogens or pathogen strains can be detected simultaneously within a single sample, as we demonstrate with the simultaneous detection of SARS-CoV-2 and IBV within a single reaction. Multiplexing significantly enhances diagnostic efficiency, particularly in clinical scenarios where symptoms are non-specific. This capability can reduce the need for multiple tests, thereby conserving valuable resources.

To further improve the applicability and efficiency of this diagnostic workflow, several opportunities for future work exist. One such opportunity is the exploration of different incubation techniques. For instance, conveyor belt ovens or water baths could enable continuous isothermal amplification and detection, allowing for automated transitions from incubation to detection. Scalability and adaptability are crucial for the broader impact of this workflow. Decentralized diagnostic hubs or mobile testing units, supported by field deployable systems, could extend testing to larger populations, particularly in rural or hard-to-reach areas. Automated sample handling could further reduce training requirements, making the workflow accessible to minimally trained health workers and supporting early detection during outbreaks.

Ensuring a robust supply chain for necessary materials is also crucial during global crises. Decentralized manufacturing, including on-demand 3D printing of diagnostic components, could enhance resilience by enabling rapid local production and reducing reliance on global distribution networks. Open-source dissemination of device designs, protocols, and software would further support local production. Integration of digital health platforms for real-time data transmission could further enhance surveillance and outbreak management, providing timely information for decision-making and improving response efforts.

Ultimately, the rapid deployment of a diagnostic system that does not require centralized laboratories can bridge the gap between diagnostic capability and limited infrastructure during future pandemics. Developing methods to improve throughput, adaptability, and accessibility will enhance the overall effectiveness of this diagnostic workflow, allowing it to meet the demands of large-scale testing during outbreaks. Strengthening access to sensitive and rapid diagnostic tests will be crucial for addressing future pandemics, reducing response times, and improving global preparedness for emerging infectious diseases.

Materials and Methods

Primer and Probe Design

RT-LAMP primers for SARS-CoV-2, IBV, and ZIKV were adapted from published designs targeting conserved genomic regions including: the N-gene of SARS-CoV-2[292], the NS1 gene of IBV[293], and the NS5 gene of ZIKV[294]. Primers were synthesized by Integrated DNA Technologies (Coralville, IA, USA) and resuspended in molecular grade H2O (NEB B1500) to a final concentration of 100 μM.

RNA Standards

SARS-CoV-2 quantitative RNA standards are RGTM 10169 Fragment 1 (NIST, Applied Genetics Group) a synthetic RNA fragment of total length 3985 nt, including SARS-CoV-2 sequence: 25949-29698 of isolate USA-WA1/2020 which includes E, M, and N genes and orfs 3a, 6, 7a, 8, and 10. The concentration is 5x106 c/uL.

IBV and ZIKV quantitative RNA standards come from Virome Nucleic Acid Mix MSA-1008 (ATCC) which is comprised of six extracted genomic viral RNAs, including Influenza B virus B/Florida/4/2006 (ATCC VR-1804DQ) and Zika virus (ATCC VR-1838DQ). ATCC estimated concentration 2x104 c/uL +/- 1 log.

QUASR RT-LAMP reactions

RNA-positive controls were prepared by using 5 μL of either the NIST SARS-CoV-2 standard or the ATCC Virome Nucleic Acid Mix in each RT-LAMP reaction. Reactions were set up in 0.5 mL polypropylene microcentrifuge tubes (72.698.200, Sarstedt, Germany) and contained 12.5 µL of WarmStart® Colorimetric LAMP 2X Master Mix (New England Biolabs), 2.5 µL of a pre-prepared primer mix, 0.5 µL of a QUASR fluorescent probe, 0.5 µL of ROX reference dye for normalization, and 5 µL of RNA sample, making up a total volume of 25 µL. Reactions are heated in 0.5-mL drilled aluminum blocks heated in a digital dry bath (Globe Scientific Inc, AS-BSH2-1473). Temperatures are monitored using thermocouple (AZ Instrument Corp., 88598 4ch K SD Logger) and analog thermometer (Thermco Products, 3 16 076) and (PSI 31495C USA).

RT-qPCR of quantitative standards

Standard curves are prepared using 20-uL reactions comprised of 5 uL Luna Probe One-Step RT-qPCR 4X Master Mix with UDG (NEB M3019S), 0.8 uL 10 uM forward and reverse primers, 1 uL of 25-uM SYTO-9 green fluorescent nucleic acid stain (Invitrogen S34854), 5 uL of quantitative standard, and 8.2 uL molecular grade H2O (NEB B1500).

Instrumentation

A far-field fluorescence detector was assembled from commercially available components. The detector structure was entirely 3D printed (PETG, Prusa MK3S+) including housings for the LEDs and optical filters. Heat set threaded inserts (97163A149, McMaster) and M3 machine screws were used as fasteners for assembly.

The optical system incorporates two narrow bandwidth LEDs (LED465E and LED570L, Thorlabs) to excite the fluorophores of the QUASR probes (493 nm) and ROX (578 nm). Excitation light is filtered by bandpass filters specific to each fluorophore, filtering to 480 nm for the reporter signal and 570 nm for the reference signal respectively (FB480-10 and FB570-10, Thorlabs). Emitted light passes through a dual bandpass filter (511.5/2, 630.5/3 Dual BP; Alluxa) and is focused onto the sensor of a monochromatic camera (0.4MP, BFS-U3-04S2M-CS ,FLIR) using a 16 mm lens (CS2316ZM02, Arducam).

A NEMA 17 stepper motor, controlled by a stepper motor driver (TB6600, SZCY LLC), rotates the carousel to position samples within the field of view. The system's operation is managed by two control units: a single-board computer (Raspberry Pi 400) that runs the operating system, image acquisition, and image processing, and a microcontroller (Arduino Nano) which manages the timed processes of LED illumination and stepper motor control. The single-board computer triggers the camera and sends commands to the microcontroller via serial communication.

High-Throughput Fluorescence Detection

High-throughput testing was conducted using previously validated SARS-CoV-2, ZIKV, and IBV samples, both positive and negative. A total of 96 samples were tested, with groups of 12 samples (e.g., six positive and six negative for SARS-CoV-2) measured 10 times each. Samples were loaded in batches using six-device cartridges to maintain order. Each set was processed through the detector, with measurements taken for all samples before reloading. In total, 960 fluorescence measurements were completed in 27 min and 25 seconds. Downtime between sample groups was not included in the throughput calculation, as it was specific to maintaining sample order and not reflective of real-world performance. In practical applications, individual test identifiers would allow for continuous sample processing at the reported throughput. The variability in device positioning is depicted in supplemental Figure 8.6.

Statistical Analysis

Differences in fluorescence ratios between positive and negative samples were analyzed for SARS-CoV-2, ZIKV, IBV, and the SC2 Sous Vide method. Normality was evaluated through Q-Q plots, CDFs, and the Kolmogorov-Smirnov test. When the data did not meet the assumption of normality, the non-parametric Mann-Whitney U test (Wilcoxon rank-sum) was applied. Additional visualizations, including scatter histograms with kernel density estimates, were used to further compare the distributions between positive and negative samples (Supplemental Figure 8.8). Fluorescence ratios were compared using two-sample t-tests for each test type, confirming significant differences between positive and negative groups with p-values less than 1e-10 (Supplemental Figure 8.8).

For high-throughput testing, 96 samples (12 per group) were measured 10 times, yielding 960 measurements. For each sample, the Z-score of the fluorescence ratio was calculated to assess consistency across multiple runs. The Z-score was determined by subtracting the mean fluorescence ratio of all measurements from the individual sample's fluorescence ratio, and then dividing the result by the standard deviation of the fluorescence ratios. This provides a standardized value for each measurement, indicating its deviation from the mean in units of standard deviation. (Figure 8.5).

Sous Vide Incubation

An incubating water bath was constructed using a 5-gallon bucket filled with 10 L of water and a sous vide circulating heater (1100 Watt Miaton, MZJ-01, Amazon). The temperature was monitored by an analog thermometer, a digital thermocouple, and the built-in sensors of the sous vide heater (Supplemental Figure 8.7). The set temperature of the sous vide was adjusted to ensure a consistent 65°C bath temperature, as verified by the additional temperature readings. Reaction vessels were placed in a custom 3D-printed floating sample holder, ensuring consistent heat transfer and uniform incubation just below the water surface (Supplemental Figure 8.7).

Supplemental Information

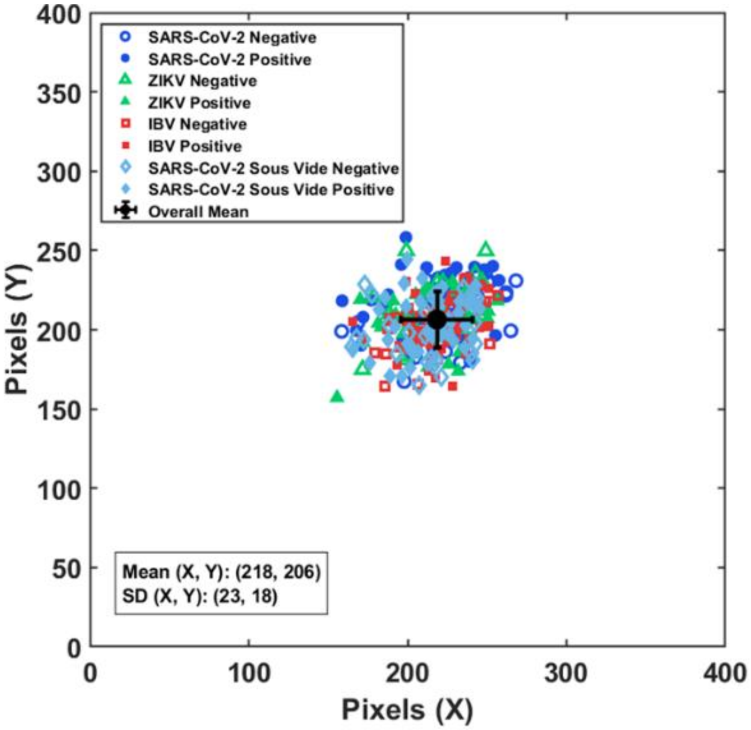

Figure 8.6. XY positioning of devices in high throughput detector. The center coordinates of the sample reaction chambers as determined by image analysis of the fluorescent measurement images. Active positioning of devices causes variability in imaged positions in relation to the optical system. The mean pixel location of the reaction chamber placement is found to be at (218, 206) with a standard deviation of 23 and 18 in the X and Y directions respectively.

Figure 8.7. Sous vide incubation setup. (Left) Example of sous vide incubation set up including circulating heater, thermometer, thermocouple, and timer. Water temperature is checked independently by both analog thermometer and thermocouple to hold nominal temperature of 65C. (Right) Image of microcentrifuge tubes in a floating 3D printed rack.

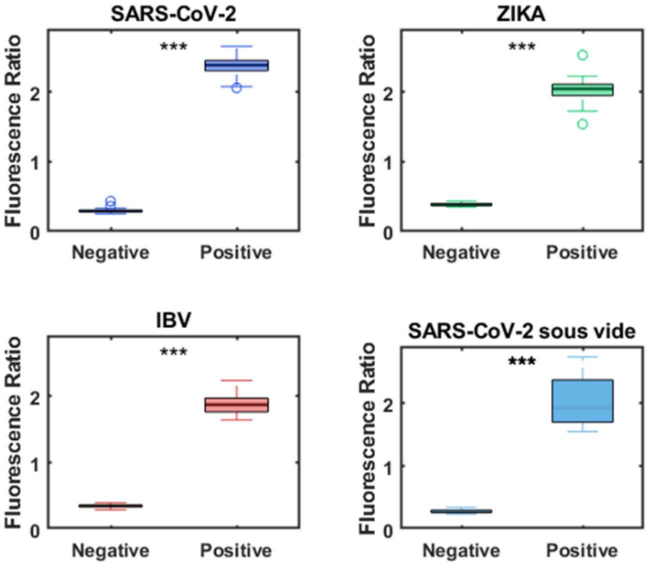

Figure 8.8. Boxplots of Fluorescence Ratios for Negative and Positive Samples Across Different Test Types**.** Comparison of fluorescence ratios for negative and positive samples for SARS-CoV-2, Zika virus (ZIKV), influenza B virus (IBV), and SARS-CoV-2 incubated with sous vide. Positive samples display significantly higher fluorescence ratios compared to negative samples in all test types (*** indicates p-values less than 0.0001).

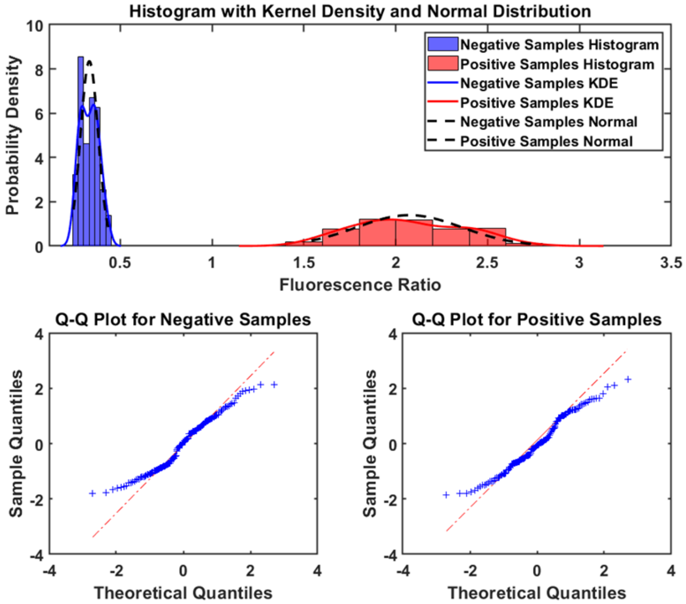

Figure 8.9. Fluorescence Ratio Distribution and Normality Assessment for Positive and Negative Samples. (Top Panel) Histogram of fluorescence ratios for negative (blue) and positive (red) samples, overlaid with corresponding Kernel Density Estimates (KDE) and fitted normal distributions (dashed lines). The negative sample distributions show a concentrated peak with a low fluorescence ratio, whereas positive samples exhibit higher fluorescence ratios, indicating successful amplification. (Bottom Panels) Q-Q plots of fluorescence ratios for negative (left) and positive (right) samples against theoretical quantiles of a normal distribution. The Q-Q plots indicate normality for both sample groups, with data points following the expected line for normal distribution (red dashed line).

CHAPTER NINE

CONCLUSION

This dissertation has explored two distinct applications of 3D printing: the fabrication of synthetic biofilms for studying structure-function relationships and the development of diagnostic methods tailored to emergent infectious disease response.

Biofilm Engineering via 3D Bioprinting

In chapters 3 and 4, I introduced a method of light-based 3D printing to create synthetic biofilms. By embedding *Pseudomonas fluorescens* bacteria within a photopolymerized PEG-DA hydrogel matrix, we achieved precise control over the initial synthetic biofilm geometry and composition. This approach enabled systematic exploration of the resultant biofilm heterogeneity and structure by modulating initial cell densities. Through the characterization of bacterial growth, spatial heterogeneity, and other emergent properties, the findings of this study offer valuable insights into the relationship between structure and function within this synthetic biofilm system.

In biofilm engineering, the ability to fabricate synthetic biofilms with directed structural characteristics unlocks opportunities to study microbial ecology, biofilm control, and biofilm-based technologies. These advancements can support applications such as bioprocessing, bioremediation, and the development of engineered living materials, providing opportunities to address critical environmental and industrial challenges. For example, engineered biofilms may be designed to create controlled metabolic niche spaces by spatially arranging microbes with selected metabolisms within the same structure, producing a living structure capable of optimizing for select processes, such as denitrification, supporting goals of bioremediation or bioprocessing.

Several limitations of this bioprinting method warrant discussion. With light based bioprinting, the choice of materials and photopolymerization processes present questions related to biocompatibility and biological relevance. Alternative printing materials or process adaptations, such as naturally derived materials or visible light based photopolymerization, may improve compatibility with model organisms and better support future research. Moreover, the synthetic biofilm models developed here focus on relatively small-scale systems. While these models provide valuable insights, scaling these systems for applications such as bioprocessing and bioremediation presents additional challenges.

Development of High-Throughput Diagnostics

In chapters 6, 7, and 8 I discussed the use of 3D printing for the development of diagnostics to address limitations in current pathogen detection methods. I used 3D printing to rapidly prototype a diagnostic platform combining reverse transcription loop-mediated isothermal amplification (RT-LAMP) with a user-friendly point-of-care diagnostic device and a custom high-throughput fluorescence detection system. This diagnostic method achieved fluorescence detection throughput of over 2,100 samples per hour, surpassing many currently available diagnostic methods while reducing required testing infrastructure and maintaining adaptability to novel pathogens. Moreover, a low-cost, resource-efficient incubation system assembled from a circulating water heater was validated, demonstrating the potential for deployment in resource-limited settings.

The diagnostic methods developed here aim to support population-scale testing without reliance on expensive equipment or centralized laboratories, ensuring deployment in resource-limited settings and promoting equitable healthcare access. These innovations address key limitations in existing diagnostic systems, such as scalability and accessibility. By fostering the development of accessible diagnostics that better scale to the needs of population testing and surveillance, this work contributes to health equity, pandemic preparedness, and the advancement of technological solutions for societal benefit.

While these results demonstrate the potential of his diagnostic workflow, further development is necessary to translate these systems into deployable point-of-care diagnostic tools. The validation performed in these studies relies on laboratory-prepared samples run under controlled conditions, which do not capture the variability of real-world environments. Optimizing the RT-LAMP biochemistry for diverse, real-world conditions will be essential to ensure specificity and sensitivity across various pathogens and patient samples. Additionally, refining the device design for usability and to improve manufacturability could improve test success costs and support manufacturing at scale. Finally, integrating additional automation, such as continuous incubation systems (e.g. conveyor ovens) with throughput comparable to the described diagnostic detector, could further increase diagnostic efficiency and scalability, advancing the potential for widespread implementation.

Concluding Remarks

The investigations presented within this dissertation underscore the versatility of 3D printing as an enabling technology, addressing critical gaps in both fundamental science and practical applications. As demonstrated, 3D printing can be used to create experimental models (e.g. synthetic biofilms) and to develop novel supporting hardware (e.g. a high-throughput fluorescence detector) through customizable and accessible fabrication made possible by the continually growing set of printing methods and materials. As 3D printing technologies continue to evolve, their applicability in research and applied sciences will expand. Embracing these evolving capabilities will empower researchers and developers to address new and pressing challenges, advancing progress across a wide range of scientific and engineering disciplines.

CUMULATIVE REFERENCES CITED

1. Flemming, H. C. & Wuertz, S. Bacteria and archaea on Earth and their abundance in biofilms. *Nat. Rev. Microbiol.* **17**, 247–260 (2019).

2. Flemming, H. C. *et al.* Biofilms: An emergent form of bacterial life. *Nat. Rev. Microbiol.* **14**, 563–575 (2016).

3. Gougoulias, C., Clark, J. M. & Shaw, L. J. The role of soil microbes in the global carbon cycle: Tracking the below-ground microbial processing of plant-derived carbon for manipulating carbon dynamics in agricultural systems. *J. Sci. Food Agric.* **94**, 2362–2371 (2014).

4. Dixon, R. & Kahn, D. Genetic regulation of biological nitrogen fixation. *Nat. Rev. Microbiol.* **2**, 621–631 (2004).

5. Wang, D., Xu, A., Elmerich, C. & Ma, L. Z. Biofilm formation enables free-living nitrogen-fixing rhizobacteria to fix nitrogen under aerobic conditions. *ISME J.* **11**, 1602–1613 (2017).

6. Gupta, A., Gupta, R. & Singh, R. L. *Microbes and Environment. Principles and Applications of Environmental Biotechnology for a Sustainable Future* (2017). doi:10.1007/978-981-10-1866-4

7. Mannaa, M., Han, G., Seo, Y. S. & Park, I. Evolution of Food Fermentation Processes and the Use of Multi-Omics in Deciphering the Roles of the Microbiota. *Foods* **10**, (2021).

8. Liu, L. *et al.* Fermented beverage and food storage in 13,000 y-old stone mortars at Raqefet Cave, Israel: Investigating Natufian ritual feasting. *J. Archaeol. Sci. Reports* **21**, 783–793 (2018).

9. Al-Kaidy, H. *et al.* Biotechnology and Bioprocess Engineering – From the First Ullmann's Article to Recent Trends. *ChemBioEng Rev.* **2**, 175–184 (2015).

10. Schmeckebier, A., Zayed, A. & Ulber, R. Productive biofilms: from prokaryotic to eukaryotic systems. *J. Chem. Technol. Biotechnol.* **97**, 3049–3064 (2022).

11. Sharma, M. *et al.* Recent advances in microbial engineering approaches for wastewater treatment: a review. *Bioengineered* **14**, 2184518 (2023).

12. Philipp, L. A., Bühler, K., Ulber, R. & Gescher, J. Beneficial applications of biofilms. *Nat. Rev. Microbiol.* **22**, 276–290 (2024).

13. Tan, E. C. D. & Lamers, P. Circular Bioeconomy Concepts—A Perspective. *Front. Sustain.* **2**, 1–8 (2021).

14. Chen, C.-Y., Yeh, K.-L., Aisyah, R., Lee, D.-J. & Chang, J.-S. Cultivation, photobioreactor design and harvesting of microalgae for biodiesel production: A critical review. *Bioresour. Technol.* **102**, 71–81 (2011).

15. Acharjee, S. A. *et al. PHA-Based Bioplastic: a Potential Alternative to Address Microplastic Pollution. Water, Air, and Soil Pollution* **234**, (Springer International

Publishing, 2023).

16. Antranikian, G. & Streit, W. R. Microorganisms harbor keys to a circular bioeconomy making them useful tools in fighting plastic pollution and rising CO2 levels. *Extremophiles* **26**, 1–11 (2022).

17. Rosenboom, J.-G., Langer, R. & Traverso, G. Bioplastics for a circular economy. *Nat. Rev. Mater.* **7**, 117–137 (2022).

18. Cámara, M. *et al.* Economic significance of biofilms: a multidisciplinary and cross-sectoral challenge. *npj Biofilms Microbiomes* **8**, 1–8 (2022).

19. Vartoukian, S. R., Palmer, R. M. & Wade, W. G. Strategies for culture of 'unculturable' bacteria. *FEMS Microbiol. Lett.* **309**, 1–7 (2010).

20. Martiny, A. C. High proportions of bacteria are culturable across major biomes. *ISME J.* **13**, 2125–2128 (2019).

21. Flemming, H. C. & Wingender, J. The biofilm matrix. *Nat. Rev. Microbiol.* **8**, 623–633 (2010).

22. Flemming, H. C. *et al.* The biofilm matrix: multitasking in a shared space. *Nat. Rev. Microbiol.* **21**, 70–86 (2023).

23. Sauer, K. *et al.* The biofilm life cycle: expanding the conceptual model of biofilm formation. *Nat. Rev. Microbiol.* **20**, 608–620 (2022).

24. Stewart, P. S. & Franklin, M. J. Physiological heterogeneity in biofilms. *Nat. Rev. Microbiol.* **6**, 199–210 (2008).

25. Williamson, K. S. *et al.* Heterogeneity in Pseudomonas aeruginosa biofilms includes expression of ribosome hibernation factors in the antibiotic-tolerant subpopulation and hypoxia-induced stress response in the metabolically active population. *J. Bacteriol.* **194**, 2062–2073 (2012).

26. Pabst, B., Pitts, B., Lauchnor, E. & Stewart, P. S. Gel-Entrapped Staphylococcus aureus Bacteria as Models of Biofilm Infection Exhibit Growth in Dense Aggregates, Oxygen Limitation, Antibiotic Tolerance, and Heterogeneous Gene Expression. *Antimicrob. Agents Chemother.* **60**, 6294–301 (2016).

27. Smriga, S., Ciccarese, D. & Babbin, A. R. Denitrifying bacteria respond to and shape microscale gradients within particulate matrices. *Commun. Biol.* **4**, 1–9 (2021).

28. Coraça-Huber, D. C. *et al.* Identification and morphological characterization of biofilms formed by strains causing infection in orthopedic implants. *Pathogens* **9**, 1–18 (2020).

29. Bridier, A., Dubois-Brissonnet, F., Boubetra, A., Thomas, V. & Briandet, R. The biofilm architecture of sixty opportunistic pathogens deciphered using a high throughput CLSM method. *J. Microbiol. Methods* **82**, 64–70 (2010).

30. Pereira, M. O., Kuehn, M., Wuertz, S., Neu, T. & Melo, L. F. Effect of flow regime on the

architecture of a Pseudomonas fluorescens biofilm. *Biotechnol. Bioeng.* **78**, 164–171 (2002).

31. Co, J. Y. *et al.* Mucins trigger dispersal of Pseudomonas aeruginosa biofilms. *npj Biofilms Microbiomes* **4**, 1–8 (2018).

32. Azeredo, J. *et al.* Critical review on biofilm methods. *Crit. Rev. Microbiol.* **43**, 313–351 (2017).

33. Buckingham-Meyer, K., Goeres, D. M. & Hamilton, M. A. Comparative evaluation of biofilm disinfectant efficacy tests. *J. Microbiol. Methods* **70**, 236–244 (2007).

34. Djordjevic, D., Wiedmann, M. & McLandsborough, L. A. Microtiter plate assay for assessment of Listeria monocytogenes biofilm formation. *Appl. Environ. Microbiol.* **68**, 2950–2958 (2002).

35. Goeres, D. M. *et al.* A method for growing a biofilm under low shear at the air-liquid interface using the drip flow biofilm reactor. *Nat. Protoc.* **4**, 783–788 (2009).

36. Rusconi, R., Garren, M. & Stocker, R. Microfluidics expanding the frontiers of microbial ecology. *Annu. Rev. Biophys.* **43**, 65–91 (2014).

37. Pérez-Rodríguez, S., García-Aznar, J. M. & Gonzalo-Asensio, J. Microfluidic devices for studying bacterial taxis, drug testing and biofilm formation. *Microb. Biotechnol.* **15**, 395–414 (2022).

38. Blanco-Cabra, N. *et al.* A new BiofilmChip device for testing biofilm formation and antibiotic susceptibility. *npj Biofilms Microbiomes* **7**, (2021).

39. Pratt, S. L. *et al.* DropSOAC: Stabilizing microfluidic drops for time-lapse quantification of single-cell bacterial physiology. *Front. Microbiol.* **10**, 1–13 (2019).

40. Tibbitt, M. W. & Anseth, K. S. Hydrogels as extracellular matrix mimics for 3D cell culture. *Biotechnol. Bioeng.* **103**, 655–663 (2009).

41. Caliari, S. R. & Burdick, J. A. A practical guide to hydrogels for cell culture. *Nat. Methods* **13**, 405–414 (2016).

42. Wang, B. X., Xu, W., Yang, Z., Wu, Y. & Pi, F. An Overview on Recent Progress of the Hydrogels: From Material Resources, Properties, to Functional Applications. *Macromol. Rapid Commun.* **43**, 1–22 (2022).

43. Strathmann, M. & Griebe, T. Arti®cial bio®lm model ± a useful tool for bio®lm research. 231–237 (2000).

44. Aristotelous, A. C. *et al.* Diffusive transport through a model host-biofilm system. *Phys. Rev. E - Stat. Nonlinear, Soft Matter Phys.* **92**, 1–7 (2015).

45. Hagel, V., Haraszti, T. & Boehm, H. Diffusion and interaction in PEG-DA hydrogels. *Biointerphases* **8**, 1–9 (2013).

46. Chan, V., Zorlutuna, P., Jeong, J. H., Kong, H. & Bashir, R. Three-dimensional photopatterning of hydrogels using stereolithography for long-term cell encapsulation. *Lab Chip* **10**, 2062–2070 (2010).

47. Zhang, Q. *et al.* Morphogenesis and cell ordering in confined bacterial biofilms. *Proc. Natl. Acad. Sci. U. S. A.* **118**, (2021).

48. Koo, H. & Yamada, K. M. Dynamic cell-matrix interactions modulate microbial biofilm and tissue 3D microenvironments. *Curr. Opin. Cell Biol.* **42**, 13–2 (2016).

49. Han, Y. *et al.* Extracellular Matrix Rigidities Regulate the Tricarboxylic Acid Cycle and Antibiotic Resistance of Three-Dimensionally Confined Bacterial Microcolonies. *Adv. Sci.* **10**, 1–13 (2023).

50. Klebe, R. J. Cytoscribing: A method for micropositioning cells and the construction of two- and three-dimensional synthetic tissues. *Exp. Cell Res.* **179**, 362–373 (1988).

51. Wilson, W. C. & Boland, T. Cell and organ printing 1: Protein and cell printers. *Anat. Rec. - Part A Discov. Mol. Cell. Evol. Biol.* **272**, 491–496 (2003).

52. Dababneh, A. B. & Ozbolat, I. T. Bioprinting Technology: A Current State-of-the-Art Review. (2014). doi:10.1115/1.4028512

53. Gu, Z., Fu, J., Lin, H. & He, Y. Development of 3D bioprinting: From printing methods to biomedical applications. *Asian J. Pharm. Sci.* **15**, 529–557 (2020).

54. Murphy, S. V & Atala, A. 3D bioprinting of tissues and organs. *Nat. Biotechnol.* **32**, 773–785 (2014).

55. Ke, D. & Murphy, S. V. Current Challenges of Bioprinted Tissues Toward Clinical Translation. *Tissue Eng. - Part B Rev.* **25**, 1–13 (2019).

56. Hospodiuk, M., Dey, M., Sosnoski, D. & Ozbolat, I. T. The bioink: A comprehensive review on bioprintable materials. *Biotechnol. Adv.* **35**, 217–239 (2017).

57. Chang, R., Nam, J. & Sun, W. Effects of dispensing pressure and nozzle diameter on cell survival from solid freeform fabrication-based direct cell writing. *Tissue Eng. - Part A.* **14**, 41–48 (2008).

58. Maruo, S. & Ikuta, K. Submicron stereolithography for the production of freely movable mechanisms by using single-photon polymerization. *Sensors Actuators, A Phys.* **100**, 70–76 (2002).

59. Benjamin, A. *et al.* Light-Based 3D Printing of Hydrogels with High-Resolution Channels. (2018). doi:10.1088/2057

60. Wang, Z. *et al.* A simple and high-resolution stereolithography-based 3D bioprinting system using visible light crosslinkable bioinks. *Biofabrication* **7**, (2015).

61. Pagac, M. *et al.* A Review of Vat Photopolymerization Technology : Materials. *Polymers (Basel).* **13**, 598 (2021).

62. Dhariwala, B., Hunt, E., Boland, T. & Ph, D. Rapid Prototyping of Tissue-Engineering Constructs , Using. **10**, 1316–1322 (2004).

63. Arcaute, K., Mann, B. K. & Wicker, R. B. Stereolithography of Three-Dimensional Bioactive Poly(Ethylene Glycol) Constructs with Encapsulated Cells. *Ann. Biomed. Eng.* **34**, 1429–1441 (2006).

64. Fairbanks, B. D., Schwartz, M. P., Bowman, C. N. & Anseth, K. S. Photoinitiated polymerization of PEG-diacrylate with lithium phenyl-2,4,6-trimethylbenzoylphosphinate: polymerization rate and cytocompatibility. *Biomaterials* **30**, 6702–6707 (2009).

65. Männel, M. J., Fischer, C. & Thiele, J. A non-cytotoxic resin for micro-stereolithography for cell cultures of HUVECs. *Micromachines* **11**, (2020).

66. Zhou, X. *et al.* 3D Bioprinting a Cell-Laden Bone Matrix for Breast Cancer Metastasis Study. *ACS Appl. Mater. Interfaces* **8**, 30017–30026 (2016).

67. Ma, X. *et al.* Deterministically patterned biomimetic human iPSC-derived hepatic model via rapid 3D bioprinting. *Proc. Natl. Acad. Sci.* **113**, 2206–2211 (2016).

68. Dubbin, K. *et al.* Projection Microstereolithographic Microbial Bioprinting for Engineered Biofilms. *Nano Lett.* **21**, 1352–1359 (2021).

69. Zhu, W. *et al.* Direct 3D bioprinting of prevascularized tissue constructs with complex microarchitecture. *Biomaterials* **124**, 106–115 (2017).

70. Raman, R. *et al.* High-Resolution Projection Microstereolithography for Patterning of Neovasculature. *Adv. Healthc. Mater.* **5**, 610–619 (2016).

71. Ma, X. *et al.* Rapid 3D bioprinting of decellularized extracellular matrix with regionally varied mechanical properties and biomimetic microarchitecture. *Biomaterials* **185**, 310–321 (2018).

72. Saygili, E., Dogan-gurbuz, A. A., Yesil-celiktas, O. & Draz, M. S. 3D Bioprinting : A Powerful Tool to Leverage Tissue Engineering and Microbial Systems. *Bioprinting* e00071 (2019). doi:10.1016/j.bprint.2019.e00071

73. Lowden, O. What are the leading companies in 3D bioprinting. *bccResearch* (2023). Available at: https://blog.bccresearch.com/what-are-the-leading-companies-in-3d-bioprinting.

74. Schaffner, M., Rühs, P. A., Coulter, F., Kilcher, S. & Studart, A. R. 3D printing of bacteria into functional complex materials. *Sci. Adv.* **3**, (2017).

75. Murga, R., Stewart, P. S. & Daly, D. Quantitative analysis of biofilm thickness variability. *Biotechnol. Bioeng.* **45**, 503–510 (1995).

76. Suarez, C. *et al.* Thickness determines microbial community structure and function in nitrifying biofilms via deterministic assembly. *Sci. Rep.* **9**, 1–10 (2019).

77. Ning, E. *et al.* 3D bioprinting of mature bacterial biofilms for antimicrobial resistance

drug testing. *Biofabrication* **11**, (2019).

78. Bhusari, S., Sankaran, S. & del Campo, A. Regulating Bacterial Behavior within Hydrogels of Tunable Viscoelasticity. *Adv. Sci.* **9**, 1–10 (2022).

79. Tuson, H. H. *et al.* Measuring the stiffness of bacterial cells from growth rates in hydrogels of tunable elasticity. *Mol. Microbiol.* **84**, 874–891 (2012).

80. De Maria, C. *et al.* Biofabrication: A Guide to Technology and Terminology. *Trends Biotechnol.* (2017). doi:10.1016/j.tibtech.2017.10.015

81. Hull, C. APPARATUS FOR PRODUCTION OF THREE-DMENSONAL OBJECTS BY STEREO THOGRAPHY. *Google Patents* (1986). doi:10.1088/1757-899X/716/1/012012

82. Debroy, D., Oakey, J. & Li, D. Interfacially-mediated oxygen inhibition for precise and continuous poly(ethylene glycol) diacrylate (PEGDA) particle fabrication. *J. Colloid Interface Sci.* **510**, 334–344 (2018).

83. Darulis, A. The Complete Resin 3D printing setting guide for beginners. *Ameralabs* Available at: https://ameralabs.com/blog/the-complete-resin-3d-printing-settings-guide-for-beginners/#:~:text=What is Burn-in Layer,stick to the build plate.

84. Pan, Y., He, H., Xu, J. & Feinerman, A. Study of separation force in constrained surface projection stereolithography. *Rapid Prototyp. J.* **23**, 353–361 (2017).

85. Hakim Khalili, M. *et al.* Mechanical Behavior of 3D Printed Poly(ethylene glycol) Diacrylate Hydrogels in Hydrated Conditions Investigated Using Atomic Force Microscopy. *ACS Appl. Polym. Mater.* **5**, 3034–3042 (2023).

86. Tim. Optimal layer exposure time for perfect resin prints. *Core Electronics* (2023). Available at: https://core-electronics.com.au/guides/perfect-resin-print-exposure-setting/#Bottom.

87. Idris, M., Seers, T. D. & Alyafei, N. MethodsX An operational guide to resin 3D printing of geological macromodels ☆. *MethodsX* **9**, 101863 (2022).

88. Anycubic. How to Level Resin 3D Printer. *Anycubic/blog* Available at: https://store.anycubic.com/blogs/3d-printing-guides/how-to-level-resin-3d-printer.

89. Chitubox. How to Level the Build Plate on a Bottom-up 3D Printer? *Chitubox/academy* Available at: https://www.chitubox.com/en/academy/advanced/how-to-level-the-build-plate-on-a-bottom-up-3d-printer.

90. Liu, J. *et al.* Current Understanding of the Applications of Photocrosslinked Hydrogels in Biomedical Engineering. *Gels* **8**, 1–26 (2022).

91. Benjamin, A. D. *et al.* Light-based 3D printing of hydrogels with high-resolution channels. *Biomed. Phys. Eng. Express* **5**, (2019).

92. Nguyen, A. K., Goering, P. L., Elespuru, R. K., Das, S. S. & Narayan, R. J. The photoinitiator lithium phenyl (2,4,6-Trimethylbenzoyl) phosphinate with exposure to 405

nm light is cytotoxic to mammalian cells but not mutagenic in bacterial reverse mutation assays. *Polymers (Basel).* **12**, 1–13 (2020).

93. Tomal, W. & Ortyl, J. Water-Soluble Photoinitiators in Biomedical Applications. 1–30 (2020). doi:10.3390/polym12051073

94. Xu, H., Casillas, J., Krishnamoorthy, S. & Xu, C. Effects of Irgacure 2959 and lithium phenyl-2,4,6-trimethylbenzoylphosphinate on cell viability, physical properties, and microstructure in 3D bioprinting of vascular-like constructs. *Biomed. Mater.* **15**, (2020).

95. Sabnis, A., Rahimi, M., Chapman, C. & Nguyen, K. T. Cytocompatibility studies of an in situ photopolymerized thermoresponsive hydrogel nanoparticle system using human aortic smooth muscle cells. *J. Biomed. Mater. Res. - Part A* **91**, 52–59 (2009).

96. Yang, Y., Zhou, Y., Lin, X., Yang, Q. & Yang, G. Printability of external and internal structures based on digital light processing 3D printing technique. *Pharmaceutics* **12**, 1–16 (2020).

97. Bagheri, A. & Jin, J. Photopolymerization in 3D Printing. *ACS Appl. Polym. Mater.* **1**, 593–611 (2019).

98. Chanda, M. Free Radical Polymerization. *Introd. to Polym. Sci. Chem.* 311–404 (2020). doi:10.1201/b14577-10

99. Yagci, Y., Jockusch, S. & Turro, N. J. Photoinitiated polymerization: Advances, challenges, and opportunities. *Macromolecules* **43**, 6245–6260 (2010).

100. Directorate, S. M. Ultraviolet Waves. *National Aeronautics and Space Administration* Available at: https://science.nasa.gov/ems/10_ultravioletwaves/. (Accessed: 14th October 2024)

101. Hopkins, R. How Ultraviolet Light Reacts in Cells. *Scitable* (2015). Available at: https://www.nature.com/scitable/blog/scibytes/how_ultraviolet_light_reacts_in/#:~:text=One way ultraviolet light can,of UV light hits DNA.

102. Ramos, C. C. R. *et al.* Use of ultraviolet-C in environmental sterilization in hospitals: A systematic review on efficacy and safety. *Int. J. Health Sci. (Qassim).* **14**, 52–65 (2020).

103. Khan, A. Q., Travers, J. B. & Kemp, M. G. Roles of UVA radiation and DNA damage responses in melanoma pathogenesis. *Environ. Mol. Mutagen.* **59**, 438–460 (2018).

104. Ravanat, J. L., Douki, T. & Cadet, J. Direct and indirect effects of UV radiation on DNA and its components. *J. Photochem. Photobiol. B Biol.* **63**, 88–102 (2001).

105. Ng, W. L. *et al.* Vat polymerization-based bioprinting - process, materials, applications and regulatory challenges. *Biofabrication* **12**, (2020).

106. Murdoch, L. E., MacLean, M., Endarko, E., MacGregor, S. J. & Anderson, J. G. Bactericidal effects of 405nm light exposure demonstrated by inactivation of escherichia, salmonella, Shigella, Listeria, and mycobacterium species in liquid suspensions and on

exposed surfaces. *Sci. World J.* **2012**, (2012).

107. Chen, H., Cheng, Y. & Moraru, C. I. Blue 405 nm LED light effectively inactivates bacterial pathogens on substrates and packaging materials used in food processing. *Sci. Rep.* **13**, 1–13 (2023).

108. Idil, Ö., Özkanca, R., Darcan, C. & Flint, K. P. Escherichia coli: Dominance of red light over other visible light sources in establishing viable but nonculturable state. *Photochem. Photobiol.* **86**, 104–109 (2010).

109. Tomb, R. M. *et al.* Invited Review Review of the Comparative Susceptibility of Microbial Species to Photoinactivation Using 380 – 480 nm Violet-Blue Light. 445–458 (2018). doi:10.1111/php.12883

110. Veloso, T. M., de Souza da Fonseca, A. & Costa dos Santos, G. Effects of light-emitting diodes on cell biology. *Front. Photonics* **3**, 1–13 (2022).

111. Fasnacht, M. & Polacek, N. Oxidative Stress in Bacteria and the Central Dogma of Molecular Biology. *Front. Mol. Biosci.* **8**, 1–13 (2021).

112. O'Connell, C. D. *et al.* Tailoring the mechanical properties of gelatin methacryloyl hydrogels through manipulation of the photocrosslinking conditions. *Soft Matter* **14**, 2142–2151 (2018).

113. Phaniendra, A., Jestadi, D. B. & Periyasamy, L. Free Radicals: Properties, Sources, Targets, and Their Implication in Various Diseases. *Indian J. Clin. Biochem.* **30**, 11–26 (2015).

114. Li, W. *et al.* Stereolithography apparatus and digital light processing-based 3D bioprinting for tissue fabrication. *iScience* **26**, 106039 (2023).

115. Huh, J. T. *et al.* Combinations of photoinitiator and UV absorber for cell-based digital light processing (DLP) bioprinting. *Biofabrication* **13**, (2021).

116. Zheng, Z. *et al.* Visible Light-Induced 3D Bioprinting Technologies and Corresponding Bioink Materials for Tissue Engineering: A Review. *Engineering* (2020). doi:10.1016/j.eng.2020.05.021

117. Han, D., Yang, C., Fang, N. X. & Lee, H. Rapid Multi-Material 3D Printing with Projection Micro-Stereolithography Using Dynamic Fluidic Control. *Additive Manufacturing* (2019). doi:10.1016/J.ADDMA.2019.03.031

118. Kowsari, K., Akbari, S., Wang, D., Fang, N. X. & Ge, Q. High-Efficiency High-Resolution Multimaterial Fabrication for Digital Light Processing-Based Three-Dimensional Printing. *3D Print. Addit. Manuf.* **5**, 185–193 (2018).

119. Miri, A. K. *et al.* Microfluidics-Enabled Multimaterial Maskless Stereolithographic Bioprinting. *Adv. Mater.* **30**, 1–9 (2018).

120. Mayer, F. *et al.* Multimaterial 3D laser microprinting using an integrated microfluidic

system. *Sci. Adv.* **5**, eaau9160 (2019).

121. Wang, M. *et al.* Digital Light Processing Based Bioprinting with Composable Gradients. *Adv. Mater.* **34**, 1–13 (2022).

122. Mhade, S. & Kaushik, K. S. Tools of the Trade: Image Analysis Programs for Confocal Laser-Scanning Microscopy Studies of Biofilms and Considerations for Their Use by Experimental Researchers. *ACS Omega* **8**, 20163–20177 (2023).

123. Boulos, L., Prévost, M., Barbeau, B., Coallier, J. & Desjardins, R. LIVE/DEAD(®) BacLight(TM): Application of a new rapid staining method for direct enumeration of viable and total bacteria in drinking water. *J. Microbiol. Methods* **37**, 77–86 (1999).

124. Nikolic, N., Barner, T. & Ackermann, M. Analysis of fluorescent reporters indicates heterogeneity in glucose uptake and utilization in clonal bacterial populations. *BMC Microbiol.* **13**, 1–13 (2013).

125. Fulaz, S. *et al.* Ratiometric Imaging of the in Situ pH Distribution of Biofilms by Use of Fluorescent Mesoporous Silica Nanosensors. *ACS Appl. Mater. Interfaces* **11**, 32679–32688 (2019).

126. Jewell, M. P., Galyean, A. A., Harris, J. K., Zemanick, E. T. & Cash, K. J. Luminescent nanosensors for ratiometric monitoring of three-dimensional oxygen gradients in laboratory and clinical Pseudomonas aeruginosa biofilms. *Appl. Environ. Microbiol.* **85**, (2019).

127. Yilmaz, S., Haroon, M. F., Rabkin, B. A., Tyson, G. W. & Hugenholtz, P. Fixation-free fluorescence in situ hybridization for targeted enrichment of microbial populations. *ISME J.* **4**, 1352–1356 (2010).

128. Pitts, B. & Stewart, P. Confocal Laser Microscopy on Biofilms: Successes and Limitations. *Micros. Today* **16**, 18–23 (2008).

129. Parker, A. E., Christen, J. A., Lorenz, L. & Smith, H. Optimal surface estimation and thresholding of confocal microscope images of biofilms using Beer's Law. *J. Microbiol. Methods* **174**, 105943 (2020).

130. Spring, K. R., Fellers, T. J. & Davidson, M. W. Resolution and Contrast in Confocal Microscopy. *OLYMPUS* 1–11 (2014). Available at: https://www.olympus-lifescience.com/en/microscope-resource/primer/techniques/confocal/resolutionintro/.

131. Auld, D. S. *et al.* Microplate Selection and Recommended Practices in High-throughput Screening and Quantitative Biology. *Assay Guid. Man.* 1–50 (2004).

132. Cellvis. Cellvis 96 Well Glass Bottom Plates. Available at: https://www.cellvis.com/_96-well-glass-bottom-plates_/products_by_category.php?cat_id=11.

133. Secretariat Society for Laboratory Automation and Screening. ANSI SLAS Footprint Dimensions. **2004**, (2004).

134. Tomeckova, V. & Halloran, J. W. Cure depth for photopolymerization of ceramic suspensions. *J. Eur. Ceram. Soc.* **30**, 3023–3033 (2010).

135. FrantzDale, B., Keeter, M., Galese, M. & Matyas-Peti, C. Formlabs OpenFL.

136. Taormina, G., Sciancalepore, C., Messori, M. & Bondioli, F. 3D printing processes for photocurable polymeric materials: technologies, materials, and future trends. *J. Appl. Biomater. Funct. Mater.* **16**, 151–160 (2018).

137. Manual, R. Imaris.

138. Imaris Tutorials. *Oxford Instruments* Available at: https://imaris.oxinst.com/tutorials.

139. Olsen, I. Biofilm-specific antibiotic tolerance and resistance. *Eur. J. Clin. Microbiol. Infect. Dis.* **34**, 877–886 (2015).

140. Percival, S. L., Suleman, L., Vuotto, C. & Donelli, G. Healthcare-Associated infections, medical devices and biofilms: Risk, tolerance and control. *J. Med. Microbiol.* **64**, 323–334 (2015).

141. Stewart, P. S. & Costerton, J. W. Antibiotic resistance of bacteria in biofilms. *Lancet* **358**, 135–138 (2001).

142. Sriyuth Murthy, P. & Venkatesan, R. Industrial Biofilms and their Control. in *Marine and Industrial Biofouling* 65–101 (Springer Berlin Heidelberg, 2009). doi:10.1007/7142

143. Davey, M. E. & O'toole, G. A. Microbial Biofilms: from Ecology to Molecular Genetics. *Microbiol. Mol. Biol. Rev.* **64**, 847–867 (2000).

144. Bharathi, S. D. *et al.* Resource Recycling, Recovery, and Xenobiotic Remediation from E-wastes Through Biofilm Technology: A Review. *Appl. Biochem. Biotechnol.* **195**, 5669–5692 (2023).

145. Stewart, P. S. Diffusion in biofilms. *Journal of Bacteriology* (2003). doi:10.1128/JB.185.5.1485-1491.2003

146. Wentland, E. J., Stewart, P. S., Huang, C. T. & McFeters, G. A. Spatial variations in growth rate within Klebsiella pneumoniae colonies and biofilm. *Biotechnol. Prog.* **12**, 316–321 (1996).

147. Walters III, M. C., Roe, F., Bugnicourt, A., Franklin, M. J. & Stewart, P. S. Contributions of Antibiotic Penetration, Oxygen Limitation. *Antimicrob. Agents Chemother.* **47**, 317–323 (2003).

148. Von Ohle, C. *et al.* Real-time microsensor measurement of local metabolic activities in ex vivo dental biofilms exposed to sucrose and treated with chlorhexidine. *Appl. Environ. Microbiol.* **76**, 2326–2334 (2010).

149. Berk, V. *et al.* Molecular architecture and assembly principles of Vibrio cholerae biofilms. *Science (80-.).* **337**, 236–239 (2012).

150. Mishra, S. *et al.* Biofilm-mediated bioremediation is a powerful tool for the removal of environmental pollutants. *Chemosphere* **294**, 133609 (2022).

151. Araújo, P. A. *et al.* Influence of Flow Velocity on the Characteristics of Pseudomonas fluorescens Biofilms . *J. Environ. Eng.* **142**, 1–8 (2016).

152. Mironov, V. *et al.* Biofabrication: A 21st century manufacturing paradigm. *Biofabrication* **1**, (2009).

153. Wangpraseurt, D., You, S., Sun, Y. & Chen, S. Biomimetic 3D living materials powered by microorganisms. *Trends Biotechnol.* **40**, 843–857 (2022).

154. Balasubramanian, S., Aubin-Tam, M. E. & Meyer, A. S. 3D Printing for the Fabrication of Biofilm-Based Functional Living Materials. *ACS Synth. Biol.* **8**, 1564–1567 (2019).

155. Balasubramanian, S., Yu, K., Meyer, A. S., Karana, E. & Aubin-Tam, M. E. Bioprinting of Regenerative Photosynthetic Living Materials. *Adv. Funct. Mater.* (2021). doi:10.1002/adfm.202011162

156. Duraj-Thatte, A. M. *et al.* Programmable microbial ink for 3D printing of living materials produced from genetically engineered protein nanofibers. *Nat. Commun.* **12**, (2021).

157. Krige, A., Rova, U. & Christakopoulos, P. 3D bioprinting on cathodes in microbial electrosynthesis for increased acetate production rate using Sporomusa ovata. *J. Environ. Chem. Eng.* **9**, 106189 (2021).

158. Smercina, D. *et al.* Synthetic Soil Aggregates : Bioprinted Habitats for. (2022).

159. Mattei, M. R. *et al.* Continuum and discrete approach in modeling biofilm development and structure: a review. *J. Math. Biol.* **76**, 945–1003 (2018).

160. Pearson, A. N. *et al.* The pGinger Family of Expression Plasmids. *Microbiol. Spectr.* **11**, (2023).

161. Thorgersen, M. P. *et al.* Nitrateutilizing microorganisms resistant to multiple metals from the heavily contaminated Oak Ridge Reservation. *Appl. Environ. Microbiol.* **85**, (2019).

162. Xu, K. D., Stewart, P. S., Xia, F., Huang, C. T. & McFeters, G. A. Spatial physiological heterogeneity in Pseudomonas aeruginosa biofilm is determined by oxygen availability. *Appl. Environ. Microbiol.* **64**, 4035–4039 (1998).

163. Hentzer, M., Eberl, L. & Givskov, M. Transcriptome analysis of Pseudomonas aeruginosa biofilm development: Anaerobic respiration and iron limitation. *Biofilms* **2**, 37–61 (2005).

164. Lipkowitz, G. *et al.* Injection continuous liquid interface production of 3D objects. *Sci. Adv.* **8**, 1–7 (2022).

165. Cruise, G. M., Scharp, D. S. & Hubbell, J. A. Characterization of permeability and network structure of interfacially photopolymerized poly(ethylene glycol) diacrylate hydrogels. *Biomaterials* **19**, 1287–1294 (1998).

166. Koo, H. & Yamada, K. M. Dynamic cell-matrix interactions modulate microbial biofilm and tissue 3D microenvironments. *Curr. Opin. Cell Biol.* **42**, 102–112 (2016).

167. Pabst, B., Pitts, B., Lauchnor, E. & Stewart, P. S. Gel-entrapped Staphylococcus aureus bacteria as models of biofilm infection exhibit growth in dense aggregates, oxygen limitation, antibiotic tolerance, and heterogeneous gene expression. *Antimicrob. Agents Chemother.* **60**, 6294–6301 (2016).

168. Cole, J. J. Aquatic microbiology for ecosystem scientists: New and recycled paradigms in ecological microbiology. *Ecosystems* **2**, 215–225 (1999).

169. Wagley, S. *et al.* Bacterial dormancy: A subpopulation of viable but non-culturable cells demonstrates better fitness for revival. *PLoS Pathog.* **17**, 1–26 (2021).

170. Marshall, D. J., Cameron, H. E. & Loreau, M. Relationships between intrinsic population growth rate, carrying capacity and metabolism in microbial populations. *ISME J.* **17**, 2140–2143 (2023).

171. Chandris, P., Giannouli, C. C. & Panayotou, G. Imaging Approaches for the Study of Metabolism in Real Time Using Genetically Encoded Reporters. *Front. Cell Dev. Biol.* **9**, 1–14 (2022).

172. Tomeckova, V. & Halloran, J. W. Predictive models for the photopolymerization of ceramic suspensions. *J. Eur. Ceram. Soc.* **30**, 2833–2840 (2010).

173. Liu, P. Y. *et al.* Real-Time measurement of single bacterium's refractive index using optofluidic immersion refractometry. *Procedia Eng.* **87**, 356–359 (2014).

174. Jo, Y. *et al.* Angle-resolved light scattering of individual rod-shaped bacteria based on Fourier transform light scattering. *Sci. Rep.* **4**, 1–6 (2014).

175. Stevenson, K., McVey, A. F., Clark, I. B. N., Swain, P. S. & Pilizota, T. General calibration of microbial growth in microplate readers. *Sci. Rep.* **6**, 4–10 (2016).

176. Russell, R. E., DiRenzo, G. V., Szymanski, J. A., Alger, K. E. & Grant, E. H. C. Principles and Mechanisms of Wildlife Population Persistence in the Face of Disease. *Front. Ecol. Evol.* **8**, 1–11 (2020).

177. Pongsiri, M. J. *et al.* Biodiversity loss affects global disease ecology. *Bioscience* **59**, 945–954 (2009).

178. Piret, J. & Boivin, G. Pandemics Throughout History. *Front. Microbiol.* **11**, (2021).

179. Ehrenpreis, J. E. & Ehrenpreis, E. D. A Historical Perspective of Healthcare Disparity and Infectious Disease in the Native American Population. *Am. J. Med. Sci.* **363**, 288–294 (2022).

180. Mathieu, E. *et al.* Coronavirus (COVID-19) Cases. Available at: https://ourworldindata.org/covid-cases.

181. Jones, K. E. *et al.* Global trends in emerging infectious diseases. *Nature* **451**, 990–993

(2008).

182. WHO. List of Blueprint priority diseases. (2018). Available at: https://web.archive.org/web/20200301083134/http://origin.who.int/blueprint/priority-diseases/en/.

183. Agyapon-Ntra, K. & McSharry, P. E. A global analysis of the effectiveness of policy responses to COVID-19. *Sci. Rep.* **13**, 1–15 (2023).

184. Juneau, C. E. *et al.* Lessons from past pandemics: a systematic review of evidence-based, cost-effective interventions to suppress COVID-19. *Syst. Rev.* **11**, 1–17 (2022).

185. Hale, T. *et al.* What have we learned from tracking every government policy on COVID-19 for the past two years? *BSG Work. Pap.Ser* 1–26 (2022).

186. Excler, J. L., Saville, M., Berkley, S. & Kim, J. H. Vaccine development for emerging infectious diseases. *Nat. Med.* **27**, 591–600 (2021).

187. Boro, E. & Stoll, B. Barriers to COVID-19 Health Products in Low-and Middle-Income Countries During the COVID-19 Pandemic: A Rapid Systematic Review and Evidence Synthesis. *Front. Public Heal.* **10**, (2022).

188. Kelly-Cirino, C. D. *et al.* Importance of diagnostics in epidemic and pandemic preparedness. *BMJ Glob. Heal.* **4**, 1–8 (2019).

189. Perkins, M. D. *et al.* Diagnostic preparedness for infectious disease outbreaks. *Lancet* **390**, 2211–2214 (2017).

190. Mercer, T. R. & Salit, M. Testing at scale during the COVID-19 pandemic. *Nat. Rev. Genet.* **22**, 415–426 (2021).

191. Shang, W. *et al.* Percentage of Asymptomatic Infections among SARS-CoV-2 Omicron Variant-Positive Individuals: A Systematic Review and Meta-Analysis. *Vaccines* **10**, (2022).

192. Li, R. *et al.* Substantial undocumented infection facilitates the rapid dissemination of novel coronavirus (SARS-CoV-2). *Science (80-.).* **368**, 489–493 (2020).

193. Peeling, R. W., Heymann, D. L., Teo, Y. Y. & Garcia, P. J. Diagnostics for COVID-19: moving from pandemic response to control. *Lancet* **399**, 757–768 (2022).

194. Frnda, J. & Durica, M. On Pilot Massive COVID-19 Testing by Antigen Tests in Europe. Case Study: Slovakia. *Infect. Dis. Rep.* **13**, 45–57 (2021).

195. The COVID-19 testing debacle. *Nat. Biotechnol.* **38**, 653 (2020).

196. Behnam, M., Dey, A., Gambell, T. & Talwar, V. COVID-19: Overcoming supply shortages for diagnostic testing. *McKinsey Co.* 1–8 (2020).

197. Allen, Danielle (James Bryant Conant University Professor, Director, Edmond J. Safra Center for Ethics, H. U. *et al.* Roadmap to Pandemic Resilience: Massive Scale Testing,

Tracing, and Supported Isolation (TTSI) as the Path to Pandemic Resilience for a Free Society. (2020).

198. Sheridan, C. Coronavirus and the race to distribute reliable diagnostics. *Nat. Biotechnol.* **38**, 382–384 (2020).

199. Corman, V. M. *et al.* Detection of 2019 novel coronavirus (2019-nCoV) by real-time RT-PCR. *Eurosurveillance* **25**, (2020).

200. Mardian, Y., Kosasih, H., Karyana, M., Neal, A. & Lau, C. Y. Review of Current COVID-19 Diagnostics and Opportunities for Further Development. *Front. Med.* **8**, (2021).

201. Garg, N., Ahmad, F. J. & Kar, S. Recent advances in loop-mediated isothermal amplification (LAMP) for rapid and efficient detection of pathogens. *Curr. Res. Microb. Sci.* **3**, 100120 (2022).

202. Chowell, G., Hengartner, N. W., Castillo-Chavez, C., Fenimore, P. W. & Hyman, J. M. The basic reproductive number of Ebola and the effects of public health measures: The cases of Congo and Uganda. *J. Theor. Biol.* **229**, 119–126 (2004).

203. Evans, S., Naylor, N. R., Fowler, T., Hopkins, S. & Robotham, J. The effectiveness and efficiency of asymptomatic SARS-CoV-2 testing strategies for patient and healthcare workers within acute NHS hospitals during an omicron-like period. *BMC Infect. Dis.* **24**, 1–13 (2024).

204. Larremore, D. B. *et al.* Test sensitivity is secondary to frequency and turnaround time for COVID-19 screening. *Sci. Adv.* **7**, 1–10 (2021).

205. Land, K. J., Boeras, D. I., Chen, X. S., Ramsay, A. R. & Peeling, R. W. REASSURED diagnostics to inform disease control strategies, strengthen health systems and improve patient outcomes. *Nat. Microbiol.* **4**, 46–54 (2019).

206. Kevadiya, B. D. *et al.* Diagnostics for SARS-CoV-2 infections. *Nat. Mater.* **20**, 593–605 (2021).

207. Petralia, S. & Conoci, S. PCR technologies for point of care testing: Progress and perspectives. *ACS Sensors* **2**, 876–891 (2017).

208. World Health Organization(WHO). Practical considerations for implementation of the Roche cobas MTB and cobas MTB-RIF/INH assays. 1–5 (2021).

209. The Global Fund. Pooled Procurement Mechanism Reference Pricing: COVID-19 diagnostics. 1–5 (2022).

210. Cobb, B. *et al.* The cobas® 6800/8800 System: a new era of automation in molecular diagnostics. *Expert Rev. Mol. Diagn.* **17**, 167–180 (2017).

211. Pfefferle, S., Reucher, S., Nörz, D. & Lütgehetmann, M. Evaluation of a quantitative RT-PCR assay for the detection of the emerging coronavirus SARS-CoV-2 using a high

throughput system. *Eurosurveillance* **25**, 1–5 (2020).

212. Aretzweiler, G., Leuchter, S., Simon, C. O., Marins, E. & Frontzek, A. Generating timely molecular diagnostic test results: workflow comparison of the cobas® 6800/8800 to Panther. *Expert Rev. Mol. Diagn.* **19**, 951–957 (2019).

213. Degli-Angeli, E. *et al.* Validation and verification of the Abbott RealTime SARS-CoV-2 assay analytical and clinical performance. *J. Clin. Virol.* **129**, 18–20 (2020).

214. Marshall, R. *et al.* Characteristics of the m2000 automated sample preparation and multiplex real-time PCR system for detection of Chlamydia trachomatis and Neisseria gonorrhoeae. *J. Clin. Microbiol.* **45**, 747–751 (2007).

215. Smith, E. *et al.* Analytical and clinical comparison of three nucleic acid amplification tests for SARS-CoV-2 detection. *J. Clin. Microbiol.* **58**, (2020).

216. Pu, R. *et al.* The screening value of RT-LAMP and RT-PCR in the diagnosis of COVID-19: systematic review and meta-analysis Ruiyang. (2022).

217. Budd, J. *et al.* Lateral flow test engineering and lessons learned from COVID-19. *Nat. Rev. Bioeng.* **1**, 13–31 (2023).

218. Kumar, R. *et al.* Advancements in COVID-19 Testing: An In-depth Overview. *Curr. Pharm. Biotechnol.* **24**, 1122–1148 (2022).

219. Lo, B. J., Cox, C., Amin, K. & Telesford, I. Prices for COVID-19 testing. (2023).

220. CDC Museum COVID-19 Timeline. *CDC* Available at: https://www.cdc.gov/museum/timeline/covid19.html.

221. Dao Thi, V. L. *et al.* A colorimetric RT-LAMP assay and LAMP-sequencing for detecting SARS-CoV-2 RNA in clinical samples. *Sci. Transl. Med.* **12**, (2020).

222. Schmidt, J. *et al.* A semi-automated, isolation-free, high-throughput SARS-CoV-2 reverse transcriptase (RT) loop-mediated isothermal amplification (LAMP) test. *Sci. Rep.* **11**, 1–9 (2021).

223. Lucira ^{TM} COVID-19 Test Kit.

224. Notomi, T. *et al.* Loop-mediated isothermal amplification of DNA. *Med. del Lav.* **28**, e63 (2000).

225. Lin, E. E., Razzaque, U. A., Burrows, S. A. & Smoukov, S. K. End-to-end system for rapid and sensitive early-detection of SARS-CoV-2 for resourcepoor and field-test environments using a $51 lab-in-a-backpack. *PLoS One* **17**, 1–12 (2022).

226. CVS Online Store : LUCIRA At Home Test. *CVS* (2024). Available at: https://www.cvs.com/shop/lucira-by-pfizer-covid-19-flu-home-test-1-ct-prodid-557909.

227. In Vitro Diagnostics EUAs - Molecular Diagnostic Tests for SARS-CoV-2. Available at: https://www.fda.gov/medical-devices/covid-19-emergency-use-authorizations-medical-

devices/in-vitro-diagnostics-euas-molecular-diagnostic-tests-sars-cov-2#individual-molecular.

228. Baek, Y. H. *et al.* Development of a reverse transcription-loop-mediated isothermal amplification as a rapid early-detection method for novel SARS-CoV-2. *Emerg. Microbes Infect.* **9**, 998–1007 (2020).

229. Brihn, A. *et al.* Diagnostic Performance of an Antigen Test with RT-PCR for the Detection of SARS-CoV-2 in a Hospital Setting —Los Angeles County, California, June–August 2020. *MMWR Recomm. Reports* **70**, 702–706 (2021).

230. Arshadi, M. *et al.* Diagnostic Accuracy of Rapid Antigen Tests for COVID-19 Detection: A Systematic Review With Meta-analysis. *Front. Med.* **9**, 1–13 (2022).

231. CVS Store - Rapid Antigen Test. *CVS* (2024). Available at: https://www.cvs.com/shop/flowflex-covid-19-antigen-home-test-1-ct-prodid-823994.

232. Lollar, R. H. EUA Quidel Corporation Sofia SARS Antigen FIA. 1–10 (2021).

233. West, R. & Gronvall, G. K. The COVID-19 XPRIZE and the need for scalable, fast, and widespread testing. *Nat. Biotechnol.* **38**, 1021 (2020).

234. Stokes, E. K. *et al.* Coronavirus Disease 2019 Case Surveillance — United States, January 22–May 30, 2020. *MMWR. Morb. Mortal. Wkly. Rep.* **69**, 759–765 (2020).

235. Bennett, N. R. *et al.* Atomically accurate de novo design of single-domain antibodies. *bioRxiv Prepr. Serv. Biol.* (2024). doi:10.1101/2024.03.14.585103

236. Puhach, O., Meyer, B. & Eckerle, I. SARS-CoV-2 viral load and shedding kinetics. *Nat. Rev. Microbiol.* **21**, 147–161 (2023).

237. Thompson, D. & Lei, Y. Mini review: Recent progress in RT-LAMP enabled COVID-19 detection. *Sensors and Actuators Reports* **2**, 100017 (2020).

238. Lei, Y. Kitchen Range Oven Enabled One-tube RT-LAMP for RNA Detection at Home - A Potential Solution for Large-scale Screening of COVID-19. 1–18 (2020).

239. Francois, P. *et al.* Robustness of a loop-mediated isothermal amplification reaction for diagnostic applications. *FEMS Immunol. Med. Microbiol.* **62**, 41–48 (2011).

240. Raddatz, B. W. *et al.* Development of an optimized colorimetric RT-LAMP for SARS-CoV-2 assay with enhanced procedure controls for remote diagnostics. *Sci. Rep.* **12**, 1–13 (2022).

241. Moehling, T. J., Choi, G., Dugan, L. C., Salit, M. & Meagher, R. J. LAMP Diagnostics at the Point-of-Care: Emerging Trends and Perspectives for the Developer Community. *Expert Rev. Mol. Diagn.* **21**, 43–61 (2021).

242. Mori, Y., Nagamine, K., Tomita, N. & Notomi, T. Detection of loop-mediated isothermal amplification reaction by turbidity derived from magnesium pyrophosphate formation. *Biochem. Biophys. Res. Commun.* **289**, 150–154 (2001).

243. Tanner, N. A., Zhang, Y. & Evans, T. C. Visual detection of isothermal nucleic acid amplification using pH-sensitive dyes. *Biotechniques* **58**, 59–68 (2015).

244. Waheed, W. *et al.* A deep learning-driven low-power, accurate, and portable platform for rapid detection of COVID-19 using reverse-transcription loop-mediated isothermal amplification. *Sci. Rep.* **12**, 1–18 (2022).

245. Ball, C. S. *et al.* Quenching of Unincorporated Amplification Signal Reporters in Reverse-Transcription Loop-Mediated Isothermal Amplification Enabling Bright, Single-Step, Closed-Tube, and Multiplexed Detection of RNA Viruses. *Anal. Chem.* **88**, 3562–3568 (2016).

246. Lee, S. H. *et al.* One-pot reverse transcriptional loop-mediated isothermal amplification (RT-LAMP) for detecting MERS-CoV. *Front. Microbiol.* **7**, 1–13 (2017).

247. Mendoza-Gallegos, R. A., Rios, A. & Garcia-Cordero, J. L. An Affordable and Portable Thermocycler for Real-Time PCR Made of 3D-Printed Parts and Off-the-Shelf Electronics. *Anal. Chem.* **90**, 5563–5568 (2018).

248. Buultjens, A. H. *et al.* Low-Cost, Open-Source Device for High-Performance Fluorescence Detection of Isothermal Nucleic Acid Amplification Reactions. *ACS Biomater. Sci. Eng.* **7**, 4982–4990 (2021).

249. Papadakis, G. *et al.* Portable real-time colorimetric LAMP-device for rapid quantitative detection of nucleic acids in crude samples. *Sci. Rep.* **12**, 1–15 (2022).

250. Mauro, E. *Lucira by Pfizer COVID-19 & Flu Test EUA*. (2023).

251. The Pandemic Preparedness Partnership. 100 Days Mission to respond to future pandemic threats. *UK Gov.* 1–84 (2021).

252. Lee, J. Monochromator vs Filter-Based Plate Reader: Which is Better? 1–2 (2021). Available at: https://www.promegaconnections.com/monochromator-vs-filter-based-plate-reader-which-is-better/.

253. Bushway, P. J., Mercola, M. & Price, J. H. A comparative analysis of standard microtiter plate reading versus imaging in cellular assays. *Assay Drug Dev. Technol.* **6**, 557–567 (2008).

254. Munster, V. J., Koopmans, M., van Doremalen, N., van Riel, D. & de Wit, E. A Novel Coronavirus Emerging in China — Key Questions for Impact Assessment. *N. Engl. J. Med.* **382**, 692–694 (2020).

255. Mina, B. M. J. & Andersen, K. G. COVID-19 testing: One size does not fit all. **37**, 126–127 (2021).

256. Jain, K. K. Nanotechnology in clinical laboratory diagnostics. *Clin. Chim. acta.* **358**,

257. Janda, J. M. & Abbott, S. L. 16S rRNA gene sequencing for bacterial identification in the diagnostic laboratory: Pluses, perils, and pitfalls. *J. Clin. Microbiol.* **45**, 2761–2764

(2007).

258. Gao, Y. *et al.* Diagnostic utility of clinical laboratory data determinations for patients with the severe COVID-19. *J. Med. Virol.* **92**, 791–796 (2020).

259. Chiappin, S., Antonelli, G., Gatti, R. & De Palo, E. F. Saliva specimen: A new laboratory tool for diagnostic and basic investigation. *Clin. Chim. acta* **383**, 30–40 (2007).

260. Yager, P., Domingo, G. J. & Gerdes, J. Point-of-care diagnostics for global health. *Annu. Rev. Biomed. Eng.* **10**, 107—144 (2008).

261. Hu, J. *et al.* Advances in paper-based point-of-care diagnostics. *Biosens. Bioelectron.* **54**, 585–597 (2014).

262. Gubala, V., Harris, L. F., Ricco, A. J., Tan, M. X. & Williams, D. E. Point of care diagnostics: Status and future. *Anal. Chem.* **84**, 487–515 (2012).

263. Craw, P. & Balachandran, W. Isothermal nucleic acid amplification technologies for point-of-care diagnostics: A critical review. *Lab Chip* **12**, 2469–2486 (2012).

264. Chin, C. D., Linder, V. & Sia, S. K. Commercialization of microfluidic point-of-care diagnostic devices. *Lab Chip* **12**, 2118–2134 (2012).

265. Ahn, C. H. *et al.* Disposable smart lab on a chip for point-of-care clinical diagnostics. *Proc. IEEE* **92**, 154–173 (2004).

266. Yetisen, A. K., Akram, M. S. & Lowe, C. R. Paper-based microfluidic point-of-care diagnostic devices. *Lab Chip* **13**, 2210–2251 (2013).

267. Wang, J. Electrochemical biosensors: Towards point-of-care cancer diagnostics. *Biosens. Bioelectron.* **21**, 1887–1892 (2006).

268. Yang, S. & Rothman, R. E. free information in English and Mandarin on the novel coronavirus COVID- Review PCR-based diagnostics for infectious diseases : uses , limitations , and future applications in acute-care settings. (2020).

269. Reed, G. H., Kent, J. O. & Wittwer, C. T. High-resolution DNA melting analysis for simple and efficient molecular diagnostics. *Pharmacogenomics* **8**, 597–608 (2007).

270. Huggett, J. F., Cowen, S. & Foy, C. A. Considerations for Digital PCR as an Accurate Molecular Diagnostic Tool. *Clin. Chem.* **61**, 79–88 (2015).

271. Elnifro, E. M., Ashshi, A. M., Cooper, R. J. & Klapper, P. E. Multiplex PCR: Optimization and application in diagnostic virology. *Clin. Microbiol. Rev.* **13**, 559–570 (2000).

272. Porte, L. *et al.* Evaluation of a novel antigen-based rapid detection test for the diagnosis of SARS-CoV-2 in respiratory samples. *Int. J. Infect. Dis.* **99**, 328–333 (2020).

273. Mak, G. C. *et al.* Evaluation of rapid antigen test for detection of SARS-CoV-2 virus. *J. Clin. Virol.* **129**, 104500 (2020).

274. Hirotsu, Y. *et al.* Comparison of automated SARS-CoV-2 antigen test for COVID-19 infection with quantitative RT-PCR using 313 nasopharyngeal swabs, including from seven serially followed patients. *Int. J. Infect. Dis.* **99**, 397–402 (2020).

275. Dinnes, J. *et al.* Rapid, point-of-care antigen and molecular-based tests for diagnosis of SARS-CoV-2 infection. *Cochrane Database Syst. Rev.* **2021**, (2021).

276. Saiki, R. K. *et al.* Enzymatic amplification of beta-globin genomic sequences and restriction site analysis for diagnosis of sickle cell anemia. *Science* **230**, 1350–1354 (1985).

277. Saiki, R. K. *et al.* Primer-directed enzymatic amplification of DNA with a thermostable DNA polymerase. *Science* **239**, 487–491 (1988).

278. Mullis, K. B. & Faloona, F. A. [21] Specific synthesis of DNA in vitro via a polymerase-catalyzed chain reaction. *Methods Enzymol.* **155**, 335–350 (1987).

279. Mullis, K. *et al.* Specific enzymatic amplification of DNA in vitro: the polymerase chain reaction. *Cold Spring Harb. Symp. Quant. Biol.* **51 Pt 1**, 263–273 (1986).

280. Mackay, I. M. Real-time PCR in the microbiology laboratory. *Clin. Microbiol. Infect. Off. Publ. Eur. Soc. Clin. Microbiol. Infect. Dis.* **10**, 190–212 (2004).

281. Johnston, S. P. *et al.* PCR as a confirmatory technique for laboratory diagnosis of malaria. *J. Clin. Microbiol.* **44**, 1087–1089 (2006).

282. Geha, D. J., Uhl, J. R., Gustaferro, C. A. & Persing, D. H. Multiplex PCR for identification of methicillin-resistant staphylococci in the clinical laboratory. *J. Clin. Microbiol.* **32**, 1768–1772 (1994).

283. Espy, M. J. *et al.* Erratum: Real-time PCR in clinical microbiology: Applications for routine laboratory testing [Clinical Microbiology Reviews [2006] 19, 1[165-256]]. *Clin. Microbiol. Rev.* **19**, 595 (2006).

284. Park, S., Zhang, Y., Lin, S., Wang, T. H. & Yang, S. Advances in microfluidic PCR for point-of-care infectious disease diagnostics. *Biotechnol. Adv.* **29**, 830–839 (2011).

285. Lee, S. H., Kim, S.-W., Kang, J. Y. & Ahn, C. H. A polymer lab-on-a-chip for reverse transcription (RT)-PCR based point-of-care clinical diagnostics. *Lab Chip* **8**, 2121–2127 (2008).

286. Tomita, N., Mori, Y., Kanda, H. & Notomi, T. Loop-mediated isothermal amplification (LAMP) of gene sequences and simple visual detection of products. *Nat. Protoc.* **3**, 877–882 (2008).

287. Nagamine, K., Hase, T. & Notomi, T. Accelerated reaction by loop-mediated isothermal amplification using loop primers. *Mol. Cell. Probes* **16**, 223–229 (2002).

288. Cutting Corners on Injection-Molded Parts. Available at: https://www.protolabs.com/resources/design-tips/cutting-corners-on-injection-molded-

parts/.

289. Whats the Average Hand Size for Men, Women, and Children. Available at: https://www.healthline.com/health/average-shoe-size-for-men.

290. Peeling, R. W., Olliaro, P. L., Boeras, D. I. & Fongwen, N. Scaling up COVID-19 rapid antigen tests: promises and challenges. *Lancet Infect. Dis.* **21**, e290–e295 (2021).

291. Jordan, L. & Kurtz, R. Optical Design of CFX96 ™ Real-Time PCR Detection System Eliminates the Requirement of a Passive Reference Dye. *Bio-Rad Lab. Inc.* tech note 6047 (2000).

292. Zhang, Y. *et al.* Enhancing colorimetric loop-mediated isothermal amplification speed and sensitivity with guanidine chloride. *Biotechniques* **69**, 179–185 (2020).

293. Ge, Y. *et al.* Detection of influenza viruses by coupling multiplex reverse-transcription loop-mediated isothermal amplification with cascade invasive reaction using nanoparticles as a sensor. *Int. J. Nanomedicine* **12**, 2645–2656 (2017).

294. Priye, A. *et al.* A smartphone-based diagnostic platform for rapid detection of Zika, chikungunya, and dengue viruses. *Sci. Rep.* **7**, 1–11 (2017).

APPENDICES

APPENDIX A

AUTOMATED DATA EXTRACTION AND ORGANIZATION FOR BIOFILM ANALYSIS

This MATLAB script automates the extraction and organization of biofilm analysis data across multiple folders, designed for cases where multiple datasets are stored in a structured directory and identified by specific folder names. The code consolidates data from individual folders, capturing properties such as volume, position (X, Y, Z), intensity, and time, and compiles them into a single, organized dataset for each unique well-position combination, facilitating downstream analysis of biofilm growth and structure. To use this script, specify the main folder path containing the dataset folders. The script identifies folders that match a particular naming pattern (e.g., '*_Statistics') and extracts data from CSV files within these folders, which are named according to specific data types (e.g., 'Volume,' 'Position_X,' 'Intensity'). It then organizes this information into a structured format and aligns positional data (X and Z) to correct for spatial discrepancies across time points. The final dataset is stored in a cell array, grouped by unique well-position combinations. To run this script, update the 'folder_path' variable with the correct path to the main folder, and the output will be a consolidated dataset of biofilm metrics that can be used for further analysis or visualization. Note that this code assumes a specific naming convention for files and folders, so ensure the data structure follows these conventions for accurate processing

```
% Author : Isaak Thornton

% Date : Last updated 2023_9_29

clear all;


% Define the folder path where the data folders are located
% Adjust the folder path as needed for each analysis session
folder_path = 'ENTER_FILE_PATH_HERE';
```

```
% Define the pattern to match the folder names
pattern = '*_Statistics';

% Get a list of all folder names in the directory that match the pattern
folder_list = dir(fullfile(folder_path, pattern));

n_folders = numel(folder_list);
wells = cell(n_folders, 1);
positions = cell(n_folders, 1);
data_wells = cell(4);

% Specify the types of data to be extracted
dataType = {'Volume', 'Time', 'PosZ', 'PosX', 'PosY', 'IntMean', 'ID', 'Well'};
raw_data = cell(0, numel(dataType));

% Loop through each folder and extract the data you need
for i = 1:length(folder_list)
    folder_name = folder_list(i).name;
    full_folder_path = fullfile(folder_path, folder_name);

    % Extract data between square brackets
    data_between_brackets = extractBetween(folder_name, '[', ']');


% Extract time

%for timelapse --> time data should come from Imaris data
%for individual time points - time in imaris folers is 0 --> need to
%populate own time
time_str = '';
if ~isempty(data_between_brackets)
    data_parts = strsplit(data_between_brackets{1}, '_');
    time_parts = find(contains(data_parts, 'hr') | contains(data_parts, 'hrs'));

    time_str = data_parts{time_parts};

end

    % Extract well
    well_str = '';
    if ~isempty(data_between_brackets)
        well_idx = find(contains(data_parts, 'A'));
        well_str = data_parts{well_idx};
```

```
end
wells{i} = well_str;

% Extract position information if present
position_str = '';
if ~isempty(data_between_brackets)
   pos_idx = find(contains(data_parts, 'Position'));
   position_str = data_parts{pos_idx};
end
positions{i} = position_str;

% Define file paths for each data type based on the folder and filename
filename = extractBefore(folder_name, 'Statistics');
file_ext = '.csv' ;

% Specify data type file names
datatypeVol = 'Volume';
datatypeTime = 'Time';
datatypePosZ = 'Position_Z';
datatypePosX = 'Position_X';
datatypePosY = 'Position_Y';

datatypeInt = 'Intensity_Mean_Ch=1_Img=1';
datatypeCoMZ = 'Center_of_Image_Mass_Z';

% Specify data type file names
fVolume =   [filename  , datatypeVol,  file_ext];
fPosZ =   [filename,   datatypePosZ,  file_ext];
fPosX =   [filename,   datatypePosX,  file_ext];
fPosY =   [filename,   datatypePosY,  file_ext];
fInt =   [filename,   datatypeInt,  file_ext];
fTime =   [filename,   datatypeTime,  file_ext];

% Construct file paths for each data type
file_path_Volume  = fullfile(folder_path,folder_name, fVolume);
file_path_PosZ    = fullfile(folder_path,folder_name, fPosZ);
file_path_PosX    = fullfile(folder_path,folder_name, fPosX);
file_path_PosY    = fullfile(folder_path,folder_name, fPosY);
file_path_Int     = fullfile(folder_path,folder_name, fInt);
file_path_Time     = fullfile(folder_path,folder_name, fTime);

% Read data tables from each file
dataVolume  = readtable(file_path_Volume, "VariableNamingRule", "preserve");
dataPosZ  =  readtable(file_path_PosZ,   "VariableNamingRule", "preserve");
```

```
            dataPosX   =  readtable(file_path_PosX,   "VariableNamingRule", "preserve");
            dataPosY   =  readtable(file_path_PosY,   "VariableNamingRule", "preserve");
            dataInt   =   readtable(file_path_Int,    "VariableNamingRule", "preserve");
            dataTime   =   readtable(file_path_Time,    "VariableNamingRule", "preserve");

            % Organize extracted data into a structured format
            raw_data{i}.Volume = dataVolume.Volume;
            raw_data{i}.PosX = dataPosX.("Position X");
            raw_data{i}.PosY = dataPosY.("Position Y");
            raw_data{i}.PosZ = dataPosZ.("Position Z");
            raw_data{i}.Int = dataInt.("Intensity Mean");
            raw_data{i}.Time = dataTime.("Time");


            % Set time value based on conditions

            %raw_data{i}.Time = str2double(regexp(time_str, '\d+', 'match'));
            raw_data{i}.Time = repmat(str2double(regexp(time_str, '\d+', 'match')),
numel(raw_data{i}.PosZ), 1);

            % Assign well and position identifiers
            raw_data{i}.Well = wells{i};
            raw_data{i}.Position = positions{i};


          end
        dataNames =          ["A" "B " "C" ];
        dataNamesPositions = ["Treatment_1" "Treatment_2 " "Control" ];

        dataNamesFiles = ["100x" "10x " "thin" ];

        treatment = "figure title"; %for figure titles
        treatment_file = "File_Naming_Tag" ;  %for figures save as function

        %%
        % Get unique well-position combinations
        wp = unique(strcat(wells, positions));
        numWells = length(unique(wells));
        w = unique(wells);
        numPosition = length(wp);

        % Initialize a cell array to store the concatenated data for each well-position combination
        data = cell(size(wp));
```

```
      header_names = {'Volume', 'Time', 'PosZ', 'PosX',  'PosY', 'Int', 'Position', 'Well', 'WP'};


      % Loop through each unique well-position combination
      for i = 1:length(wp)
        current_wp = wp{i};

        % Find the indices of the data sets with the current Well-Position combination
        idx = find(strcmp(strcat(wells, positions), current_wp));

        % Concatenate the data sets into a single table
        temp_data = table();
        for j = 1:length(idx)
          % Replicate time values to match the length of volume
          %time_replicated = repmat(raw_data{idx(j)}.Time,
length(raw_data{idx(j)}.Volume), 1);
          position_replicated = repmat(raw_data{idx(j)}.Position,
length(raw_data{idx(j)}.Volume), 1);
          well_replicated = repmat(raw_data{idx(j)}.Well, length(raw_data{idx(j)}.Volume),
1);
          wp_replicated = repmat(current_wp, length(raw_data{idx(j)}.Volume), 1);
          temp_data = [temp_data; table(raw_data{idx(j)}.Volume, raw_data{idx(j)}.Time,
raw_data{idx(j)}.PosZ, raw_data{idx(j)}.PosX, raw_data{idx(j)}.PosY,...
                raw_data{idx(j)}.Int, position_replicated,  well_replicated, wp_replicated)];
        end

        % Add the header names to the table
        temp_data.Properties.VariableNames = header_names;

        % Store the concatenated data in the corresponding cell of concatenated_data
        data{i} = temp_data;
      end

      % set up time variables
      timepoints = unique(data{1}.Time);
      tsteps = length(timepoints);
```

APPENDIX B

PROCESSING CODE FOR FLUORESCENCE DETECTOR DATA

This MATLAB script processes data captured from the Rapid Serial Detector, producing visual output for analysis. The code pulls data from multiple runs and test types, then sorts, processes, and generates statistics on the fluorescence signals. The use of samples refers to each individual test. For example, for experiments where 12 negative and 12 positive samples were analyzed, 24 samples will be combined and compared within the code. Multiple sample detection is referred to as multiple “runs”. For most experiments, each sample is run three times. The blue or blu channel refers to the fluorescence channel measuring the QUASR fluorescent probe (i.e. reporter signal) for the assay. The yellow or “yel” channel refers to the fluorescence channel measuring the ROX dye fluorescence (i.e. reference signal) for the assay. Ratio values refer to the reporter signal divided by the reference signal, the calculation of background subtracted pixel sum performed by the embedded computer within the detector (see Chapters 6 & 7).

```
%MATLAB code for processing Rapid Serial Detector Capture Data
%take text log from fluorescence detector and output data plots
%Input parameters of run (# of samples, # of Positives, Log filenames,
%ect..) then output desired plots for comparison

%Author : Isaak Thornton
%Date : Last updated 2023_5_25
% This script processes fluorescence detector logs, removing blanks,
% sorting samples, and outputting data for comparison across multiple
% runs and test types. The results include plots and statistical analysis.

% Script
```

```
Clearvars; clc; % Clears variables
%///////////// Input Parameters //////////////
Nruns =3; % Number of times each sample is Run
X = 24; % Number of highest values to keep (number of samples run in each log)

title_text = {'2023/6/26 Panel Figure Draft v2', 'Aggregate Analysis'};
Nruns = 3; % Number of measurements per sample
X = 24; % Number of samples per run
NumNegative = 12; % Number of Negative Samples -- where to divide sample set
POne = NumNegative +1; % Start for Positive Samples

%Pull out data for different time intervals
Test_Type = { 'SC2_Dry_5_17','ZIK','IBV_BIP','SC2_SV_5_17','IBV_LB'}; %
'SC2_2','SC2_20'};
 % define the time intervals
%data for all tests except time series and Duplex
Test_Name =  {'SARS COV 2', 'ZIKA', 'IBV BIP FAM','SC2 Sous Vide', 'IBV LB'};%

Test_Color = [0.1 0.3 0.9;  % SC2: Blue
            0 0.8 0.4;    % ZIKA: Green
            0.9 0.2 0.2;  % IBV_BIP_FAM: Red
              0.4 0.7 0.9; % SC2_SV_Time: Sky Blue
              0.9 0.4 0.1]  % IBV_LB: Burnt Orange

Test_Marker = {'o', '^', 's', 'd', 'h'};  % Circle, Triangle, Square, Diamond, Pentagon
RatioSort = "yes"; % Sorts the sample data by the fluorescence ratio value for plotting
% RatioSort = "no";

% set up initial data structures
```

```
data = cell(numel(Test_Type), Nruns); % create a cell array to store the data for each run
for i = 1:numel(Test_Type) % loop through the time intervals
  folder_path_neg = sprintf('NegativeSamples/Folder/Path', Test_Type{i});
  folder_path_pos = sprintf('PositiveSamples/Folder/Path', Test_Type{i});

for r = 1 : Nruns
  filename = sprintf('Run_%d_log.txt', r);
  %fileID = fopen(filename);
  fileID = fopen(fullfile(folder_path_neg, filename)); % Modify to read file from "Negatives" folder

  % Read the data
  textout = textscan(fileID,'%f %f %f %f %f %f %f %f %f','HeaderLines',18);
  fclose(fileID);
  full_array = [textout{1}, textout{2}, textout{3}, textout{4}, textout{5}, textout{6}, textout{7}, textout{8}, textout{9}];

  MM = [textout{3}, textout{6}, textout{9}];
  Negative{i,r} = MM; %store the array into a cell array data
end
%Pull out Positive data
for r = 1 : Nruns

  filename = sprintf('Run_%d_log.txt', r);
  %fileID = fopen(filename);

% Modify to read file from "Positive" folder
  fileID = fopen(fullfile(folder_path_pos, filename));
```

```
   % Read data from the log file, skipping the first 18 header lines
% 'textout' stores data as a cell array, with each column of the file stored in a separate cell
  textout = textscan(fileID,'%f %f %f %f %f %f %f %f %f','HeaderLines',18);
  fclose(fileID);
% Combine the 9 columns of data into 'full_array' for the positive samples
full_array = [textout{1}, textout{2}, textout{3}, textout{4}, textout{5},
textout{6},    textout{7}, textout{8}, textout{9}];
   % Extract the relevant columns for further analysis (e.g., 3rd, 6th, 9th columns)
  MM = [textout{3}, textout{6}, textout{9}];
  Positive{i,r} = MM; %store the array into a cell array data
End

%vertical concatenation of the negative and positive runs into set of single arrays
for r = 1:Nruns
  data{i,r} = [Negative{i,r} ; Positive{i,r}];
end

for r = 1 : Nruns
  n = size(data{i,r},1); % Number of rows in the array
  row_numbers = (1:n)'; % Create a column vector of row numbers
  data{i,r}= [row_numbers, data{i,r}]; % Add the row numbers column to the array

  % Sort the array based on the Yellow channel looking for Blank Captures
  [~, indices] = sort(data{i,r}(:,3), 'descend');
  % Keep the highest X number of values -->drop blanks
  data{i,r} = data{i,r}(indices(1:X), :);

  %resort based on the original order of captures
  % aligns the data based on order through detector
```

```
  [~, indices] = sort(data{i,r}(:,1), 'ascend');
  data{i,r} = data{i,r}(indices, :);

  n = size(data{i,r},1); % RE-Number of rows in the array
  row_numbers = (1:n)'; % Create a column vector of row numbers
  data{i,r}(:,1) = row_numbers;
  %data{i,r}= [data{i,r}, coordinates{i,r}]; %add on XY tube coordinates

     if RatioSort == "yes"
        %option to resort based on ratio value
        [~, indices] = sort(data{i,r}(:,4), 'ascend');
        data{i,r} = data{i,r}(indices(1:X), :);
     end
end
% create arrays for multiple run sample data to be compared
for r = 1 : Nruns

  for s = 1 : length(data{i,r}(:,1))   %put each sample in a new array
     sampleNum(s,i,r)      = data{i,r}(s,1);
     sampleBlu(s,i,r)      = data{i,r}(s,2);
     sampleYel(s,i,r)      = data{i,r}(s,3);
     sampleRatio(s,i,r)    = data{i,r}(s,4);
         %Values for each set of samples
        % (e.g. Blu holds all values of sample j in one array)
        Ratio(s,i,r) = sampleRatio(s,i,r);
        Blu(s,i,r) = sampleBlu(s,i,r);
        Yel(s,i,r) = sampleYel(s,i,r);
        BluAdjust(s,i,r) = sampleBluAdjust(s,i,r);
```

```
        RatioAdjust(s,i,r) = sampleRatioAdjust(s,i,r);

 %Standard Deviation and Mean Calculations
        Ratio_SD(s,i) = std(Ratio(s,i,:));
        Ratio_Mean(s,i) = mean(Ratio(s,i,:));
        RatioAdjust_SD(s,i) = std(RatioAdjust(s,i,:));
        RatioAdjust_Mean(s,i) = mean(RatioAdjust(s,i,:));
        Blu_SD(s,i) = std(Blu(s,i,:));
        Blu_Mean(s,i) = mean(Blu(s,i,:));
        BluAdjust_SD(s,i) = std(BluAdjust(s,i,:));
        BluAdjust_Mean(s,i) = mean(BluAdjust(s,i,:));
        Yel_SD(s,i) = std(Yel(s,i,:));
        Yel_Mean(s,i) = mean(Yel(s,i,:));
    end
  end
End

%% Calculate neg and pos mean and SDs
% Preallocate arrays to store the results
negMeans = zeros(1, 5);
negSDs = zeros(1, 5);
posMeans = zeros(1, 5);
posSDs = zeros(1, 5);
% Calculate means and SDs for each test
for i = 1:5 % For each test
  % Negative samples statistics (samples 1:12)
  negMeans(i) = mean(Ratio(1:12, i, :), [1 3]); % Mean over samples and runs
  negSDs(i) = std(Ratio(1:12, i, :), 0, [1 3]); % Standard deviation over samples and runs
```

```
  % Positive samples statistics (samples 13:end)
  posMeans(i) = mean(Ratio(13:end, i, :), [1 3]);
  posSDs(i) = std(Ratio(13:end, i, :), 0, [1 3]);
  % Display results
  fprintf('Test %d - Negative Samples: Mean = %.4f, SD = %.4f\n', i, negMeans(i), negSDs(i));
  fprintf('Test %d - Positive Samples: Mean = %.4f, SD = %.4f\n', i, posMeans(i), posSDs(i));
end

% Optional: Store results in a structure for easy access and further processing
Results = struct('NegativeMeans', negMeans, 'NegativeSDs', negSDs, ...
          'PositiveMeans', posMeans, 'PositiveSDs', posSDs);
%% Generate CSV for analysis
% Creating a table to store the processed data
headers = {'Sample Number', 'Sample Blu', 'Sample Yel', 'Sample Ratio', ...
      'Sample Blu Adjust', 'Sample Ratio Adjust', 'Blu Mean', ...
      'Blu SD', 'Blu Adjust Mean', 'Blu Adjust SD', 'Yel Mean', ...
      'Yel SD', 'Ratio Mean', 'Ratio SD', 'Ratio Adjust Mean', ...
      'Ratio Adjust SD'};

% Initializing an empty table
processed_data = array2table(zeros(0,16), 'VariableNames', headers);
for i = 1:numel(Test_Type)
  for s = 1:X
     new_row = table(sampleNum(s,i,1), sampleBlu(s,i,1), sampleYel(s,i,1), ...
            sampleRatio(s,i,1), sampleBluAdjust(s,i,1), ...
            sampleRatioAdjust(s,i,1), Blu_Mean(s,i), Blu_SD(s,i), ...
            BluAdjust_Mean(s,i), BluAdjust_SD(s,i), Yel_Mean(s,i), ...
            Yel_SD(s,i), Ratio_Mean(s,i), Ratio_SD(s,i), ...
```

```
                    RatioAdjust_Mean(s,i), RatioAdjust_SD(s,i), ...
                    'VariableNames', headers);
        % Appending the new row to the table
        processed_data = [processed_data; new_row];
    end
end
% Writing the table to a CSV file
writetable(processed_data, 'CoreSamples_data.csv');
```